Tampere University

Jasmin Laitamäki

# COMPARING PROPERTIES OF DIFFERENT INFRARED CAMERAS

Faculty of Information Technology
and Communication Sciences
Master of Science Thesis
August 2019

# ABSTRACT

Jasmin Laitamäki: Comparing properties of different infrared cameras
Master of Science Thesis
Tampere University
Master's Degree Programme in Information Technology
August 2019

---

Infrared (IR) camera enables to measure the temperature of an object without contact. As a result, a thermal image is created, and it is usually visualized by colours/contrast representing different temperature values. Originally, IR cameras were developed for military and surveillance purposes. As the features of IR cameras evolved and cost decreased, the application field expanded also to other areas such as industry and medicine. This thesis work is conducted on requirements and desires of medical technology company Imaqen Ltd. The aim was to acquire a better understanding of different IR camera technologies, compare those to each other on paper and carry out measurements, where the ability of the IR cameras to detect fast effects is tested and the noise levels of the cameras are determined. On this ground, one could find the most suitable IR camera to a future application of the company.

Among other things, spectral range, sensitivity and response time of IR cameras depend on the material and technology of the detector. These properties influence e.g. in which temperature range the camera is working, how small temperature differences can be distinguished and how fast effects can be detected. The real functionality of an IR camera is revealed only in practical testing, so in addition to theoretical study, five different IR cameras were tested. Three cameras were cooled photovoltaic (PV) detectors, which measure the temperature of an object by counting incident photons. Two cameras were microbolometers (MB), which operation is based on variation in temperature of sensing elements of the detector. The aim was to measure how well the cameras are detecting heat effects lasting only a couple of milliseconds. A technical phantom was built for the measurement, where a rotating plate with a small hole was adjusting the time a warm object behind it was visible. By increasing the angular velocity of the plate, the time of the heat effect was reduced to 2.7 ms. Noise level of the camera affects how small temperature differences the camera can distinguish. Therefore, the characteristic noise level of every camera was calculated, and this was compared to the NETD (noise-equivalent temperature difference) value provided by the manufacturer.

MBs are not suitable for detecting heat effects that last only a couple of milliseconds due to their long response time i.e. the thermal time constant of the sensing element. The PV detectors on the other hand are very suitable for fast recognition tasks as their response time is short. However, an aliasing effect was discovered because of a too low frame rate. This can be a limiting factor when the effect time decreases and if the frame rate of the camera cannot be increased. All the noise levels were higher than values provided by the manufacturers, especially with MBs. This difference of noise levels between MB and PV detectors makes the latter more suitable for detecting small temperature differences on a scene.

Based on the results and theory, one can conclude that PV detectors have better fast recognition and noise features than MBs. However, cost and size of MBs are considerably reduced compared to PV detectors. This can turn out to be a selection criterion if the minimum requirements are fulfilled. There are still other detectors used in IR cameras e.g. quantum well infrared photodetector, which were not tested in this work. Thus it would be beneficial to reproduce these tests with a larger variety of different IR detector technologies; only then more precise conclusions about the best detector could be made. Sometimes a trade-off between some features must be made, for example, it has to be decided if a fast response time is more important than high sensitivity with a large resolution. The application will set the requirements for optimal features of the IR camera. Therefore, different cameras cannot be put in order without knowing what the target application is.

Keywords: infrared radiation, temperature measurement, microbolometer, photon detector

# TIIVISTELMÄ

Jasmin Laitamäki: Erilaisten lämpökameroiden ominaisuuksien vertailu
Diplomityö
Tampereen yliopisto
Tietotekniikan diplomi-insinöörin tutkinto-ohjelma
Elokuu 2019

Lämpökamera mahdollistaa kohteen lämpötilan mittaamisen ilman kontaktia. Sillä saadaan kohteesta lämpökuva, jossa värit/sävyt edustavat eri lämpötiloja. Alun perin lämpökameroita käytettiin ja kehitettiin sotilas- ja valvontakäyttöön. Kameroiden hintojen laskiessa ja ilmaisimien ominaisuuksien parantuessa sovellusalue on laajentunut myös muun muassa teollisuuteen ja lääketieteeseen. Tämä diplomityö on toteutettu terveysteknologia-alan yrityksen, Imaqen Oy:n tarpeita ja toiveita varten. Tavoitteena oli parantaa ymmärrystä eri lämpökamerateknologioiden ominaisuuksista sekä vertailla näitä keskenään niin teoriassa kuin käytännössä. Lähtökohtana oli toteuttaa mittaus, jossa vertaillaan eri kameroiden kykyä havaita nopeita ilmiöitä sekä määrittää kameroiden kohinatasot. Työn tavoitteena oli edesauttaa yrityksen päätöksentekoa tulevaisuuden laitehankintoja ajatellen.

Käytetystä ilmaisinmateriaalista ja –teknologiasta riippuen muun muassa lämpökameroiden spektrivaste, herkkyys sekä vasteaika vaihtelevat. Nämä ominaisuudet vaikuttavat esimerkiksi siihen, millä lämpötila-alueella kameralla pystytään kuvaamaan, kuinka pieniä lämpötilaeroja pystytään erottamaan ja kuinka nopeita ilmiöitä havaitsemaan. Todellinen toiminta paljastuu kuitenkin vasta käytännön testeissä. Teoreettisen tarkastelun lisäksi työssä suoritettiin testit viidelle eri lämpökameralle. Kolme kameroista oli jäähdytettyjä fotojännitekameroita, joiden kohteen lämpötilan mittaus perustuu kohteesta saapuvien fotonien laskemiseen. Lisäksi testattiin kaksi jäähdyttämätöntä mikrobolometria, joiden toiminta perustuu ilmaisinmateriaalin lämpötilan vaihteluun. Tavoitteena oli testata, kuinka hyvin eri kamerat havaitsevat lämpöilmiöitä, jotka ovat nopeimmillaan muutaman millisekunnin mittaisia. Tätä varten rakennettiin testijärjestelmä, jossa lämpölähteen näkymisaikaa kameralle säädettiin pyörivän reikälevyn avulla. Pyörimisnopeutta kasvattamalla saatiin lämpöilmiötä lyhennettyä aina 2,7 millisekuntiin asti. Kameran kohinataso vaikuttaa siihen, kuinka pieniä lämpötilaeroja kameralla pystytään havaitsemaan. Tämän vuoksi jokaiselle kameralle määritettiin sen ominainen kohinataso, jota verrattiin kameravalmistajan ilmoittamaan NETD-arvoon (noise-equivalent temperature difference).

Mikrobolometrit eivät sovellu millisekunnin luokkaa olevien lämpöilmiöiden havaitsemiseen niiden pitkän vasteajan vuoksi, joka riippuu materiaalin termisestä aikavakiosta. Fotojännitekameroissa vasteaika on lyhyt, joten ne soveltuvat nopeiden ilmiöiden havaitsemiseen. Tuloksissa havaittiin kuitenkin taajuuksien laskostumista liian matalan kuvanottotaajuuden vuoksi. Tämä voi muodostua rajoittavaksi tekijäksi ilmiönopeuden kasvaessa, jos kameran kuvanottotaajuutta ei pystytä nostamaan. Kohinatasot olivat kaikilla kameroilla valmistajien ilmoittamia arvoja korkeammalla, erityisesti mikrobolometreilla. Ero mikrobolometri- ja fotojännitekameroiden kohinatasojen välillä tekee fotojännitekameroista soveltuvampia pienten lämpötilaerojen havaitsemiseen.

Tulosten ja teorian perusteella voidaan todeta, että fotojännitekamerat ovat sekä nopeus- että kohinaominaisuuksiltaan mikrobolometreja parempia. Mikrobolometrien koko sekä kustannukset ovat kuitenkin fotojännitekameroita huomattavasti pienemmät. Tämä voi osoittautua valintakriteeriksi, jos kuvattavan kohteen asettamat vaatimukset täyttyvät. On kuitenkin olemassa myös muita lämpökameroissa käytettyjä ilmaisimia, kuten kvanttikaivoilmaisin, joita ei tämän työn aikana päästy testaamaan. Vaaditaan siis testien toistamista laajemmalla otannalla eri ilmaisinteknologioita, jotta tarkempia johtopäätöksiä parhaasta lämpökamerasta pystytään tekemään. Osa kameran ominaisuuksista vaatii myös kompromissien tekemistä. Täytyy esimerkiksi päättää, onko tärkeämpää kuvausnopeus vai pienten lämpötilaerojen havaitseminen suurella resoluutiolla. Käyttökohde asettaa vaatimukset optimaaliselle kameralle, eikä lämpökameroita voida siis asettaa paremmuusjärjestykseen tietämättä ensin, mitä ollaan kuvaamassa.

Avainsanat: infrapunasäteily, lämpötilan mittaus, mikrobolometri, fotoni-ilmaisin

# PREFACE

I would like to thank my examiner Assistant Professor Antti Vehkaoja for sharing his knowledge and giving valuable comments for this thesis work. I thank my examiner Assistant Professor Jani Boutellier for giving his thoughts for this thesis. I express my gratitude to Imaqen Ltd and all its members making this project possible, being involved in camera tests and giving their comments for this thesis. I would like to thank Ph.D. Janne Tamminen for all the help on the project. I express my gratitude to D.Sc. Risto Joro for sharing his knowledge. I am grateful to M.Sc. Heimo Ihalainen for sharing his thoughts and time, teaching me about signal processing and giving me a lot of valuable comments on this thesis. My compliments to Ph.D. Topi Kaaresoja and Infradex Inc for making the measurements possible with FLIR's X6900sc and T1020 cameras and for excellent advice. I express my gratitude to M.Sc. Guilherme Soares and M.Sc. Jari Rämö for the help with Telops Fast-IR 2K camera. I am grateful to D.Sc. Ari Kankkunen and Aalto University for an opportunity to test their camera, FLIR SC7600. I would like to thank M.Sc. Seppo Vihinen for guidance with camera calibration and for borrowing his calibration container. I thank M.Sc. Jari Väliaho for borrowing and advising with the microcontroller and helping me to build the test set-up. My compliments to M.Sc. Markus Karjalainen for borrowing his temperature sensor. I thank Senior Laboratory Technician Jouni Niemelä for helping me to plan and build the test set-up. I also express my gratitude to many other co-workers for many ideas, inspiring working atmosphere and instructive coffee room discussions.

I am grateful to my friends and family for all the help during my studies. Especially to Markus for thoughts and comments for this thesis, Laura for advice and encouragement, and my mother for helping me to edit the figures of this thesis work and always being supportive. Lastly, I thank my fiancèe Petri for proof-reading this thesis, helping me to improve my English and before anything, being patient and supportive.

Tampere, 15.8.2019

Jasmin Laitamäki

# CONTENTS

# LIST OF FIGURES

# LIST OF TABLES

# LIST OF ABBREVIATIONS AND SYMBOLS

| | |
|---|---|
| A/D | Analog-to-digital |
| CCD | Charge-coupled device |
| CMOS | Complementary metal-oxide semiconductor |
| FIR | Far infrared |
| FOV | Field of view |
| FPA | Focal plane array |
| G-R | Generation-recombination |
| IFOV | Instantaneous field of view |
| IR | Infrared |
| LWIR | Long-wavelength infrared |
| MCT | Mercury cadmium telluride |
| MOSFET | Metal-oxide-semiconductor field-effect transistor |
| MRTD | Minimum resolvable temperature difference |
| MTF | Modulation transfer function |
| MWIR | Mid-wavelength infrared |
| NEI | Noise-equivalent irradiance |
| NEP | Noise-equivalent power |
| NETD | Noise-equivalent temperature difference |
| NIR | Near-infrared |
| NUC | Non-uniformity correction |
| PC | Photoconductor |
| PIN | p-i-n photodiode |
| PV | Photovoltaic |
| QDOT | Quantum dot |
| QWIP | Quantum well infrared photodetector |
| ROIC | Readout integrated circuit |
| RPM | Revolutions per minute |
| RT | Radiometric temperature |
| SLS | Strained layer superlattice |
| SNR | Signal-to-noise ratio |
| SWIR | Short-wavelength infrared |
| TCR | Temperature coefficient of resistance |
| URL | Uniform Resource Locator |

| | |
|---|---|
| $A$ | Area of the surface ($m^2$) |
| $b$ | Constant, used in absorption coefficient calculation ($s^2/(kg \cdot m^3)$) |
| $C$ | Thermal contrast |
| $C_1$ | Constant, used in Planck's law ($W \cdot \mu m^4/m^2$) |
| $C_2$ | Constant, used in Planck's law ($\mu m \cdot K$) |
| $C_t$ | Thermal capacitance (J/K) |
| $c$ | Specific heat ($J/(kg \cdot K)$) |
| $c_0$ | Speed of light (m/s) |
| $D$ | Aperture diameter (m) |
| $D^*$ | Detectivity ($cm\sqrt{Hz}/W$ or Jones) |
| $d$ | Dimension of the detector (m) |
| $E$ | Energy of the molecule (J) |
| $E_g$ | Bandgap energy (J) |
| $E_p$ | Energy of one incident photon (J) |
| $\dot{E}_{pix}$ | Change in the energy of the pixel (W) |
| $\dot{E}_{rad}$ | Radiation heat transfer into the pixel (W) |
| $e$ | Napier's constant |
| $F$ | Focal point (m) |
| $F_s$ | Nyquist rate (Hz) |
| $f$ | Frequency (Hz) |
| $f_{max}$ | Nyquist frequency (Hz) |
| $\Delta f$ | Electrical or noise bandwidth (Hz) |
| f | Focal length (m) |
| f# | f-number |
| $G$ | Photoconductive gain |
| $h$ | Planck's constant ($J \cdot s$) |
| $\hbar$ | Reduced Planck's constant ($J \cdot s$) |
| $h_r$ | Radiation heat transfer coefficient ($W/(m^2 \cdot K)$) |
| $I$ | Output current (A) |
| $I_b$ | Bias current (A) |
| $I_{back}$ | Background current (A) |
| $I_{dark}$ | Dark current (A) |
| $I_{signal}$ | Examined signal current (A) |
| $i$ | Noise current (A) |
| $j$ | Integer (1, 2, 3, 4...) |
| $k$ | Bolzmann's constant (J/K) |
| $L_d$ | Depth of the well (m) |
| $L_w$ | Width of the well (m) |
| $m$ | Mass (kg) |

| | |
|---|---|
| $m^*$ | Effective mass (kg) |
| $N_b$ | Number of bits |
| $\dot{N}_c$ | Carrier generation rate (1/s) |
| $N_p$ | Photon irradiance ($1/(\mathrm{m}^2 \cdot \mathrm{s})$) |
| $N_{pix}$ | Number of pixels |
| $NA$ | Numerical aperture |
| $n$ | Refraction index of the medium |
| $Q$ | Incident spectral photon flux ($1/(\mathrm{m}^2 \cdot \mathrm{s})$) |
| $QE$ | Quantum efficiency |
| $q$ | Elementary charge (C) |
| $q_{rad}$ | Heat transfer rate (W) |
| $\mathcal{R}$ | Responsivity (A/W) |
| $R$ | Electrical resistance ($\Omega$) |
| $R_t$ | Thermal resistance (K/W) |
| $r$ | Minimum distance according to the Rayleigh criterion (m) |
| $s_i$ | Distance between the lens and the image (m) |
| $s_o$ | Distance between the lens and the object (m) |
| $T$ | Temperature of the object (K) |
| $T_\infty$ | Temperature of surroundings (K) |
| $t$ | Time (s) |
| $U$ | Voltage (V) |
| $V$ | Volume ($\mathrm{m}^3$) |
| $W$ | Emissive power of the real surface ($\mathrm{W/m}^2$) |
| $W_b$ | Emissive power of the blackbody ($\mathrm{W/m}^2$) |
| $x$ | Thickness of the detector (cm) |
| $\alpha$ | Absorptivity or absorption coefficient ($\mathrm{cm}^{-1}$) |
| $\alpha_T$ | Relative temperature coefficient of temperature |
| $\beta$ | Reflectivity |
| $\gamma$ | Transmissivity |
| $\varepsilon$ | Emissivity |
| $\sigma$ | Stefan-Boltzmann constant ($\mathrm{W}/(\mathrm{m}^2 \cdot \mathrm{K}^4)$) |
| $\lambda$ | Wavelength (m or µm) |
| $\rho$ | Mass density ($\mathrm{kg/m}^3$) |
| $\tau$ | Thermal time constant (s or ms) |
| $\Phi$ | Radiation power (W) |
| $\theta$ | Angle of the radiation cone divided by two (°) |

# 1. INTRODUCTION

Infrared (IR) camera is a device that measures incident IR radiation emitted by objects and therefore allows a remote way to measure the temperature of an object without contact. IR radiation is electromagnetic radiation, which wavelength region, 0.75–1000 µm, lies between visible light and microwaves. All objects with a temperature over absolute zero emit IR radiation. (Hamamatsu and Solid State Division, 2011) The main part of the IR camera is a focal plane array (FPA) that consists of a two-dimensional array of individual sensing elements. Those sensing elements collect incident radiation energy from environment and convert it into an electric signal, thus creating a thermal image of the scene. (Meola et al., 2015)

The original applications for IR cameras were surveillance and night vision tools for military purposes. As the cost of IR cameras has decreased and image quality improved, e.g. higher sensitivity and resolution, the application field of these cameras has expanded. Nowadays IR cameras are also used in applications like animal tracking, building inspection, medicine (including veterinary), astronomy and industry defect imaging. (Gade and Moeslund, 2014; Tan and Mohseni, 2018; Hellier, 2013)

IR cameras are used in applications where ability to "see" the temperature of the object or temperature variation of the scene is beneficial. For example, with an IR camera it is possible to track a missing human in dark environment, which is impossible with visible light camera. In building inspection one can detect major points of heat loss of a building with IR camera as can be seen in Figure 1.1. In veterinary medicine for example, detection of inflammation from animals is easier when this can be done without touching the animal. IR cameras can also be used in medicine to examine physical processes of human body through distribution of temperatures on the skin. Requirements in this field are high for sensitivity as the temperature differences can be extremely small. (Gade and Moeslund, 2014)

One can find a variety of IR cameras with different features and prices. A standalone thermal imaging device with a $32 \times 32$ pixel resolution can be found under 200 euros for an application that does not need high resolution and sensitivity. Even a small thermal camera that can be combined with a smartphone can be found around

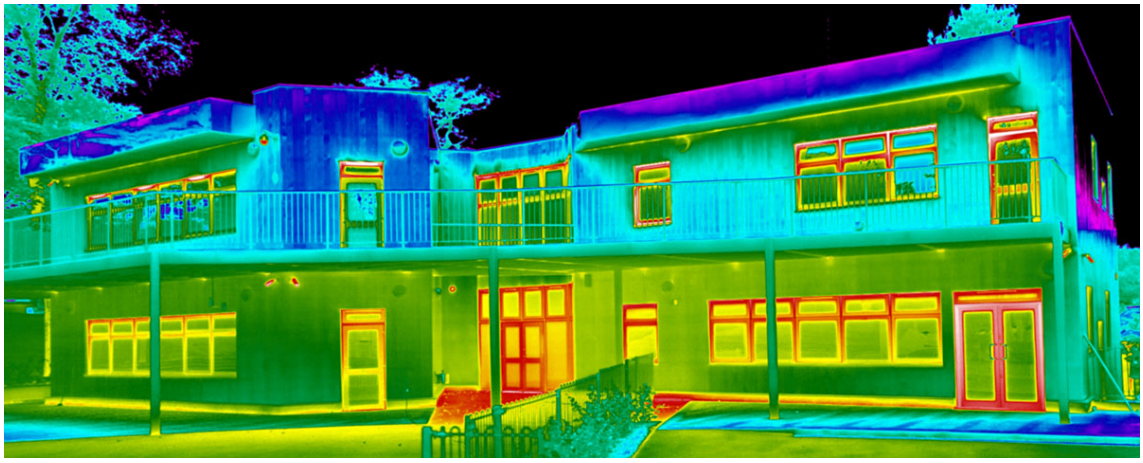

***Figure 1.1*** *Thermal image of a building shows the heat loss around doors and windows. (Red Current Ltd, 2019)*

100 euros. Affordable products like these are offered for example by Perfect Prime (https://perfectprime.com/pages/thermal-imaging-camera). However, the price of the IR camera increases as its features and performance are improved e.g. resolution, frame rate and sensitivity are increased. So, a high-end camera can exceed a price of 100 000 euros. (Webster and Eren, 2014)

This thesis work was funded by medical technology company Imaqen Ltd and it was executed in a research group of Sensor Technology and Biomeasurements in Tampere University. The aim of this work was to obtain a better understanding about technologies used in IR cameras. The purpose was to compare different features of IR cameras, to obtain specifications that are important and so find the most suitable camera solution for a future application of Imaqen Ltd. In this study, five IR cameras were tested, three based on indium antimonide (InSb) photon detectors and two based on microbolometers. The operating principles of these two cameras are very different. Photon detectors count photons of incident IR radiation, whereas incident radiation heats the sensing elements of the microbolometer and thus their resistance will change. The aim was to assess the differences between fast recognition abilities of tested IR cameras and also to examine how small temperature differences the cameras can detect. The noise levels associating with IR cameras were also defined both spatially and temporally. A technical phantom that creates a rapid controllable heat effect was planned and built for the measurements. The phantom contains a rotating plate with a hole that adjusts the time a warm object behind of it is visible for the camera. Also Posch et al. (2009) have used a rotating plate set-up to test a performance a novel IR sensor.

The noise-equivalent temperature difference (NETD) value defines the temperature difference in a scene that will create a signal equal to the noise level (Vincent et

al., 2015, p. 169). So the NETD values of tested cameras were defined and also compared to values provided by the manufacturers. Meola et al. (2015) also tested, how well different IR cameras can detect very small temperature differences. During the camera tests a calibration of IR camera is introduced as well as non-uniformity correction (NUC) procedure, that is highly important for a functional IR FPA.

Chapter 2 presents the theory behind the IR radiation. Basic structures and working principles of different types of IR detectors, including a microbolometer and different photon detectors, are introduced. Properties of the detectors are presented in a general level and other components of IR camera systems are considered. At the end of the chapter, different noise components and figures of merit are presented for IR cameras. In Chapter 3, the structure of the technical phantom is introduced as well as the evaluated cameras. Role of the calibration and NUC is also discussed. Finally, the camera test procedure is introduced, and noise level detection of the cameras is discussed. Test results are presented and discussed in Chapter 4 and lastly, the conclusion of the work is reported in Chapter 5.

# 2. THEORETICAL BACKGROUND

Particles of the material have motion when the temperature of the material is over absolute zero (0 K, -273.15 ℃). This random motion is caused by kinetic energy of the particles. The larger the kinetic energy of the particles, the higher is the temperature of the material. (Weng, 2012) Temperature of the material can be measured in different ways. One way is to use a device that is in physical contact with the object being measured. This type of contact temperature sensor utilizes conduction of thermal energy between the object and the sensor. The own temperature of the sensor is changing and this will change properties of the sensor e.g. the volume of the liquid inside a class tube (liquid-in-glass thermometer) or voltage (thermocouple). In some cases it is hard or even impossible to create a good contact with the measured object e.g. when it is in hazardous location or the object is moving. In these cases a non-contact temperature sensor can be the only option to measure the temperature of the object. (Soloman, 2010; McGee, 1988) In this thesis work, non-contact temperature measurement methods using IR thermography are discussed.

Thermography is based on sensing the IR radiation that the surface of the object is emitting. This emitted radiation cannot be seen by human eye, except if the surface is hot enough. However, with IR camera this radiation can be converted to a visual image. This image does not show the colors of the object but rather the thermal variation of the object surface. (*The ultimate IR handbook* 2012, p. 4)

## 2.1 Physics of infrared radiation

There are four different categories of the energy of a molecule. One part is coming from interactions of nuclei and electrons of the molecule, this is called electronic energy. The centre of mass of the molecule is moving through space, this motion is causing translational energy. Two other parts are vibrational and rotational energy caused by vibration and rotation of the molecule and its atoms. So the energy $E$ of the molecule is expressed as the sum of these four different energy categories:

$$E = E_e + E_{trans} + E_{vib} + E_{rot}. \tag{2.1}$$

The translational $E_{trans}$, vibrational $E_{vib}$ and rotational $E_{rot}$ energies of molecules create the temperature of an object. (Serway and Jewett, 2014, p. 1344) The energies of a molecule are quantized and so only certain discrete energy levels are allowed to a molecule (Gade and Moeslund, 2014, p. 247).

Molecules can absorb and emit electromagnetic radiation. When incident radiation is absorbed the molecule will rise to an excited energy state. Conversely, when the molecule will fall back to ground state it will emit a photon. The energy of a photon absorbed (or emitted) has to be equal to the difference between these two energy levels. All objects with temperature over absolute zero emit IR radiation that corresponds to their temperature. If more radiation is emitted than absorbed the temperature of the object will decrease and vice versa. (Gade and Moeslund, 2014, p. 247-248)

In addition to temperature, the power of radiation emitted depends on the material and condition of the object surface. Therefore, different objects even with the same temperature may have different radiation power per unit surface area. However, there is a maximum power of radiation that can be emitted by the surface of an object at a certain temperature. This ideal radiator is called a *blackbody* and it is providing a standard against which radiative properties of real surfaces are compared. (Cengel, 2002, p. 565)

### 2.1.1 Blackbody radiation

When observing a transfer of IR radiation, it is important to understand the concept of blackbody. According to the definition, blackbody absorbs all the radiation regardless of the direction or wavelength of the radiation. Respectively, at certain temperature blackbody emits the maximum possible amount of thermal radiation. (Agrawal and Platzer, 2018) The radiation power emitted by the blackbody can be described by Stefan-Boltzmann law

$$W_b = \sigma T^4, \tag{2.2}$$

where $\sigma = 5.670 \cdot 10^{-8}\ W \cdot m^{-2} \cdot K^{-4}$ denotes the Stefan-Boltzmann constant and $T$ is the absolute temperature of the surface in Kelvin. One can notice that the emissive power of blackbody is proportional to the fourth power of the absolute temperature

and not depend on wavelength of the radiation. So the sum of the radiation emitted over all wavelengths is accounted. (Cengel, 2002, p. 565–566)

In some cases, it is important to know the *spectral* emissive power of blackbody $W_{b\lambda}$, which is presented as a function of wavelength $\lambda$. This relation of wavelength to the emissive power is known as Planck's law and can be expressed as

$$W_{b\lambda} = \frac{C_1 \lambda^{-5}}{e^{C_2/\lambda T} - 1}, \tag{2.3}$$

where

$$C_1 = 2\pi h c_0^2 = 3.742 \cdot 10^8 \ W \cdot \mu m^4/m^2$$
$$C_2 = h c_0/k = 1.439 \cdot 10^4 \ \mu m \cdot K$$

and $h = 6.626 \cdot 10^{-34} \ J \cdot s$ is the Planck's constant, $c_0 = 2.998 \cdot 10^8 \ m/s$ stands for the speed of light and $k = 1.381 \cdot 10^{-23} \ J/K$ is the Boltzmann constant. The constants $C_1$ and $C_2$ are valid only when a blackbody is placed in vacuum or gas. If other medium is used, $C_1$ needs to be replaced by $C_1/n^2$, where $n$ is a refraction index of the medium. (Cengel, 2002, p. 565–566)

Figure 2.1 shows that at any specific temperature there is a specific emittance curve that is a function of wavelength. The emitted radiation increases with wavelength, reaches the maximum and decreases with increasing wavelength again. The emissive power is also increasing with temperature at any wavelength. As the curves shift to the left as the temperature increases, one can come to the conclusion that a larger fraction of radiation is emitted at shorter wavelengths when the temperature is high. (Cengel, 2002, p. 565–566)

For every emittance curve there is a wavelength which gives the maximum value of the radiation. This wavelength $\lambda_{max}$ is inversely proportional to the absolute temperature and can be approximated from Wien's displacement law,

$$\lambda_{max} = \frac{2898 \ [\mu m \cdot K]}{T}, \tag{2.4}$$

where $\lambda_{max}$ is measured in micrometers and $T$ in Kelvin (*The ultimate IR handbook* 2012; Agrawal and Platzer, 2018). In Figure 2.1, the wavelength $\lambda_{max}$ of every emittance curve is marked with a vertical red line.

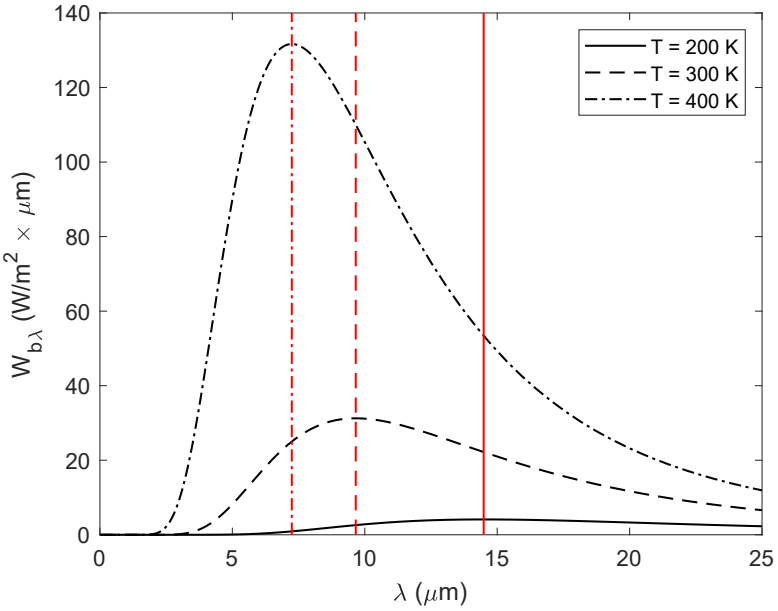


***Figure 2.1*** *The emissive power as a function of wavelength for 200 K, 300 K and 400 K. The maximum value and so the wavelength $\lambda_{max}$ of every emittance curve is marked with a vertical red line.*

### 2.1.2 Emissivity

When incident radiation hits the surface of an object, part of the radiation is reflected, other part is absorbed and possible remaining part is transmitted through the object (Mobley, 2013). The total incident radiation energy can be stated as

$$W = W\alpha + W\beta + W\gamma. \tag{2.5}$$

When the previous formula is divided by $W$, one gets

$$1 = \alpha + \beta + \gamma, \tag{2.6}$$

where $0 \leq \alpha \leq 1$ stands for absorptivity, $0 \leq \beta \leq 1$ for reflectivity and $0 \leq \gamma \leq 1$ for transmissivity. The value, that every coefficient gets, depends on how well the object reflects, absorbs or transmits incident radiation. For example, for material that is opaque transmissivity $\gamma = 0$. It is important to notice that materials that are transparent to visible light may be opaque to IR light. That is why the same lens material cannot be used for both visible light and IR cameras. (*The ultimate IR handbook* 2012, pp. 4–5)

Radiation properties of a real object are compared to the blackbody and therefore ratio of the emitted energy of a real object surface ($W$) to the emitted energy of the blackbody surface ($W_b$) is called *emissivity* $\varepsilon$ of the object surface. This property shows how efficiently the surface emits energy in relation to the blackbody and can be presented as

$$\varepsilon = \frac{W}{W_b}. \tag{2.7}$$

As the blackbody is a perfect radiator, a real object can have the emissivity between 0 and 1. The better the radiative properties of the object surface, the higher is the emissivity. (*The ultimate IR handbook* 2012, p. 5) According to the Kirchhoff's law of thermal radiation, the emissivity and the absorptivity of an object are equal for a given wavelength,

$$\varepsilon(\lambda) = \alpha(\lambda). \tag{2.8}$$

The emissivity of an object is not constant. It varies with the temperature of the object and also with the wavelength and direction of the emitted radiation. A surface is called *diffuse* if its emissivity is independent of direction of the radiation. If the emissivity of a surface varies strongly with wavelength, the surface is called *selective* and if not, it is called *gray* surface. (Cengel, 2002, p. 578–580, 584) For a gray, diffuse surface the emissive power is

$$W = \varepsilon\sigma T^4. \tag{2.9}$$

For a gray surface one can present an equation for net rate of radiation heat transfer from the surface

$$q_{rad} = \varepsilon\sigma A(T^4 - T_\infty^4), \tag{2.10}$$

where $A$ stands for the area of the surface. $T$ and $T_\infty$ are the temperatures of the gray surface and surroundings, respectively. The surroundings is assumed to be isothermal and much larger to completely enclose the surface. The above equation gives the difference between thermal energy of the surface radiated by emission and gained by absorption from the surroundings. The previous equation can also be expressed in form

$$q_{rad} = h_r A(T - T_\infty), \tag{2.11}$$

where

$$h_r = \varepsilon\sigma(T + T_\infty)(T^2 + T_\infty^2) \tag{2.12}$$

is the radiation heat transfer coefficient. (Incropera and DeWitt, 2001, p. 10) The last two equations are important when considering the working principle of a microbolometer-type IR sensing element, as one can notice in Subsection 2.2.1.

### 2.1.3 Spectral bands of infrared radiation

The spectral range of IR radiation is 0.75–1000 µm. The range can be divided to sub-divisions:

- Near-infrared (NIR): 0.75–1.4 µm
- Short-wavelength infrared (SWIR): 1.4–3 µm
- Mid-wavelength infrared (MWIR): 3–8 µm
- Long-wavelength infrared (LWIR): 8–15 µm
- Far infrared (FIR): 15–1000 µm

(D'Amico et al., 2009, p. 22)

NIR and SWIR regions are used for example in optical communications and moisture analyzers (Hamamatsu and Solid State Division, 2011). Application fields for NIR and SWIR imaging also include: metal industry (e.g. high-temperature measurements), recycling industry (e.g. plastic sorting), astronomy (e.g. telescope NIR sensors), pharmaceutical industry and medical applications (Vollmer and Möllmann, 2017; Reich, 2005; Sakudo, 2016). From FIR region one can find FIR lasers that are used e.g. diagnostic measurements of plasma (J. Hecht, 1999). Thermal imaging in MWIR and LWIR ranges are used in various fields such as in security and surveillance applications and in medicine (Vollmer and Möllmann, 2017).

Radiation transparency of the atmosphere is varying through the spectral range and so the spectral regions at which IR radiation can pass through the atmosphere without major attenuation are called *atmospheric windows*. The main windows in IR range are at 0.75–2.5 µm, 3–5 µm and 8–14 µm. Carbon dioxide, ozone and water

vapor are absorbing incident radiation at other regions. (Weng, 2012) In Figure 2.2, one can see the atmospheric windows in thermal IR range and regions where radiation is absorbed by the atmosphere.

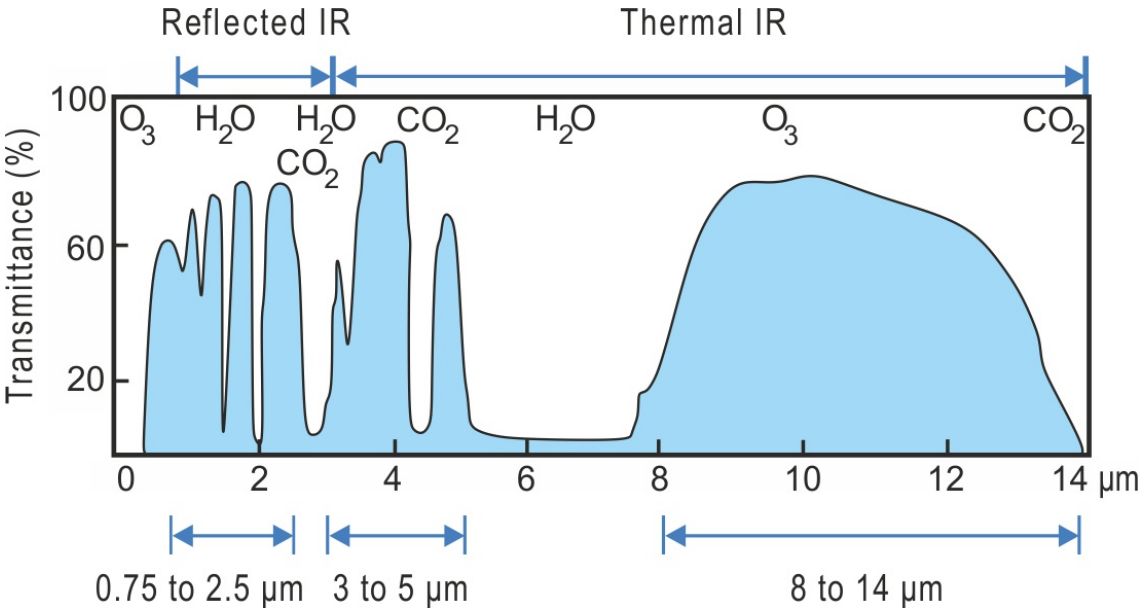


***Figure 2.2*** *Radiation transmittance of the atmosphere. The main atmospheric windows in IR range are marked at the bottom of the figure. Adapted from Weng (2012)*

MWIR and LWIR spectral bands differ from each other, for example with respect to contrast, background signal, atmospheric transmission dependence on weather, scene characteristics and optical aperture constraints. Thermal contrast, that is discussed in more detail in Subsection 2.1.5, is higher in MWIR band than in LWIR band. MWIR band also has better transmissivity in high humidity and higher resolution because of about three times smaller optical diffraction. LWIR on the other hand has reduced background noise and performs better in fog, winter haze and dust than MWIR band. (Bass, 2010)

### 2.1.4 Optics of infrared radiation

Like in visible light cameras, there are lenses, windows and mirrors used in IR devices. The main difference is in the choice of the materials used. Normal glass is opaque when wavelength increases over 2 µm, so it cannot be used in IR devices as an optical material. (Vincent et al., 2015, p. 524) Compared to lenses in visible light cameras, there are not so many material options for IR cameras. While the materials used are relatively expensive and their transmission properties are still rather poor, the lenses are tried to be made as thin as possible. (Laikin, 2006)

Materials that are commonly used as an optical material in IR devices are presented in Table 2.1.

***Table 2.1*** *Optical materials used in IR devices. (Soloman, 2010; Knight Optical, 2014; GRYSTAL GmbH, n.d.)*

| Material | Symbol | Spectral range (µm) | Transmission (%) |
|---|---|---|---|
| Quartz | $SiO_2$ | 0.18–3.5 | > 90 |
| Barium fluoride | $BaF_2$ | 0.2–8 | > 90 |
| Calcium fluoride | $CaF_2$ | 0.3–8 | > 90 |
| Sapphire | $Al_2O_3$ | 0.2–4 | > 80 |
| Zinc selenide | ZnSe | 0.55–18 | > 60 |
| Silicon | Si | 1–6 | > 50 |
| Germanium | Ge | 2–14 | > 45 |

Important properties of the lens are focal length, aperture diameter, numerical aperture and f-number (Vincent et al., 2015, p. 553). The *focal length* f describes the ability of the lens to collect or diverge light and it is the distance between the center of the lens and the focal point. The *focal point* $F$ indicates the place of the image created by incident parallel rays of light. (Herzberger, 2014) These characters are illustrated in Figure 2.3.

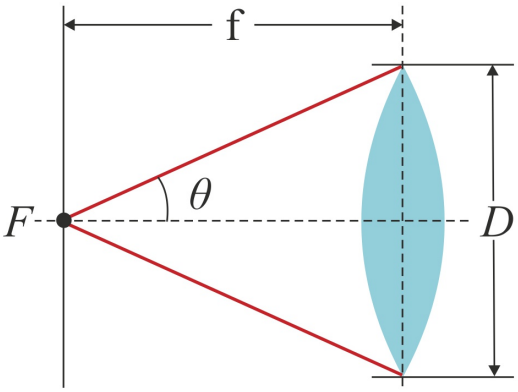


***Figure 2.3*** *Properties of a lens: focal length (f), focal point (F), aperture diameter (D) and angle of the radiation cone divided by two (θ).*

By knowing the distances of the object and the created image from the lens, the focal length f can be solved from Gaussian lens formula:

$$\frac{1}{\mathrm{f}} = \frac{1}{s_o} + \frac{1}{s_i}, \tag{2.13}$$

where $s_o$ is the distance between the lens and the object, and $s_i$ is the distance between the lens and the image (E. Hecht, 2017, p. 167).

The aperture diameter $D$ of the lens determines the bundle of rays which are going through the lens. The numerical aperture $NA$ is the measure that defines the angle of rays collected by the lens and it is defined as

$$NA = n \sin \theta, \tag{2.14}$$

where $n \approx 1$ in air and $\theta$ is the angle of the radiation cone at focal plane divided by two. (Vincent et al., 2015, p. 553)

Resolution of optical systems is limited by diffraction, aberration and manufacturing defects. In many cases diffraction is the primary limitation as aberration and manufacturing flaws can be prevented by careful design and manufacturing of the lens. For every lens and optical system, the diffraction-limited resolution is usually defined. This is an ultimate minimum distance $r$ between two points that still enables distinguishing those as individuals. (Driggers et al., 2012, p. 218-220) This distance can be presented by Rayleigh criterion

$$r = \frac{0.61\lambda}{NA} \tag{2.15}$$

for aberration- and defect-free optical system (Accetta and Shumaker, 1993, p. 110-111). As the wavelength increases, the spatial resolution decreases (Laikin, 2006).

The f-number f# describes the capability of the lens to gather radiation and it can be defined as

$$\mathrm{f\#} = \frac{1}{2NA} \approx \frac{\mathrm{f}}{D}. \tag{2.16}$$

One can notice that the bigger the aperture diameter is the smaller the f-number gets. The intensity of the incident radiation reaching the focal plane is inversely proportional to the square of the f-number, like one can see in next subsection. (Young et al., 2011; Vincent et al., 2015) Usually, the higher f-number will also reduce the price of the lens. It is important to have a low f-number for uncooled cameras e.g. microbolometers to maintain a suitable sensitivity of the camera. However, for cooled photon detectors, a higher f-number can be accepted as the same amount of incident radiation can be achieved just by increasing the exposure time. (Gade and

Moeslund, 2014, p. 249)

Besides the focal length, also the size of the detector determines how much off-axis scene the camera can capture on an image. The size of the pictured field is called *field of view* (FOV) and it can be solved as

$$FOV = 2\tan^{-1}\left(\frac{d}{2\mathrm{f}}\right), \tag{2.17}$$

where $d$ is one dimension of the detector. As the focal plane of an IR camera consists of many individual sensing elements, it is called focal plane array. (Kasunic, 2011)

It is sometimes worthwhile to divide the FOV into smaller units known as *instantaneous field of view* (IFOV). This is the field that one individual sensing element i.e. a pixel collects the radiation from. Equation 2.17 can be used to calculate the IFOV if the dimension of the detector is replaced by the pixel size. (Kasunic, 2011)

Different kinds of filters are used in IR devices. The simplest one has a broad band and its purpose is just to reduce the transmission of radiation and prevent the saturation of the detector at high temperatures. *Spectral adaptation* is used when spectral filter is blocking or transmitting certain wavelengths. This kind of filter can be called short-pass, long-pass, band-pass or narrow band-pass filter. Filters can be extremely helpful when one attempts to measure the temperature of a selective radiator. If the filter is blocking all wavelengths except the spectral range where the object is emitting, one can increase the confidence that the detector mostly measures the radiation of the object and not the background behind it. (*The ultimate IR handbook* 2012)

### 2.1.5 Thermal contrast

The incident spectral photon flux with use of a zero-emissivity bandpass filter for a hemispheric area is

$$Q = \int_{\lambda_1}^{\lambda_2} \gamma(\lambda) Q(T, \lambda) d\lambda, \tag{2.18}$$

where $\gamma$ is the in-band transmission, $\lambda_1$ is the cut-on wavelength and $\lambda_2$ is the cut-off wavelength. Zero emissivity of the filter is reached by cooling it until its self-radiation is negligible. (Rogalski, 2002, p. 23-24)

As discussed in the last subsection, the f-number f# of the lens has an impact on the intensity of the incident radiation. The density of incident photon flux on the surface of the detector can be expressed as

$$Q_B = \frac{1}{1 + 4(\mathrm{f}\#)^2} Q. \tag{2.19}$$

Temperature variations and differences in emissivity within a scene create a thermal image. When the temperature of the target is very close to the temperature of its background, the target becomes difficult to distinguish. In this case, the concept of *thermal contrast* becomes very important for thermal imaging. The thermal contrast depends on the spectral range of emitted radiation and can be presented as

$$C = \frac{\partial Q / \partial T}{Q}. \tag{2.20}$$

Even though many objects emit more radiation in LWIR than in MWIR band, the amount of radiation varies more with temperature in MWIR band. Because of this, the thermal contrast is higher in MWIR than in LWIR band. In Figure 2.4, one can find thermal contrast as a function of scene temperature for different sub-bands of MWIR and LWIR range. One can notice that when the temperature is 300 K, the thermal contrast in MWIR band is 3.5–4 %, while in LWIR band it is 1.6 %. (Rogalski, 2002; Rogalski, 2018)

## 2.2 Infrared detectors

An IR detector converts the energy of IR radiation into an electrical signal (Bass, 2010). Detectors can be divided into two groups: thermal detectors and photon detectors. With thermal detectors, the temperature of a target is measured based on increasing temperature of the sensing element heated by the emitted IR radiation of the target. This increase in temperature can be detected in multiple ways. For example with a bolometer, the increase of temperature is changing the electrical resistance of the detector, whereas with pyroelectrics, the electric polarization is changing i.e. a measurable voltage difference is created. (Kasunic, 2011; Khandpur, 2006) Photon detectors on the other hand count incident photons coming to the detector. Those detectors use either photovoltaic or photoconductive technologies. (Bass, 2010)

Photovoltaic detectors are the most common detectors used for imaging devices.

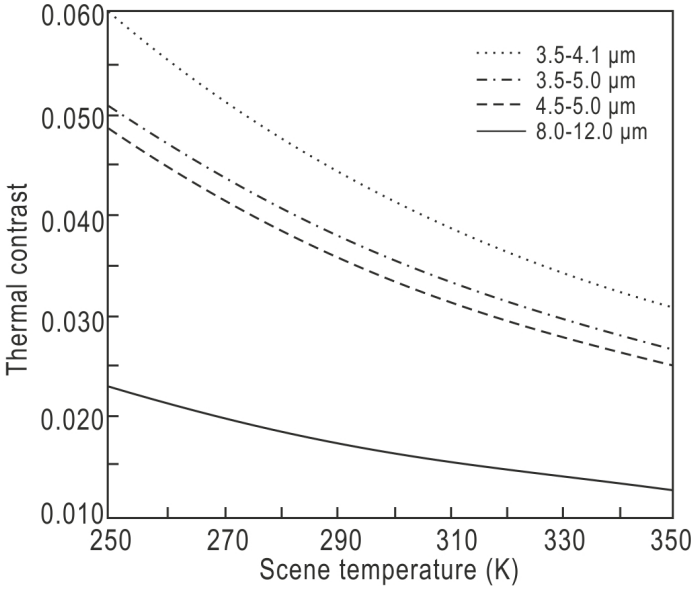


***Figure 2.4*** *Thermal contrast as a function of scene temperature in sub-bands of MWIR and LWIR. Adapted from Rogalski (2002)*

Indium antimonide (InSb) is used for MWIR imaging, while mercury cadmium telluride (HgCdTe or MCT) can be used for both, MWIR and LWIR imaging. Besides photovoltaic detectors, also quantum well IR photodetectors are used in imaging devices in many spectral ranges. Photon detectors are generally more sensitive and faster than thermal detectors, but as a drawback they require cooling to reduce the dark current. This is also the main reason why photon detectors are more expensive than thermal detectors. Uncooled bolometer on the other hand offers an inexpensive option when imaging in LWIR range. (Diakides et al., 2017; *The ultimate IR handbook* 2012)

### 2.2.1 Microbolometers

In these days, microbolometers are challenging photon detectors by offering competitive thermal sensitivity with a reduced cost. Typical spectral response of a microbolometer is 7–14 µm. Microbolometer utilizes micromachined sensors that use wafer-level silicon processing. (Khandpur, 2014) A wafer is a thin disk, made of silicon in this case, which is then processed by micromachining to create microstructures utilizing deposition, etching and other microfabrication techniques. The name *microbolometer* comes from microscale size of one pixel. (Soloman, 2010)

A microbolometer is a thermal detector which is heated by incident radiation. Be-

cause of the radiation, the temperature of sensing elements will rise and change the resistance of the elements. (Khandpur, 2014) Microbolometers do not need cooling, which is an advantage compared to photon detectors (Kasunic, 2011).

Typical structure of a microbolometer pixel (Figure 2.5) contains a membrane which is attached to a substrate. The membrane consists of an absorbing layer most commonly made of vanadium oxide (VOx) or amorphous silicon ($\alpha$-Si). The absorbing layer is facing the thermal source being measured. The layer will then heat up and its resistance will change accordingly. The membrane is isolated from the environment via thin, long legs. The purpose of the legs is to reduce the impact of thermal conductivity during the temperature measurement, connect the membrane to the readout integrated circuit (ROIC) and protect the membrane from damage during the deformation caused by temperature change. The heat convection can be reduced by placing the detector in vacuum. (Kasunic, 2011; Khandpur, 2014) A reflective layer is deposited under the membrane to improve absorption of incident radiation (Liu et al., 2006).

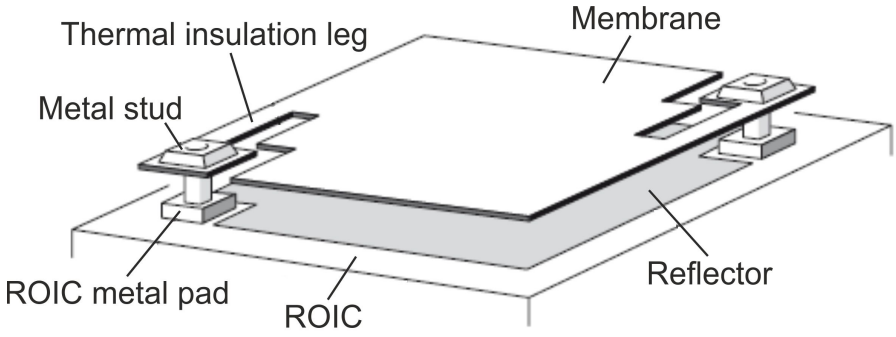


***Figure 2.5*** *Structure of one microbolometer pixel. Adapted from Kasunic (2011).*

The surface of a microbolometer pixel is collecting radiation from the environment. The net rate of thermal radiation from the source was determined in Equation 2.11. According to that equation, the *thermal resistance* for radiation can be expressed as

$$R_t = \frac{T - T_\infty}{q_{rad}} = \frac{1}{h_r A}, \tag{2.21}$$

where $h_r$ is determined in Equation 2.12 and $T$ and $T_\infty$ are the temperatures of the pixel and the environment, respectively. (Incropera and DeWitt, 2001, p. 91)

The temperature of the microbolometer pixel is assumed to be uniform and changing only with time. Let's assume, that the pixel has mass $m$, volume $V$, surface

area $A$, density $\rho$ and specific heat $c$ when the temperature of the pixel is $T_i$. The pixel is facing the environment at a temperature of $T_\infty$ with radiation heat transfer coefficient of $h_r$. One can assume that $T_\infty > T_i$, but the following equations are also valid for the opposite case. The temperature of the pixel will rise by a differential amount $dT$ within a differential time interval $dt$ when the radiation from the environment will hit the surface of the pixel. The radiation heat transfer into the pixel has to be equal to the increase in the energy of the pixel. The energy balance of the pixel for the time interval $dt$ can be presented as

$$\dot{E}_{rad} = \dot{E}_{pix} \tag{2.22}$$

or

$$h_r A(T_\infty - T)dt = mc\ dT. \tag{2.23}$$

Considering that $m = \rho V$ and $dT = d(T - T_\infty)$, the previous equation can be rearranged as

$$\frac{d(T - T_\infty)}{T - T_\infty} = -\frac{h_r A}{\rho V c}dt. \tag{2.24}$$

Integrating the equation from $t = 0$, in which case $T = T_i$, to time $t$, when $T = T(t)$, previous equation gives

$$\ln \frac{T(t) - T_\infty}{T_i - T_\infty} = -\frac{h_r A}{\rho V c}t. \tag{2.25}$$

The former can also be presented as

$$\frac{T(t) - T_\infty}{T_i - T_\infty} = e^{-t/\tau}. \tag{2.26}$$

In former equation, $\tau$ is the *thermal time constant* of the pixel and it can be expressed as

$$\tau = \left(\frac{1}{h_r A}\right)(\rho V c) = R_t\ C_t, \tag{2.27}$$

where $C_t$ is the thermal capacitance of the pixel. (Cengel, 2002, p. 210–211) Thermal time constant of modern microbolometers typically gets values between 8–12

ms (FLIR, 2016). If the values of $R_t$ or $C_t$ increase, the pixel will be slower to respond to changes in radiation coming from the environment. Thus decreasing the speed to reach the thermal equilibrium i.e. to follow the changes in the measured temperature. (Incropera and DeWitt, 2001, p. 242)

Like one can see in Figure 2.6, the thermal time constant of the pixel states the time required for the pixel temperature to change 63.2 % of temperature difference between the pixel and environment (Incropera and DeWitt, 2001, p. 242). The rule of thumb is that it will take five times the thermal time constant for pixel temperature to approximately reach the temperature of environment, that corresponds to change of 99.33 %. This time equals approximately 40–60 ms in typical microbolometer device. (FLIR, 2016)

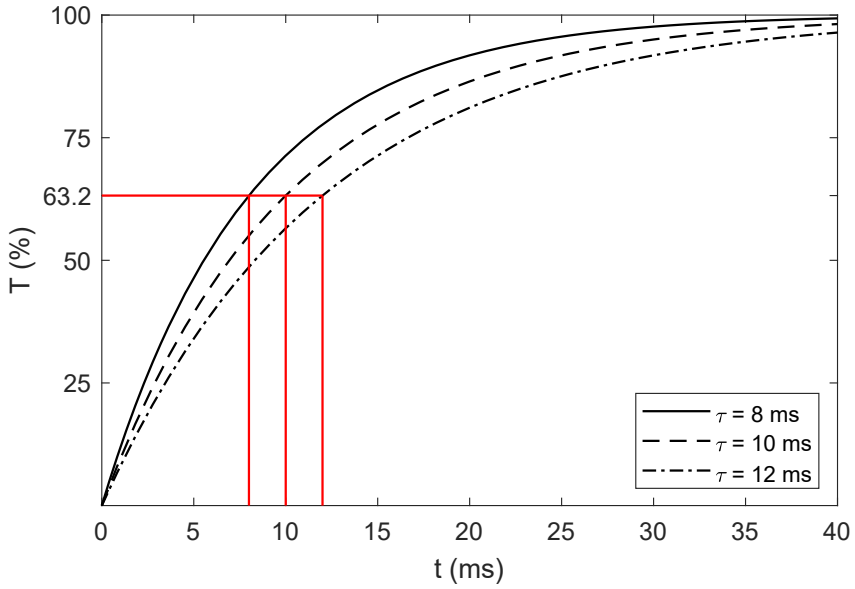


***Figure 2.6*** *Change in the temperature of a microbolometer pixel as a function of time for different values of thermal time constant $\tau$.*

The absorbed radiation of the membrane will generate a temperature increase. The specific heat capacity and absorptivity of the pixel will affect the change in temperature, which will then change the electrical resistance of the pixel. A bias current is applied through the sensor and as the incident radiation heats up the membrane this will cause a change in the measured voltage. Both the constant bias current and pulse bias current are used in microbolometers. The main advantage of pulsed bias is reduced power consumption i.e. reduced heating of the sensor caused by the measurement. (Khandpur, 2014)

A *relative temperature coefficient of resistance* (TCR) can be defined for the thermal

detector as

$$\alpha_T = \frac{1}{R}\frac{dR}{dT}, \tag{2.28}$$

where $R$ is the electrical resistance of the detector. So the voltage change of the detector can be presented as

$$\Delta V = I_b \Delta R = I_b R\ \alpha_T \Delta T, \tag{2.29}$$

where $I_b$ is the bias current. (Rogalski, 2010, p. 104)

Thermal detector should have a large TCR. In practice, the larger the TCR is the smaller change in temperature will cause a noticeable change in the resistance of the detector. The TCR also has an impact on responsivity and flicker noise of microbolometers. (Wang et al., 2013) Noise sources of IR systems are discussed in Subsection 2.2.5, while figures of merit, like responsivity, are introduced better in Subsection 2.2.6.

### 2.2.2 Photon detectors

The main difference between thermal detectors and photon detectors is that the temperature of the sensing elements will change in thermal detectors, while the photon detectors will measure the number of incident photons. Photon detectors utilize a semiconductor, e.g. InSb, as the detector material. (Kasunic, 2011) The electrical conductivity of semiconductors is between the conductivities of metals and insulators (Yu and Cardona, 2001, p. 1). The photon detectors are typically working in MWIR band. Detectors working in this range are very sensitive to small temperature differences because of the high thermal contrast in MWIR band, as discussed in Subsection 2.1.5. (Gade and Moeslund, 2014, p. 248)

Simplified working principle of photon detectors is based on the *bandgap* of the semiconductor material. This bandgap is the energy difference between *valence* and *conduction* bands and usually it is between zero and 4 eV. (Vincent et al., 2015; Yu and Cardona, 2001) Valence band is the lower band and it is full of electrons. The upper band called conduction band is empty. When an electron within the valence band is excited due to external energy e.g. an incident photon, it is moved to the conduction band, as illustrated in Figure 2.7. This leaves an empty state in the valence band, called *hole*. Movement of charge carriers, i.e. holes in the valence

band and electrons in the conduction band, is measured as a current. (Harrison and Valavanis, 2016, p. 56)

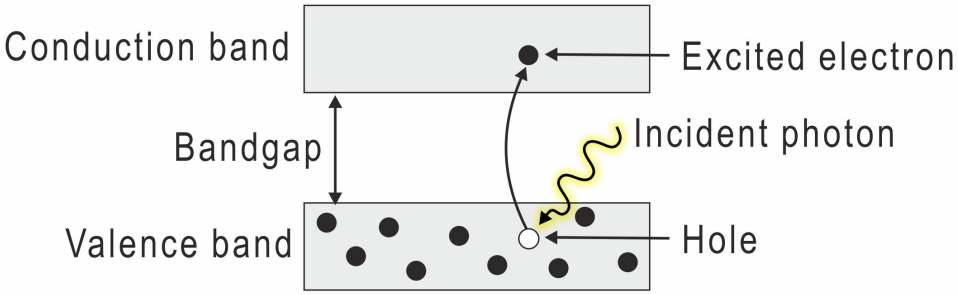


***Figure 2.7*** *An incident photon excites an electron within the valence band and the electron is moved over the bandgap to the conduction band.*

The energy of the incident photon must be higher than the bandgap energy between the valence and the conduction bands. If the incident photon arriving to the surface of the semiconductor material has enough energy, it can excite an electron initially bound to atoms and create a free electron-hole pair. (Kasunic, 2011) If the energy of an incident photon is not high enough, the photon will just go through the material (Vincent et al., 2015, p. 144).

In an ideal case one incident photon with a suitable energy would excite one electron, but on average, one photon will convert less than one electron. Reflection of the photons at the detector surface, incomplete absorption because of the thin absorption layer and poor material quality will reduce the number of converted electrons. (Kasunic, 2011)

So the absorptivity of a semiconductor material determines if the charge carriers are produced and photocurrent created. This depends on the *absorption coefficient* $\alpha$ of a semiconductor material. (Zimmermann, 2009, p. 4-5) The absorption coefficient for a semiconductor material with a bandgap energy of $E_g$ is determined as

$$\alpha(E_p) = b(E_p - E_g)^{1/2}, \tag{2.30}$$

where

$$E_p = \frac{hc_0}{\lambda} \tag{2.31}$$

is the energy of incident photon and $b$ is a constant that depends on the semiconductor material (Rogalski, 2002, p. 12). Figure 2.8 shows the absorption coefficients

and the corresponding radiation penetration depths of different detector materials. As one can see, the absorption coefficient is a function of wavelength and so the wavelength range in which the carriers are generated is limited for a given semiconductor (Rogalski, 2003a, p. 71).

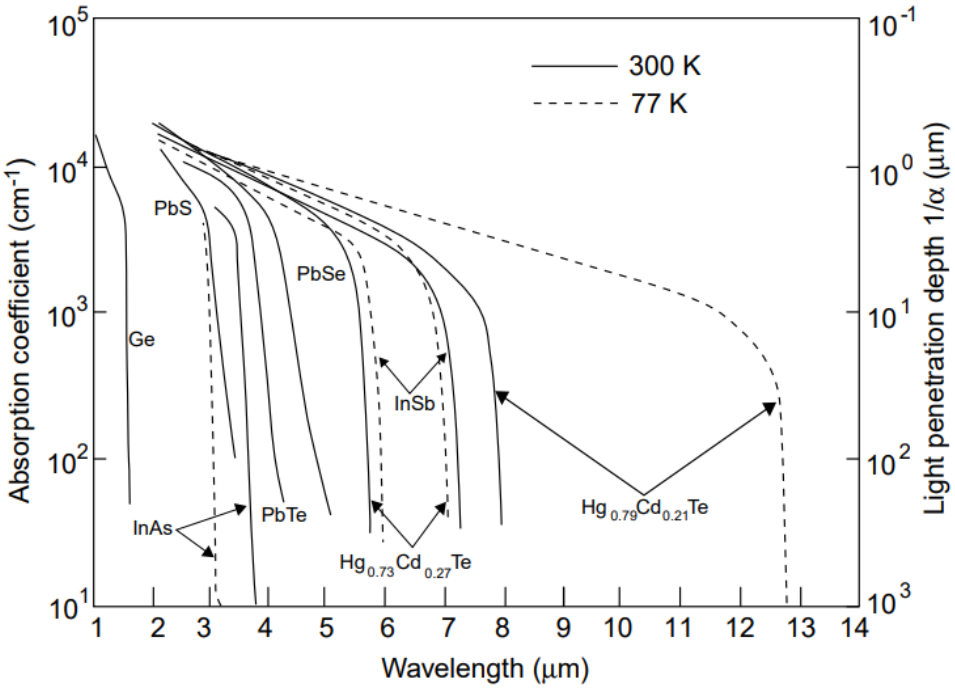


***Figure 2.8*** *Absorption coefficients and corresponding radiation penetration depths of different semiconductor materials. (Rogalski, 2003a, p. 71)*

Only some of the incident photons will create charge carriers. This fraction is described by *quantum efficiency* $QE$ and if reflection coefficient is negligible it can be solved as

$$QE = 1 - exp(-\alpha x), \tag{2.32}$$

where $x$ stands for thickness of the sensing element. (Rogalski, 2003b) Figure 2.9 presents quantum efficiency values as a function of wavelength for different detector materials.

The carrier generation rate of the detector can now be presented as

$$\dot{N}_c = QE\ N_p A_e, \tag{2.33}$$

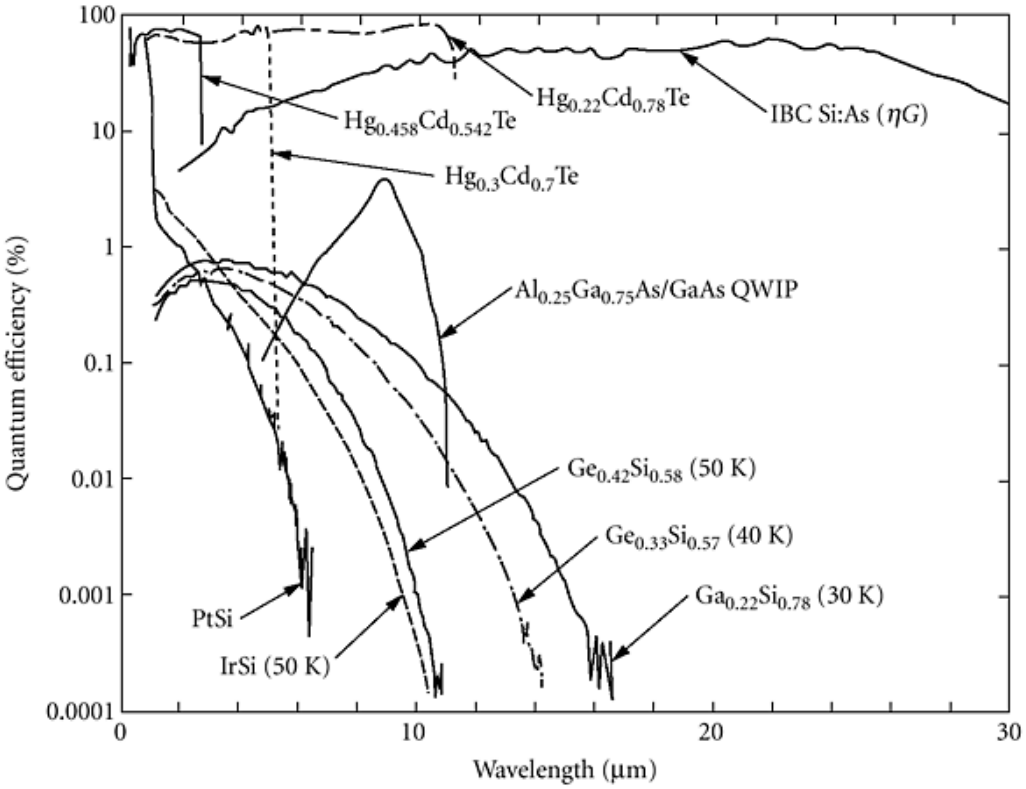


***Figure 2.9*** *Quantum efficiency as a function of wavelength for different detector materials. (Bass, 2010)*

where $N_p$ is photon irradiance. $A_e$ is the effective area of the detector i.e. the ideal detector area multiplied by the fill factor, which is explained in Subsection 2.2.3. (Vincent et al., 2015, p. 157)

The detector feature called *responsivity* $\mathcal{R}$ is the signal output divided by the radiation input. Many units can be used to describe the responsivity, but the most common one describes the amount of current that a watt of radiation power at a specific wavelength can produce ($A/W$). (Vincent et al., 2015, p. 160) Because absorption depends on wavelength and the absorptivity of a semiconductor decreases with longer wavelengths, one could assume that the responsivity of a semiconductor detector would decrease too. However, the responsivity of the detector increases with wavelength up to a certain cutoff point. This can be explained with photon energy, which is inversely proportional to wavelength, like one can see in Equation 2.31. This means that to create a watt of radiation power, more photons per second are needed as their wavelength is getting longer. Because the number of excited electrons depend on the number of incident photons, one watt of photons will create a greater photocurrent and so a higher responsivity with a longer wavelength, like one can see in Figure 2.10. With thermal detectors, only radiation power will

affect the rise in temperature and in principle, the responsivity is independent of wavelength. (Kasunic, 2011)

In Figure 2.10, one can see that at first the responsivity increases with wavelength, but above a certain wavelength, it suddenly decreases to zero. This drop occurs when the energy of an incident photon is under the bandgap energy $E_g$ and it defines the *cutoff* wavelength, beyond which the responsivity of the detector will drop. The maximum value of the responsivity curve occurs when the wavelength of photons is about 90 percent of the cutoff wavelength. (Kasunic, 2011)

For some detector materials, e.g. silicon and InSb, the bandgap and so the maximum wavelength are fixed, while the bandgap of some materials, e.g. MCT and InGaAs, can be modified. For example, often the composition of indium gallium arsenide is $In_{0.53}Ga_{0.46}As$, but also other compositions are used to shift the responsivity maximum, as shown in Figure 2.10. (Kasunic, 2011)

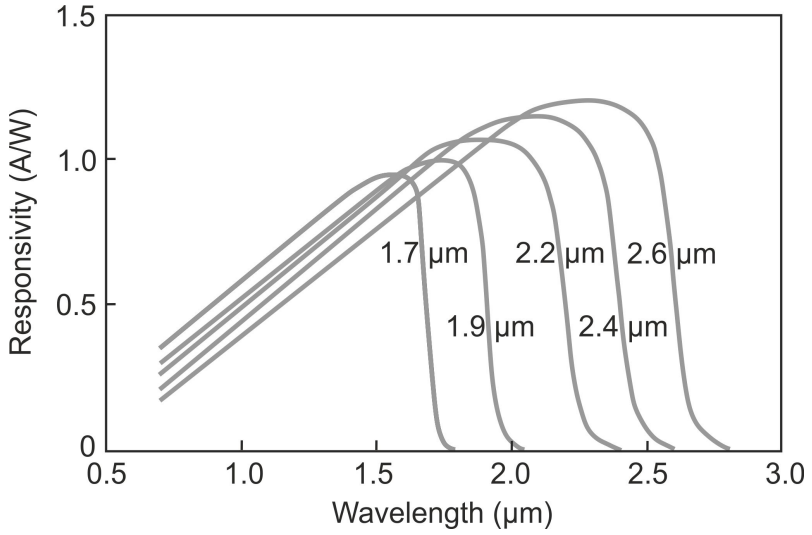


***Figure 2.10*** *Responsivity as a function of wavelength for InGaAs detectors with different compositions. The cutoff wavelengths of the detectors are marked in the figure. Adapted from Kasunic (2011)*

As the energy of incident photons creates charge carriers, also the thermal energy of the detector can excite bounded electrons and so create a *dark current*. This current exists in the detector even though there are no incident photons coming to the detector. Besides the temperature, it depends on the size, bias, material, quality and design of the detector. The reduction of dark current is the biggest reason why cooling of the photon detectors is needed. (Kasunic, 2011; Vincent et al., 2015) Photon detectors are cooled to cryogenic temperatures using a structure called Dewar flask with e.g. liquid nitrogen or a small Stirling cycle refrigerator

unit. The detector is attached to the cold side of the cooler, so the heat caused by the detector is conducted away. Cooling requirements make the photon detectors bigger, heavier and more expensive than thermal detectors. (Rogalski, 2003a; *The ultimate IR handbook* 2012)

A photoconductor, the simplest photon detector, contains only one thin layer of semiconductor, whereas a photovoltaic detector combines (at least) two semiconductor layers to a p-n junction (Kasunic, 2011). In following subsections, both photon detectors are introduced as well as a more complex detector called quantum well IR photodetector.

### Photoconductors

The simplest and least expensive photon detectors are photoconductors. They contain one thin layer of semiconductor e.g. MCT or germanium. The simplified structure of a photoconductor is presented in Figure 2.11. As mentioned earlier, absorbed photons excite bounded electrons and this increases conductivity of the detector material. Thus the conductance varies with incident photon flux and conductivity is measured as a change in the voltage (or current) of the photoconductor. (Kasunic, 2011)

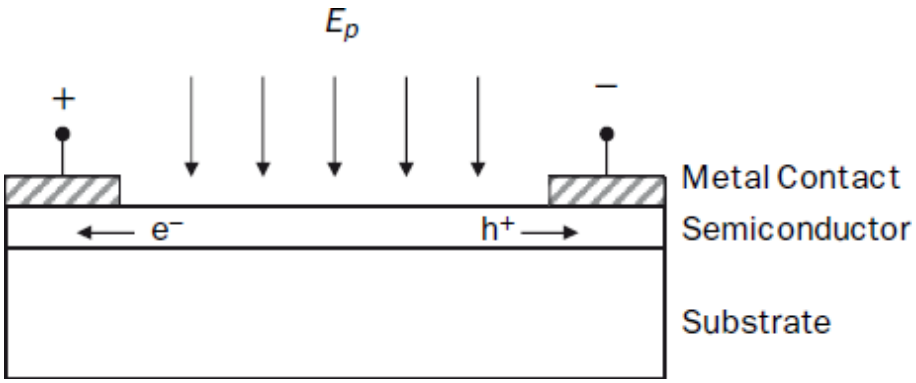


***Figure 2.11*** *The structure of a photoconductor. The energy of incident photons ($E_p$) creates free electron-hole pairs. Free electrons ($e^-$) move to the positive anode and holes ($h^+$) move to the negative cathode. (Kasunic, 2011)*

Photoconductors that use non-doped semiconductor materials are called *intrinsic* detectors and they generally have a larger bandgap energy and thus are used for short wavelength detection. The energy of an incident photon has to be large enough that the electron excites from the valence band to the conduction band. (Kasunic, 2011; Bass, 2010)

Photoconductor material can also be doped with other material to reduce the excitation energy of electrons. In this type of photoconductor, electrons (or holes) are excited into the conduction band (or valence band) from states within the band (e.g. impurity-bound states, quantum wells or quantum dots) and is therefore called *extrinsic* detector. Doped photoconductors are usually more sensitive to longer wavelengths than thermal and photovoltaic-based detectors. (Bass, 2010; Rogalski et al., 2018) Figure 2.12 illustrates the difference in excitation energy of intrinsic and extrinsic detectors.

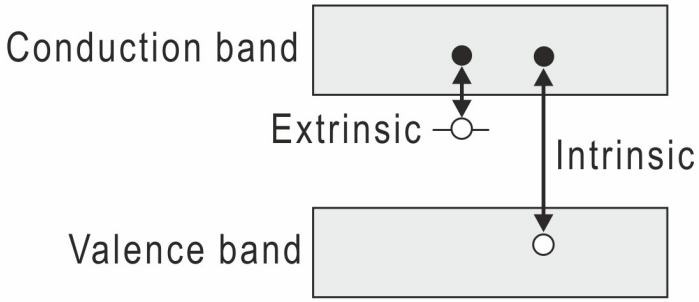


***Figure 2.12*** *The excitation energy needed of intrinsic and extrinsic detectors. In intrinsic detectors an electron is excited from the valence band to the conduction band, whereas in extrinsic detectors an electron is excited into the conduction band from state within the band. Adapted from Bass (2010).*

Extrinsic detectors require more cooling than intrinsic detectors to achieve high signal-to-noise ratio. The cooling requirement is associated with LWIR band. This is because the energy levels of extrinsic detector are close to each other and this induces thermal transitions between them, thus increasing the dark current. For example, an intrinsic MCT photoconductor is cooled down to 77 K, while an extrinsic one must be cooled below 40 K when photoconductor operates out to 15 to 20 µm. Flicker noise that associates almost with all electronic devices may also dominate, especially at longer wavelengths as its density is higher in low frequencies. (Bass, 2010; Rogalski et al., 2018)

One absorbed photon will excite one bound electron if there is no applied voltage. However, if voltage is applied across the semiconductor one photon can excite even 10–1000 electrons. This *gain* of the photoconductor depends on the material and how slowly-moving holes it contains. One should remember that electrons are moving across the semiconductor film to the anode and holes to the cathode. Every electron that will reach the anode will be measured as current. Because holes are typically moving slower in a crowded valence band than free electrons in a conduc-

tion band, electrons that will reach the anode earlier will cause a charge imbalance. To correct this, an additional electron is released from the cathode into the semiconductor. Many electrons can reach the anode during the time the hole will reach the cathode. This determines the number of free electrons that one photon creates and so order the gain of the photoconductor. For example, in many devices the lifetime of one hole is 10–1000 times longer than the travel time of an electron. The lifetime of holes and so the gain of a photoconductor affects how rapid signal changes can be measured with the detector. Silicon photoconductor with a high gain has a speed of $10^3$–$10^6$ Hz, while InGaAs photoconductor with a low gain will exceed $10^9$ Hz speed. (Kasunic, 2011) So high gain increases the responsivity of the detector but on the other hand makes it slower (Bass, 2010).

Temperature and electrical resistance influence the noise levels of detectors. Thermal motion of electrons and fluctuating number of electrons in the conductive layer cause noise. The lifetime $\tau_c$ of holes determines the frequency level ($f = 1/\tau_c$) above which the thermal noise is dominating and the gain mechanism has no point. Otherwise, due to the number of electrons, generation-recombination noise is dominating in photoconductors and that noise is almost double the inherent noise (i.e. shot noise) of photovoltaic detectors. More about different noise sources are discussed in Subsection 2.2.5. In summary, photoconductors are typically slower and noisier than photovoltaic detectors. They are usually low-cost devices with a low-end performance. (Kasunic, 2011)

### Photovoltaic detectors

Compared to photoconductors, photovoltaic detectors are slightly more complex, and this makes them generally more expensive. Basic operation principle is yet similar to photoconductors: a photon is absorbed by the sensing element and the energy of the photon will excite a bound electron. (Kasunic, 2011)

The simplest photovoltaic detector is a diode that contains two layers of semiconductor material, deposited one on top of the other. The layers are doped with materials that contain either extra electrons (n-layer) or extra holes (p-layer). The interface of these two layers is called *p-n junction*. (Kasunic, 2011) The p-n junction structure is presented in Figure 2.13. Free charge carriers will diffuse to the other side of the junction, depending on the charge of the carrier. This will create a *depletion layer* (marked in Figure 2.13 with dashed lines) that has no free charge carriers. On the other side of this layer there is a positive net charge and the other side a negative net charge. This will result a charge imbalance and therefore cause a local *built-in*

*electric field*. (Vincent et al., 2015)

Like in photoconductors, an incident photon with enough energy will create an electron-hole pair in the p-n junction. The local electric field will move those charge carriers away from the junction and so a measurable photocurrent is created. This phenomenon is called *photovoltaic effect*. Due to the low absorptivity of the thin junction, incident photons are not generating electron-hole pairs efficiently. Although charge carriers are also generated outside the p-n junction, the excited electron can recombine (reverse to the generation of free electrons) before it is measured as a photocurrent. (Kasunic, 2011)

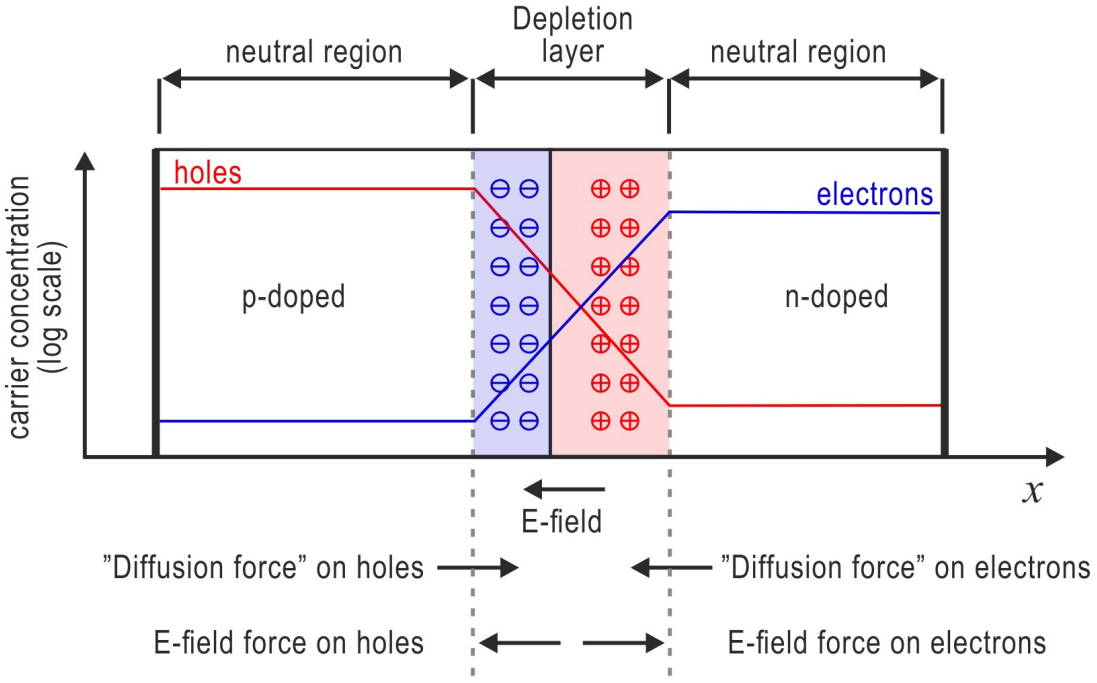


***Figure 2.13*** *A p-n junction in equilibrium. The concentrations of electrons and holes are marked with blue and red lines, respectively. The depletion layer is marked with dashed lines. Directions of the electric field and the diffusion force are shown on the bottom. Adapted from Johnson (2003).*

To improve the performance of the photodiode, a negative voltage i.e. a reverse bias is applied across the junction which will increase the electric field. As a result, the depletion layer will become slightly thicker. A stronger field will also increase the speed of electrons. As a down side, by increasing the reverse bias the noise level of the detector will also increase. (Kasunic, 2011)

The efficiency and speed can also be increased by adding a third not doped layer (an intrinsic layer) between the n and p layers, creating a *p-i-n* photodiode (PIN). The intrinsic layer is thicker than the depletion layer of a p-n junction and this

will provide better absorptivity close to the electric field and so result a higher responsivity. An additional layer will also reduce diffusion time and capacitance and so provide a faster response, which is advantageous to high-frequency applications. (Kasunic, 2011)

By adding a fourth, p-type layer between intrinsic and n-layers, one can create an *avalanche* photodiode. This will create a gain to the diode structure because one photon can produce more than one electron, similarly as in photoconductors, although this requires a larger voltage than PIN diodes. The other drawback is that the avalanche diode has an additional noise component, that will increase with the gain value. However, with an optimum gain value the avalanche diode with a higher responsivity can be a better choice than a PIN diode with a noisy amplifier. (Kasunic, 2011)

### Quantum well infrared photodetectors

One can create a unique band structure by stacking few atoms thick layers of two or more materials. The detectors using this engineering technology are called *quantum well* (QWIP), *quantum dot* (QDOT) or *strained layer superlattice* (SLS) IR photodetectors. (Vincent et al., 2015, p. 203) The structure and working principle of the QWIP are described in this subsection.

The IR radiation detection of QWIP can be explained by basic principles of quantum mechanics i.e. a particle in a box model, which can be solved by the Schrödinger equation. The solution describes the energy levels inside the quantum well where a particle (e.g. an electron) can exist. The dimensions of a quantum well mainly determine the energy level positions. For example, the energy levels of the quantum well with infinitely high barriers and width of $L_w$ can be solved from

$$E_j = \frac{\hbar^2 \pi^2 j^2}{2m^* L_w^2}, \tag{2.34}$$

where $\hbar = h/2\pi$ stands for the reduced Planck's constant, $j$ is an integer (1, 2, 3, 4...) and $m^*$ is the effective mass of the particle in the quantum well. (Gunapala and Bandara, 1999, p. 1057)

Although QWIPs are grouped with extrinsic photoconductive detectors, they still have many properties better than classical photoconductors. For instance, QWIP devices have highly evolved production technology and as a main advantage, they

have a high uniformity between sensing elements which allows to produce large arrays. (Kukkonen et al., 2001; Rogalski, 2006) QWIPs are manufactured by using the semiconductor crystal growth technology e.g. molecular beam epitaxy. This technology makes it possible to manufacture structures with atomic layer control. (Paiella, 2006)

The basis of QWIP is to use layered wide bandgap semiconductor materials (e.g. GaAs and AlGaAs) and create quantum wells with low effective bandgaps within the valence band or the conduction band (Rogalski, 2003b). This way the excitation of charge carriers takes place within the band and so the absorption of a photon is called *intersubband absorption* (Kukkonen et al., 2001; Paiella, 2006). Figure 2.14 shows the low effective bandgaps of the quantum well within the valence band and the conduction band.

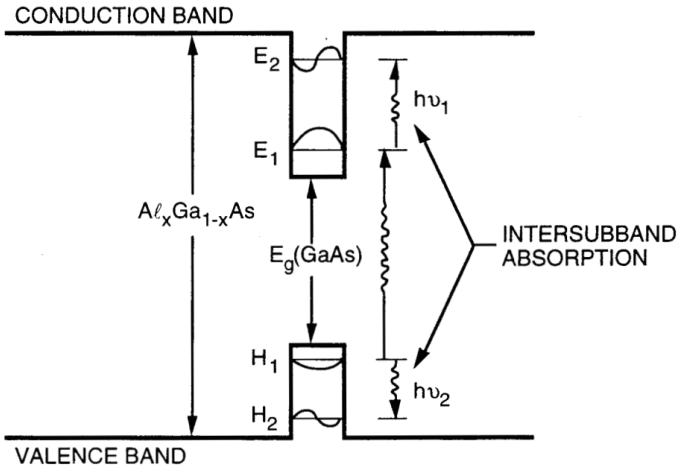


***Figure 2.14*** *The schematic bandgap structure of quantum wells within the valence band and the conduction band. An incident photon will excite an electron within the conduction band or a hole within the valence band, in which case an intersubband absorption occurs. (Kukkonen et al., 2001)*

The structure of a quantum well is created by depositing thin layers of materials with different bandgap energies. Usually a layer of GaAs is deposited between two layers of $Al_xGa_{1-x}As$. The number of ground state electrons or holes are controlled by doping the GaAs. The GaAs layer, with a smaller bandgap, is acting as well structure, while the $Al_xGa_{1-x}As$ layers, containing a larger bandgap, are forming the barriers on both sides of the well. The width of the well is controlled by changing the thickness of the GaAs layer and the depth by changing the Al composition of the potential barrier layer. (Kukkonen et al., 2001, p. 398)

By adjusting the size of the well, well-defined energy states can be created e.g. the ground state located at the bottom of the well and the first excited state at the

top of the well (Kukkonen et al., 2001, p. 398). Depending on the position of the first excitation state in the quantum well, the dark current and the responsivity of the detector are varying. By changing the dimensions of quantum wells, the needed excitation energy can be adjusted over a wide spectral range, from SWIR to FIR. (Gunapala and Bandara, 1999, p. 1058)

Multiple quantum well structures are then stacked to create a photon detector (Figure 2.15). The structure acts like other photon detectors: an incident photon will excite an electron in the ground state into an excited state. Applied external voltage will then move the excited electron and so create a photocurrent. (Kukkonen et al., 2001, p. 398)

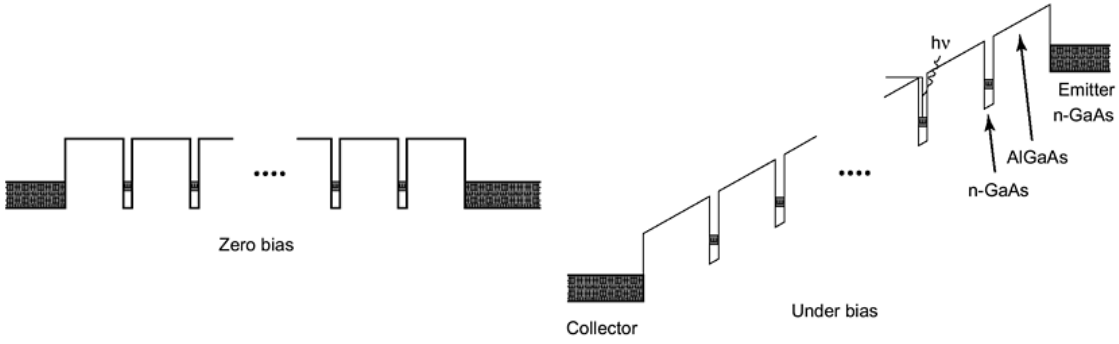


***Figure 2.15*** *Stacked quantum wells within the conduction band. In the left figure there is a zero bias, while in the right figure the bias voltage is applied. Adapted from Paiella (2006)*

The absorption quantum efficiency of QWIPs is small compared to InSb and MCT detectors. Because QWIP is a photoconductive detector, the gain value also affects the responsivity of the detector. As the gain of QWIPs is typically 0.4, the quantum efficiency stays below 10 %. Because of this, longer integration times, typically 10 to 100 times longer, are used with QWIPs than with InSb and MCT detectors. (Diakides et al., 2017; Rogalski, 2002) However, the small gain increases the signal-to-noise ratio of the detector. (Rogalski, 2006, p. 3514)

Although the spectral response of QWIP can be adjusted to a wide spectral range, the bandwidth of spectral range is relatively narrow. QWIPs need more cooling (typically to 60 K) than InSb and MCT detectors to reduce dark current. (Diakides et al., 2017) In summary, QWIPs are ideal for IR cameras with a large resolution and a low frame rate with a long integration time (Rogalski, 2006, p. 3514).

### 2.2.3 Focal plane array

Variety of individual sensing elements used in IR detectors were introduced in previous subsections. One sensing element can be used to measure the total irradiance of the scene, however more than one is needed to create a *thermal image* of the scene. In this case, multiple individual sensing elements are integrated together to form a two-dimensional array called *focal plane array* (FPA). The FPA is placed at the focal plane of the camera lens and besides the sensing elements, it also contains readout electronics to measure the created signal e.g. current, voltage or resistance, to digitize the signal and then to construct the thermal image of the scene. (Kasunic, 2011; Vincent et al., 2015) Individual pixels have dimensions in microscale and an IR FPA usually contains from 60 000 to more than 1 000 000 pixels. The resolution of an IR FPA can range from less than 160 x 120 pixels up to 1024 x 1024 pixels. (*The ultimate IR handbook* 2012, p. 9) Some detectors, e.g. QWIPs require optical grating to disperse the incident radiation to increase the absorption. This is because the QWIPs cannot absorb radiation at normal incidence as the electric field of the radiation is parallel to the plane of the quantum well. (Ryzhii, 2003; Zhang et al., 2013)

In addition to resolution, important features that affect the way an FPA operates are for example fill factor, non-uniformity and delay in reading out the pixel data. The *fill factor* describes the ratio between a radiation sensitive pixel area and a pitch area (Figure 2.16). The smaller the fill factor the bigger are the gaps between pixels that cannot detect incident radiation. (Kasunic, 2011)

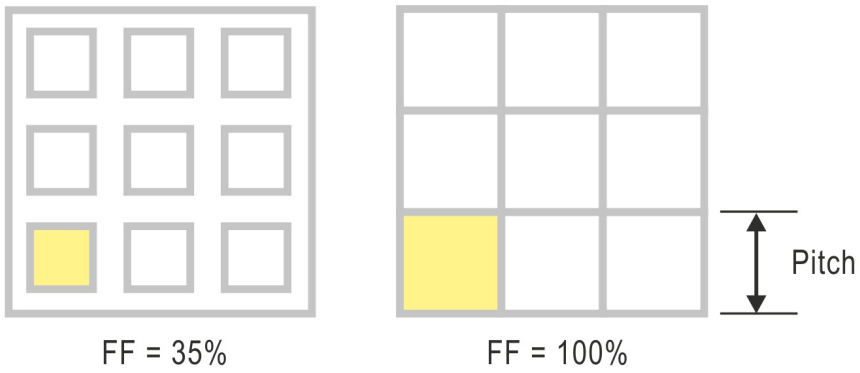


***Figure 2.16*** *The fill factor (FF) of an FPA is the ratio of a radiation sensitive pixel area (yellow area) to a pitch area. In left side figure the FF is only 35 % when in right side it is 100 %.*

Response to incident radiation can differ between pixels even with a uniform scene

and this is causing *non-uniformity* of the FPA. The reason for this is the manufacturing process as the concentration of the dopants, the layer thickness and the relative proportions of different semiconductor materials can vary between pixels of the same FPA. This can reduce the image quality and the signal-to-noise ratio if it is not corrected. Performing the non-uniformity correction (NUC) before using the IR camera is extremely important as one can discover in Section 3.3. (Kasunic, 2011)

Individual pixel can respond to radiation changes within microseconds, but it will take longer to read the signal of every pixel on the FPA and so create a *frame*. The time it takes to collect and read out the data of all pixels affects the *frame time*, from which the *frame rate* is obtained. Generally, a higher frame rate can be reached with a smaller array, however the detector type also has an effect on the frame rate. For example, with microbolometers, even with a low resolution, a suitable frame rate is usually around 30 Hz due to the slow response of the sensing elements. With photon detectors a frame rate up to 1000 Hz can be reached. Even higher frame rates can be achieved with a technique called *windowing*, where the data is read out only from a smaller subarray of the FPA. (Kasunic, 2011)

Many features mentioned above depend on the readout electronics used to measure and process the created signal of the sensing elements. There are currently three different technologies: charge-coupled device (CCD), complementary metal-oxide semiconductor (CMOS) and hybrid arrays. (Kasunic, 2011)

CCD FPA was used in early imaging devices in both visible and IR ranges, and its operation can be divided in four different phases: charge generation, collection, transfer and measurement. The problem with a CCD FPA is that some of the electrons can be lost as they are transferred to the end of a pixel row, where they are read out and processed. A solution to this issue is the CMOS FPA, that forms integrated circuits taking advantage of complementary metal-oxide-semiconductor field-effect transistors (MOSFET). In CMOS FPAs, the readout and processing circuits are included into each pixel. Each pixel converts collected charge to voltage by themselves. This means that no electrons are lost because of the charge transfer. Individual pixels can also be read out separately, thus it enables windowing. (Kasunic, 2011; Janesick, 2001; Vincent et al., 2015) The simplified structure and principle of operation of CCD and CMOS FPAs are introduced in Figure 2.17.

The sensing element and readout electronics are integrated into the same silicon chip in CCD and CMOS FPAs. These technologies can only be used in imaging devices that work on a spectral range to which silicon is sensitive. (Kasunic, 2011) This

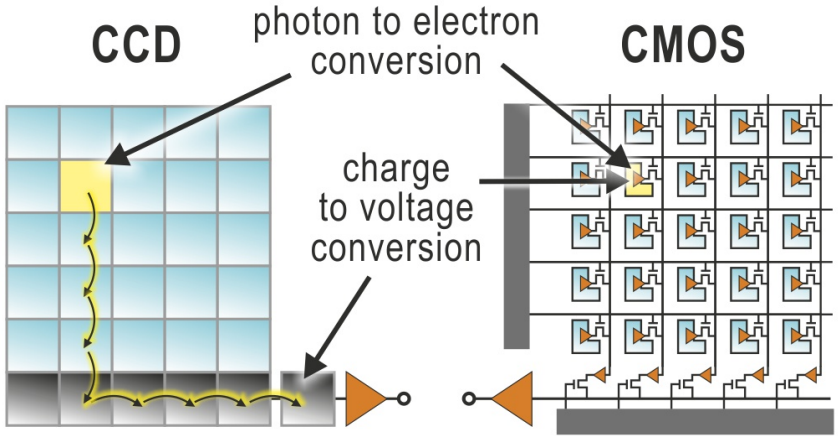


***Figure 2.17*** *Performance difference between CCD and CMOS FPAs. In a CMOS device the collected charge is measured and processed in the pixel, whereas a CCD device transfers the collected charge to the end of the pixel row, thus making the drain of electrons possible. Adapted from Meroli (n.d.)*

monolithic structure can be used in uncooled IR devices such as microbolometers and in photon detectors working in visible or in NIR range (Vincent et al., 2015, p. 232).

Typically, IR photon detectors are working in other spectral ranges and thus require different semiconductor materials for sensing. In these cases, the sensing element array is mounted i.e. *hybridized* to the ROIC with e.g. indium bumps, like one can see in Figure 2.18. (Kasunic, 2011; Diakides et al., 2017) This is because of manufacturing high-quality CCDs and transistors from IR sensitive materials is difficult. So ROIC and sensing element array can be individually optimized. (Vincent et al., 2015, p. 231, 235-236)

### 2.2.4 Signal detection

When observing the output signal $I$ of the pixel one can obtain three main components:

$$I = I_{signal} + I_{back} + I_{dark}, \tag{2.35}$$

where $I_{signal}$, $I_{back}$ and $I_{dark}$ are the currents of the examined signal, background and dark current, respectively. A large background radiation or a significant dark current makes it hard to detect the target signal. (Kasunic, 2011)

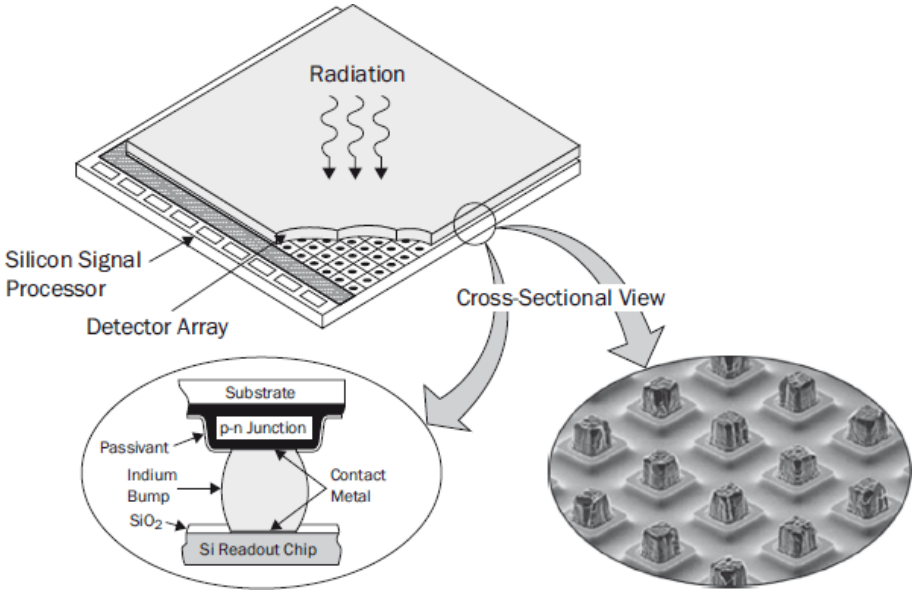


***Figure 2.18*** *Sensing element array hybridized to a silicon ROIC with indium bumps. (Rogalski, 2003c)*

As the signal is changing over time, the sensing element together with other electronics has to respond fast enough. The electrical bandwidth is the difference between the lowest and the highest frequency of the detected signal. It is also one factor that affects how rapid events the detector can distinguish. With a wider bandwidth the shorter events can be detected. Usually this is approximated as

$$\Delta f \approx \frac{1}{2\Delta t}, \tag{2.36}$$

where $\Delta t$ is the time factor specified according to the event. There are different time factors e.g. detector response time, integration time (of the bias pulse in case of microbolometer) and frame time. Any one of these time factors can be used to determine the bandwidth $\Delta f$ of the detector. (Kasunic, 2011; Kohin and Butler, 2004)

When there are rapid events occurring in the scene the *response time* of the detector should be short enough to respond to the occurring events. In this case, the length of the event is used to determine the bandwidth, $\Delta t = t_{event}$. Usually one cannot know exactly when the desired event will happen and so the time that the detector measures an incident radiation should be longer than the time of the event. In the case of photon detector, this is known as *integration time*, the time that the "shutter" of the photon detector is open and collecting incident photons. (Kasunic, 2011)

Usually, the integration time is shorter than the frame time and also the scene is relatively static, in other words the scene is not containing events that are faster than the used integration time. In this case, the integration time determines the bandwidth, so $\Delta t = t_{int}$. Integration time is also used to determine the bandwidth in cases where the scene contains fast moving objects. The shutter has to be closed fast enough to prevent blurring of the object. (Kasunic, 2011)

### 2.2.5 Noise sources

Noise is defined as an unwanted disturbance in a desired signal. It is anything that prevents accurate reading of the target signal. Noise is attempted to be kept as low as possible, but it cannot be avoided entirely. There are sources of noise that are fundamental and unavoidable. These kind of noise sources are for example:

- Random arrival of photons
- Vibration of detector atoms (even in low temperatures)
- Random movement of electrons in the detector.

Other external noise sources that can be avoided:

- Electrical interference due to motors, AC power lines etc.
- Fluctuating temperature of the detector
- Shifting of electrical components caused by vibrations.

The noise caused by arriving photons determines the ultimate base of the noise level that cannot be eliminated. This photon noise is produced by random arrival of photons to the surface of the detector. (Vincent et al., 2015, p. 161) So the most basic noise source is the source itself. As the detector cannot separate the incident photons coming from the measured source or the background, also the latter has an effect on the noise level. This photon-caused noise differs depending if a photoconductor (PC) or a photovoltaic (PV) detector is used. (Kasunic, 2011)

Electrical bandwidth, or from here on called as noise bandwidth $\Delta f$ of the system has always an effect on noise level. Like discussed in previous subsection, the noise bandwidth is approximated as $\Delta f = 1/(2\ t_{int})$. One can notice next, that a wide bandwidth i.e. a short integration time will strengthen certain noise sources e.g.

photon caused noises and Johnson noise. With these kind of noise sources, increase in integration time will also increase the signal-to-noise ratio. Depending on the source, some noise components are appearing at specific frequencies, while others more uniformly at all frequencies acting like white noise. If the frequency of the examined signal is known, e.g. how rapidly the scene is changing, noise can be reduced by limiting the noise bandwidth. For white noise for example the noise current or voltage is proportional to the square root of the bandwidth. (Vincent et al., 2015; Kasunic, 2011)

### Shot noise and generation-recombination noise

The noises of PV and PC detectors differ according to the mechanism and names, but the causes are similar. In case of PV detectors, the noise is caused by randomly arriving charge carriers at the diode junction. This causes fluctuation in the current and it is called *shot noise*. First of all, the variation in the arrival rate of charge carriers can be presented as

$$\delta\dot{N}_c = \sqrt{2\dot{N}_c\Delta f}, \tag{2.37}$$

where $\dot{N}_c$ is the arrival rate of the carriers. The *variation* in current is called *noise current* $i_S$. Because the output current of PV detector is $I = \dot{N}_c\, q$, the noise current is $i_S = \delta\dot{N}_c\, q$, and thus

$$i_S = \sqrt{2\ \dot{N}_c\ q^2\ \Delta f}, \tag{2.38}$$

where $q = 1.602 \cdot 10^{-19}C$ is the elementary charge.

When $\dot{N}_c$ is replaced with current divided by the charge of an electron, one gets the shot noise of the PV detector:

$$i_S = \sqrt{2\ I\ q\ \Delta f}. \tag{2.39}$$

The shot noise is also depending on the level of illumination. Limiting level comes from the dark current ($I \approx I_{dark}$) when low-level signal is detected. Instead, if illumination level is high, the limiting shot noise is caused by the photocurrent of the signal ($I \approx I_{signal}$) or the background ($I \approx I_{back}$). (Bass, 2010; Vincent et al.,

2015)

With PC detectors the noise is due to the fluctuation in the current and it is called *generation-recombination (G-R) noise*. There are two reasons for this noise: the randomness of the carrier generation and the randomness of the carrier recombination i.e. varying lifetime of the charge carriers. The total fluctuation of these two processes can be presented as

$$\delta \dot{N}_c = \sqrt{4 \dot{N}_c \Delta f}, \tag{2.40}$$

where $\dot{N}_c$ is the generation (or the recombination) rate of the carriers. The cause of the generation can be either due to arriving photons or to thermal generation. Because the output current in PC device is $I = \dot{N}_c \, q \, G$ (where $G$ is the photoconductive gain) and so the noise current is $i_{GR} = \delta \dot{N}_c \; q \; G$, one can present:

$$i_{GR} = \sqrt{4 \; \dot{N}_c \; q^2 \; \Delta f \; G^2}. \tag{2.41}$$

When $\dot{N}_c$ is replaced, G-R noise of the PC detector is:

$$i_{GR} = \sqrt{4 \; I \; q \; \Delta f \; G}. \tag{2.42}$$

When comparing the noises of PV and PC detectors one can notice that the PC detector noise includes a factor 4 and PV a factor 2. PC detector also contains a gain value that is missing from the noise of the PV detector. So even though the gain of the PC detector is reduced when signal-to-noise ratio is calculated, it will always be better for PV than for PC devices. (Vincent et al., 2015, p. 162-164) One should notice that the gain of QWIPs is typically 0.4, thus this reduces the G-R noise of QWIPs (Rogalski, 2006, p. 3514).

### Johnson noise

*Johnson noise*, also known as *thermal noise* or *Nyquist noise* is electrically generated and it depends on the resistances of the detector and other components in the device. The cause of the Johnson noise is the thermal motion of electrons and so higher temperature will increase it, as the velocity of the electrons increases. The current of Johnson noise is given by

$$i_J = \sqrt{\frac{4kT}{R}\Delta f}. \tag{2.43}$$

One can see in previous equation that by decreasing the temperature or increasing the resistance one can reduce this noise current. (Kasunic, 2011)

Sometimes the photon generated current is not large enough to generate a measurable voltage drop fast enough. One can increase the speed in many ways, one is to lower the resistance. But as the decrease in the resistance will increase the photocurrent, it will also increase the Johnson noise current. So sometimes there is a trade-off between sensitivity and speed when the Johnson noise is dominating. (Kasunic, 2011)

The Johnson noise appears in resistive elements like in feedback and load resistors and in PC detectors. Instead, it does not occur in ideal diodes. (Vincent et al., 2015, p. 165-166)

### Other noise sources

*Flicker noise*, also called as *1/f noise* or *modulation noise*, is significant noise element in thermal detectors, but it appears in photon detectors too (Bass, 2010). Predicting of flicker noise is hard but in general, if the frequency of detected signal is $f$ and the spectral band is narrow, the square of the noise is proportional to the current and inversely proportional to the frequency. Usually unless the frequency is very low, the flicker noise is negligible. (Vincent et al., 2015, p. 167) In addition to thermal detectors, flicker noise can be dominating also in low-frequencies in PV and PC detectors as well as in other electronic devices e.g. transistors and resistors (Bass, 2010).

Along with flicker noise, *temperature (fluctuation) noise* is a major noise source in microbolometers. It is caused by the heat loss of the absorbing layer during the measurement time of the signal. This noise can be reduced by improving the thermal isolation of the detector. (Kasunic, 2011)

In addition to the detector, also other components of the electrical circuit are causing noise. For example, amplifier and analog-to-digital (A/D) converter following it are causing noise called *amplifier* and *quantization noise*. The latter depends on the number of bits into which the signal is converted and also the maximum number of electrons that can be collected i.e. capacity or depth of the well. The quantization

noise is usually given in units of electrons and it is given by

$$i_Q = \frac{L_d}{2^{N_b}\sqrt{12}}, \tag{2.44}$$

where $L_d$ is the depth of the well and $N_b$ is the number of bits. (Kasunic, 2011)

There are noise sources that are typical for FPAs. Non-uniformities in responsivity and amplifier gain between pixels are caused by variation in fabrication of array devices. This cannot be entirely fixed and so it is causing *spatial noise* to the device. Sometimes an identical signal is measured slightly different when it is read and this is known as *read noise*. Because this noise occurs once per frame, it is independent of the integration time. (Kasunic, 2011)

### 2.2.6 Figures of merit for infrared detectors

As we have learned, there is a variety of technologies that can be used for IR detectors. In Figure 2.19, the basic detectors, divided to thermal detectors (e.g. microbolometer) and photon detectors, are shown. Photon detectors are divided again to PV (e.g. InSb and MCT) and PC detectors. Amongst PC detectors, one can find intrinsic (e.g. InSb and MCT) and extrinsic (e.g. QWIP) photoconductors.

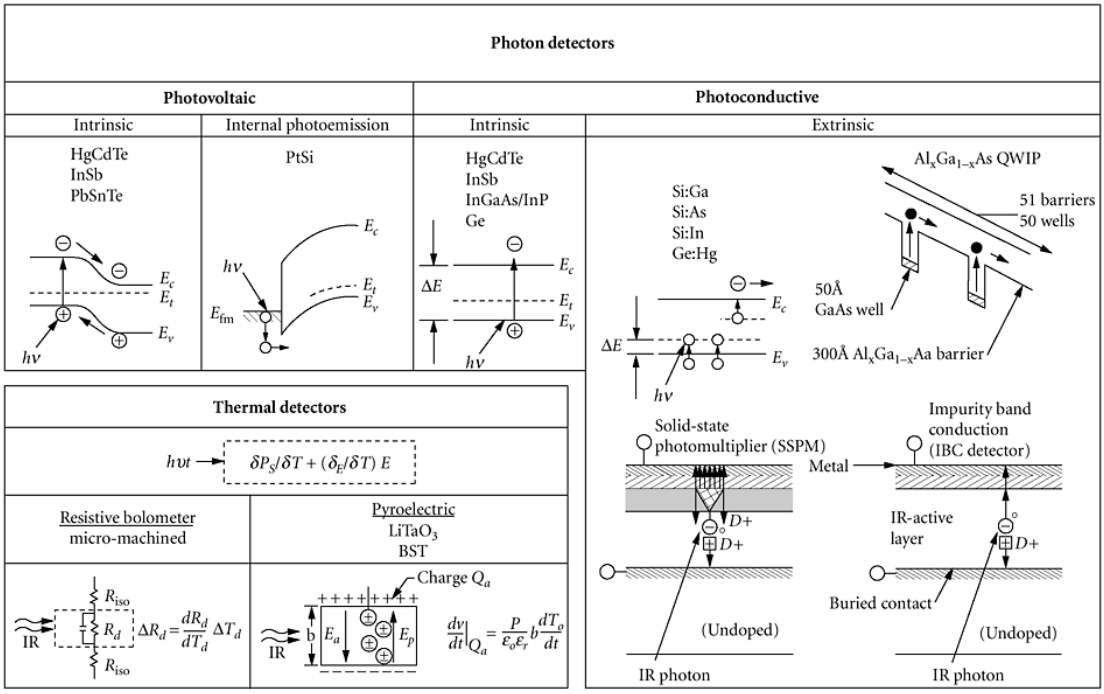


***Figure 2.19*** *Different photon and thermal detectors. (Bass, 2010)*

The material of the detector is causing many property differences. For instance, the spectral band of the given material should be considered when choosing the detector. (Kasunic, 2011) Commonly used materials in IR detectors with their spectral band are given in Table 2.2. With photon detectors, bandgap energy and absorption coefficient of the material affect how well the detector detects photons. Also, the lifetime and mobility of the charge carriers will determine the magnitude of the generated photocurrent. In some cases, the same material is suitable for both PC and PV detectors. In this case, a PV device is a better choice due to its better signal-to-noise ratio, simpler biasing and because the responsivity and noise level are more predictable. (Vincent et al., 2015, p. 156, 191) With thermal detectors e.g. microbolometers the TCR of the detector material affects the responsivity of the device (Wang et al., 2013).

***Table 2.2*** *Detector materials used in IR devices in different bands (Kasunic, 2011).*

| **Spectral band** | **Materials** | **Spectral range (μm)** |
|---|---|---|
| NIR | CdSe, Ge, MCT, InGaAs, Si | 0.7–1 |
| SWIR | Ge, MCT, InGaAs, InAs, PbS | 1–3 |
| MWIR | MCT, InSb, PbSe | 3–5 |
| LWIR | $\alpha$-Si, MCT, QWIP, VOx, Si:As | 8–12 |
| FIR | MCT, Si:As, Si:Sb | 12–30 |

There are many different parameters that are used to describe the performance of detectors or to compare the detectors to each other. One of these is the responsivity, which is already mentioned a couple of times. Responsivity will help to assess the amplification requirements e.g. to obtain the expected output. Regardless of what the input and output signals are, the responsivity is defined as the output divided by the input. Because the responsivity can be increased by adding the amplifier, the low responsivity is not that big of a problem. However, one cannot overcome the limitation of noise just by adding gain as it is also amplifying the noise. (Vincent et al., 2015, p. 41-43)

The *signal-to-noise ratio* (SNR) is the current (or voltage) of the signal divided by the current (or voltage) of the noise. By itself it does not tell about the detector as one can improve it just by increasing the irradiance of the target. Thus it rather tells the conditions under which the detector is working. (Vincent et al., 2015, p. 45-46)

Linearity instead describes how constant the responsivity of the detector will stay over certain range of irradiance. Frequency and spectral responses specify how

the responsivity varies with the electrical frequency or with the wavelength of the incident IR radiation. (Vincent et al., 2015, p. 48-50) Spectral response *per watt* of an ideal thermal detector is independent of wavelength, while spectral response *per photon* of an ideal photon detector is up to the cutoff wavelength independent of wavelength (Vincent et al., 2015, p. 145-146).

Like described in Subsection 2.2.5, noise is unwanted disturbance and it tends to hide the desired signal. So one should reduce the noise to improve the true signal. SNR then describe how "clean" the signal is. There are many figures of merit to define the quantity of the signal when SNR is 1. These are *noise-equivalent power* (NEP), *noise-equivalent irradiance* (NEI) and *noise-equivalent temperature difference* (NETD) that describe the amount of power, irradiance or temperature difference in the scene that produces a signal equivalent to the noise of the detector. (Vincent et al., 2015, p. 45, 169) Generally, the smaller the f-number the smaller i.e. the better is the NETD value of the IR camera (MoviTHERM, 2018).

Because the NEP formula does not consider the effect of the noise bandwidth and the size of the detector, concept of *detectivity* ($D^*$) was introduced (Vincent et al., 2015, p. 47-48). It can be calculated as

$$D^* = \frac{\sqrt{A_e \Delta f}}{NEP}. \tag{2.45}$$

In support website of IR camera manufacturer FLIR (FLIR Technical Support Center, 2019) is answered to the question about why the company is not providing $D^*$ specifications for its cameras. According to the company, it is obsolete figure of merit and it is not working well when FPA-type detectors are compared. They prefer the NETD instead of the $D^*$ because there are no assumptions or approximations used (e.g. with noise bandwidth) in calculations regarding the NETD.

According to the application support engineer of FLIR, Raphael Danjoux (2019), the NETD varies depending on the settings of the IR camera. For example, integration time of the cooled photon detectors affects the NETD value. NETD value is also affected by camera being used with or without a lens or a spectral filter. The NETD will also vary with the target's temperature. Noise is distributed unequally over the FPA, so it is natural that some pixels exhibit higher/lower NETD values than others. The NETD value represents the standard deviation of the measured data and it can be determined both for the temporal noise and for the spatial noise.

Figure 2.20 illustrates how FLIR calculates the temporal NETD of uncooled bolome-

ter cameras. This value is calculated from 32 sequential frames. The median value of each frame is subtracted from every pixel in each frame. After this, the standard deviation of each pixel as a function of time for 32 frames is calculated. Finally, the temporal NETD is the median value of all standard deviations. FLIR determines the temporal NETD value for cooled photon detectors a little different. For photon detectors FLIR also determines the responsivity of the camera, and the temporal noise of the camera is divided by the responsivity. (Danjoux, 2019)

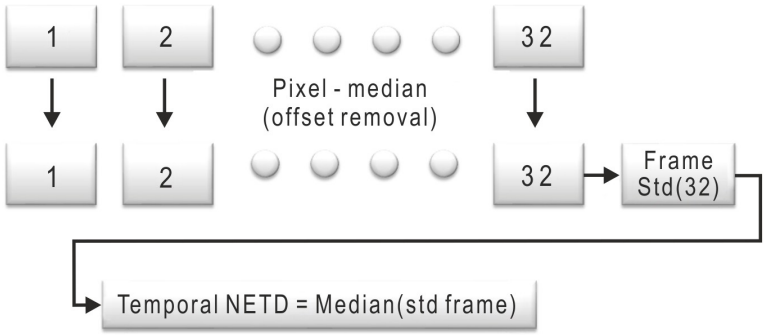


***Figure 2.20*** *FLIR's temporal NETD calculation for uncooled bolometer cameras. After removing the median value from every pixel in each frame, the standard deviation of each pixel as a function of time is calculated. The temporal NETD is the median value of all standard deviations. Adapted from Danjoux (2019).*

The spatial NETD is also calculated from 32 sequential frames as illustrated in Figure 2.21. First, an average frame is calculated by averaging the corresponding pixels of these 32 frames. The average frame is then divided into regions of $5 \times 5$ pixels. The standard deviation of each region is calculated and the spatial NETD is the median value of all standard deviations. (Danjoux, 2019)

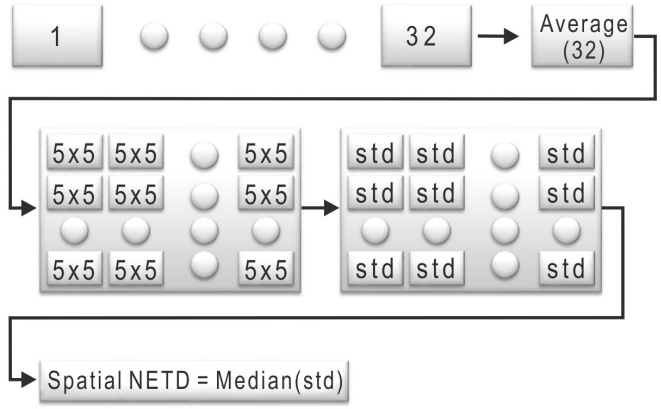


***Figure 2.21*** *FLIR's spatial NETD calculation for uncooled bolometer cameras. The frames are averaged into one frame and then divided into regions of* $5 \times 5$ *pixels. The standard deviation of each region is calculated. The spatial NETD is the median value of standard deviations. Adapted from Danjoux (2019).*

The total NETD of the camera can be calculated as

$$Total\ NETD = \sqrt{(Temporal\ NETD)^2 + (Spatial\ NETD)^2}. \tag{2.46}$$

FLIR provides only the temporal NETD for its cameras in specification sheets and this is usually called just NETD. As the NETD value of the camera only corresponds to temporal noise in certain conditions, one can compare the NETD values of different cameras only if the test conditions are the same for every camera. (Danjoux, 2019)

One should keep in mind that the NETD is not a value of the minimum temperature difference that can be measured. The NETD is the median value of the standard deviations of all pixels. So, assume that the NETD of a system is 0.02 ℃ at 25 ℃. A normalized Gaussian distribution presents the probability to have temperature X. According to the *Six-σ law*, the probability that the temperature X is comprised between 24.94 ℃ and 25.06 ℃ is 99.73 %, as can be detected in Figure 2.22. Thus one can be confident with a measurement where the temperature difference between two values is at least six times the NETD value. (Danjoux, 2019)

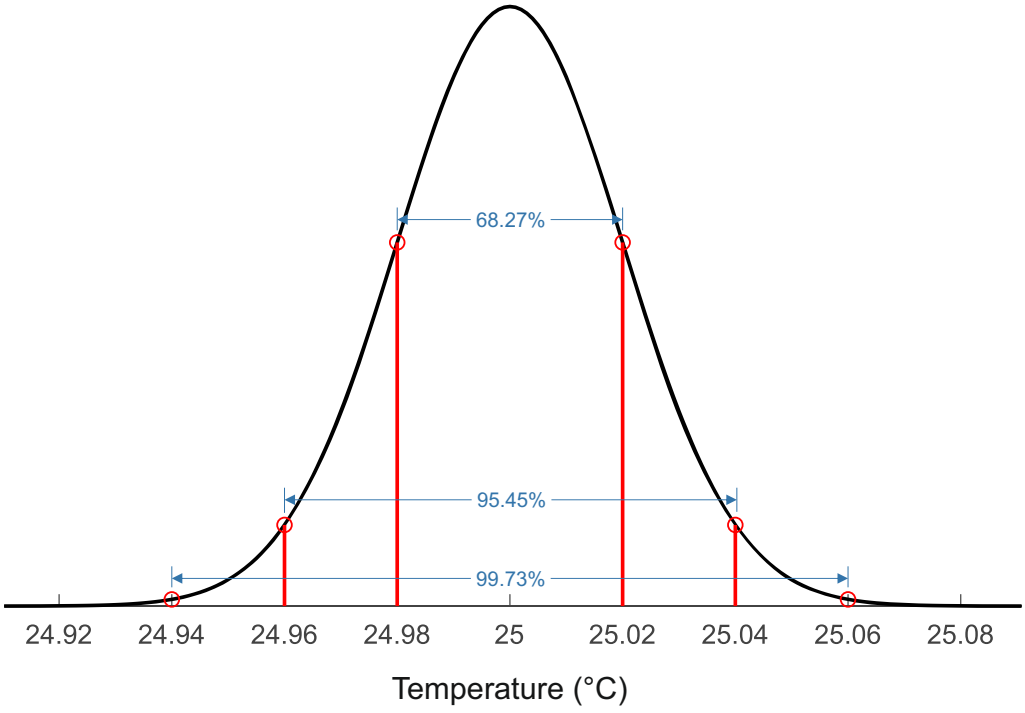


***Figure 2.22*** *Distribution of temperature values of individual pixels at 25 ℃ when the NETD is 0.02 ℃. Two, four and six times the NETD value will comprise 68.27 %, 95.45 % and 99.73 % of the temperature values, respectively.*

*Modulation transfer function* (MTF) determines how small details the detector can

measure, and it is dependent on the size of the detector and the response uniformity across the detector. It is sometimes called spatial frequency response. A small detector that has a uniform response has better MTF and so it detects smaller differences than a large detector. *Minimum resolvable temperature difference* (MRTD) combines NETD and MTF and it is a function of spatial frequency. MRTD defines the ability to distinguish small temperature differences between closely spaced or small features. (Vincent et al., 2015, p. 51-52, 175)

*Dynamic range* describes the difference between the lowest measurable signal and the highest useful signal. The lowest measurable signal is restricted by the noise level, whereas the highest signal can be defined as the point where the signal cannot be increased anymore even if the irradiance is increasing. This can also be called as *saturation* of the detector when some physical constraint is reached by the detector. (Vincent et al., 2015, p 49)

One should consider the most important properties that are demanded of the camera. This kind of properties can be e.g. cost, fast response time, uniformity or sensitivity. Usually there is no ideal option and so compromises should be made. The response time and the noise levels of tested IR cameras are the main features examined in this thesis work. As already mentioned, the ability of tested IR cameras to detect rapid heat effect was tested. According to the theory, one can now make a hypothesis, that microbolometers will not detect effects as rapid as photon detectors. One can also assume, that the photon detectors will detect smaller temperature differences due to the higher noise level associating with microbolometers.

## 2.3 Previous research

Some previous studies in which different properties of the IR cameras have been examined are introduced in this section. The first one used a rotating plate as a test set-up. This research was prioritized because the rotating plate system was also used as the technical phantom in this thesis work. The other research studied the ability of the IR cameras to detect small temperature variations. This research is presented because it is also an important subject in this thesis.

### 2.3.1 Rotating plate as a test set-up

A rotating plate as a measurement set-up was used in the study of Posch et al. (2009). In their study, a novel temporal contrast IR sensor based on $64 \times 64$ pixel microbolometer was introduced. The autonomous pixels of the sensor independently

responded to changes in incident IR radiation. An upper and lower thresholds had been set for "+" and "-" events, respectively. Whenever the voltage difference of the pixel exceeded or undershot one of these thresholds this created a measured event. So this removed the need to read information of all the pixels whether or not their information had changed, which is the case with classical image sensor. Also the temporal resolution was not limited by the frame rate of the camera. The rotating plate was adjusting the rate of measured heat effects at frequencies 2–220 Hz. Behind the plate there was placed a rectangular heating element that covered about $5 \times 20$ pixel area. The temperature range of the measurement target was 20–330 ℃.

The measurement results showed that the temperature difference between the rotating plate and the heating element had to be really high to create an appropriate number of detected events. When the stimulus frequency was set to 10 Hz, the average of detected events was 80 % with the temperature difference of 300 K. About 50 % of events were detected when the temperature difference was 110 K and no events at all when the temperature difference was reduced under 35 K. The sensitivity dependency of the sensor on the stimulus frequency for different temperature contrast was also tested. According to the results, over 50 % of high contrast events (temperature difference above 135 K) could be detected when stimulus frequency reached 20 Hz. The temperature difference had to be above 275 K, and still only about 20 % of events could be detected when stimulus frequency was 100 Hz and no events when frequency reached 200 Hz.

The reasons for low temperature resolution were the low thermal sensitivity and temperature coefficient of the sensor. Even though the results were not so convincing, one can still see the potential of this event-based IR sensor if it would utilize more sensitive sensor elements.

### 2.3.2 Measurement of small temperature variations

A study by Meola et al. (2015) is one example where the ability of IR cameras to detect small temperature variations was examined. In the study, FLIR's SC6000 QWIP, X6540sc InSb and T440 microbolometer were tested. The cameras measured cyclic thermo-elastic effect caused by the bending of composite material. The relation between noise behaviour and frame rate was also examined. With the QWIP camera there was a noticeable sinusoidal pattern with some frame rates and some random jumps in the output signal. These effects were not found from results of the other cameras. The behaviour of QWIP was explained by the dark current, which is a major source of noise in these types of detectors. The sinusoidal noise

was removed from the signal by frequency analysis and correction with the help of the reference area. The study presented that the InSb camera has a lower noise level than other cameras and the microbolometer has a higher noise level and lower sensitivity. However, the QWIP has a higher sensitivity and with a help of signal correction, the sinusoidal noise and random jumps could be removed from the signal of the camera. So according to the study, the QWIP camera is the best choice for detecting small temperature variations.

However, in study of Meola et al. (2015), created temperature variations were still about 10 times bigger than the NETD values of the cameras. So the temperature differences should be even smaller to be applied in the evaluation of how small temperature differences the camera can detect. Furthermore, to create a controlled temperature variation in the order of tens of millikelvins is challenging.

# 3. MATERIALS AND METHODS

In this chapter, the built test set-up and the evaluated cameras are presented. Calibration and NUC are considered and the main steps of these procedures are demonstrated. Finally, the performed tests are introduced and discussed. The main idea of these tests was to demonstrate how well rapid heat effects and small temperature differences can be detected by different IR camera technologies. The aim is to discuss the limitations that some technologies have and what are the things that should be taken care of when events lasting only milliseconds are detected. The noise levels of every camera are also defined and these values are compared to ones determined by the manufacturers.

A test set-up was planned and built for performing the measurements. The test set-up includes:

- Camera being tested and a tripod
- Technical phantom incl. the plate system, the measurement target, a microcontroller and a servo motor
- Cover for background radiation
- Thermometers to measure the temperatures of the measurement target and the environment
- Computer with Arduino control center, FLIR ResearchIR or Telops RevealIR (former HypIR) software and Matlab for data analysis.

The cameras were tested in different places, so the test set-up was designed so that it was easy to move and rebuild again to a new place.

## 3.1 Technical phantom

Tests were executed using a technical phantom which is presented in Figure 3.1. The phantom contains two plates: a stationary rectangular plate and a rotating

circular plate. The rotating plate contains a sector hole, through where the camera can see the measurement target i.e. a warm object placed behind the plates, and a round hole for an IR led. The distance between the axis of rotation and the sector hole is 120 mm and dimensions of the sector hole are vertically 10 mm and horizontally 2.09–2.27 mm, thus it forms a 1° sector hole. The horizontal size of the sector hole is adjusting the time how long the warm object is visible. This rotating plate with the 1° sector hole was used for rapid heat effect measurements where the temperature difference between the warm object and the environment was about 7 ℃. There was also used another rotating plate, otherwise similar to the first one but with a bigger sector hole, 15°. This plate was used when slower effects with small temperature differences were measured.

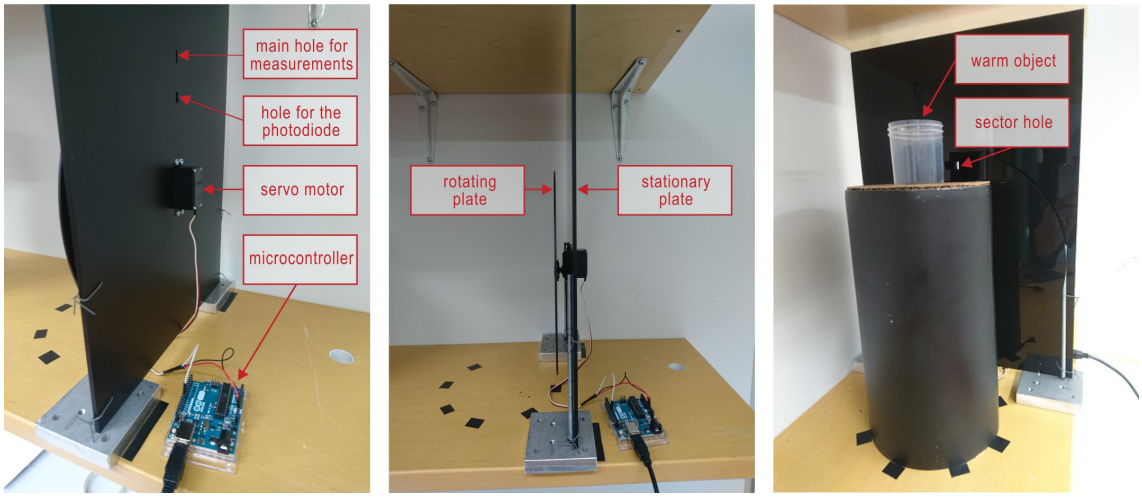


***Figure 3.1*** *Front, side and back of the technical phantom from left to right.*

The rotating plate is attached to a servo motor (Parallax's High Speed Continuous Rotation Servo), which is then connected to a microcontroller (Arduino UNO). The servo motor is also attached to the stationary plate that has a main hole for the measurements and a round hole for a photodiode. The stationary plate is connected to two metal stands. The main hole on the stationary plate is rectangular and its dimensions are vertically 10 mm and horizontally 2.25 mm. The camera is able to see the object only through the hole of the stationary plate, so it is limiting the visibility of the warm object. The plates were cut with a laser cutter and then painted with matt black paint to result approximately 0.96 emissivity of the surface. The value of emissivity can be inspected with FLIR ResearchIR software when the temperature of the object surface is known.

The servo motor rotates the circular plate and the microcontroller is used to control the servo. Rotational speed of the plate can be set by the user with computer via Arduino control center software. So the rate and the duration of the heat effect can

be changed by altering the rotational speed of the plate.

Behind the plates there is a warm object i.e. a small container filled with warm water. Electrical tape was attached to one side of the container to reach emissivity value of 0.96. The distance of the container from the surface of the rotating plate is 6 cm and from the stationary plate 8 cm. The camera is on the other side of the phantom plates and it can see the container through the holes when they are one after another. The center of the camera lens is at the same level with the hole of the stationary plate. The height of the camera was adjusted by using the tripod.

The room temperature was varying between different measurements because the tests for the cameras were performed in different places. So it was important that the temperature of the measurement target was adjustable to ensure the same temperature difference for every measurement. Water with suitable temperature was taken from a tap. Temperature difference between the environment and water was set to approximately 7 ℃ when rapid heat effect tests were performed. The thermometer was placed in the water during the measurements and the precise temperature value was written down for every test case. For small temperature difference tests the temperature difference was reduced after every test and the purpose was to see how small temperature differences the camera can distinguish.

It is important to know how long the object can be seen by the camera. So the rotational speed of the servo motor have to be known. Revolutions per minute (RPM) was measured using a photodiode on one side and an IR led on the other side of the rotating plate. For RPM measurements, holes were made on the plates for the photodiode and the IR led. The microcontroller is reading a signal when the diode is absorbing radiation from the led. According to that information, the RPM value is calculated and showed on the monitor. When the time of one rotation and the size of the sector hole are known, the time how long the camera can see the warm object behind the plates can be calculated.

Before the plate phantom was chosen, there were also consideration of other phantom options. First idea was to build a mechanical system where a warm object would touch at the surface of an appropriate material for a short time. Paper or other thin material layer was considered as a surface material. User could set the temperature of the warm object as well as the time period of the contact. Camera would then be on the other side of the surface, detecting when the object is touching the surface. A residual heat after the contact was faced as a problem. So the surface was not cooling fast enough. Also the conduction of the heat have to be considered with this kind of phantom and it would make it more complex. Because the whole idea of

this measurement was to detect rapid effects, this phantom option was dismissed.

The other possible option was a resistor phantom, where the resistor would represent a controllable heat source. Heating of the resistor would be controlled by changing the power value and time period of the current flow. Again, the heating and cooling time of the resistor was considered as a problem.

## 3.2 Evaluated cameras

During the project, five different cameras were tested. Three cameras used cooled InSb photon detectors and other two were uncooled microbolometers (MB) (Ronda, 2018; Telops, 2015; FLIR (SC7600), 2014; FLIR (A655sc), 2014; FLIR (X6900sc), 2018; FLIR (T1020), 2015). FLIR A655sc microbolometer is owned by Imaqen Ltd and others were borrowed from Aalto University, Infradex Ltd and Tampere University. All except one of the cameras are made by FLIR Systems and one camera is made by Telops. Cameras and their basic specifications are shown in Table 3.1. One should also notice that usually there is a big difference in costs between uncooled microbolometers and cooled photon detectors. Microbolometers used in this work cost around 20 000–40 000 euros, whereas all the InSb cameras cost more than 100 000 euros. More detailed specifications of the cameras are presented in following documents Telops (2015), FLIR (SC7600) (2014), FLIR (A655sc) (2014), FLIR (X6900sc) (2018), and FLIR (T1020) (2015).

***Table 3.1*** *Cameras under tests and their basic specifications.*

| **Cameras** | **Type** | **Resolution (pixels)** | **Spectral range (µm)** | **NETD (mK)** |
|---|---|---|---|---|
| Telops Fast-IR 2K | InSb | 320×256 | 3.0–5.4 | 25 |
| FLIR SC7600 | InSb | 640×512 (320×256) | 1.5–5.1 | <20 |
| FLIR X6900sc | InSb | 640×512 | 3.0–5.0 | <20 |
| FLIR A655sc | VOx MB | 640×480 | 7.5–14.0 | <30 |
| FLIR T1020 | $\alpha$-Si MB | 1024×768 | 7.5–14.0 | <20 |

Depending on the camera and used lens, the FOV is different for every camera. It was decided that the distance between camera and the stationary plate would be determined so that the IFOV of every camera would be the same. This way the spatial resolution is the same for every camera. The IFOV of 0.285 mm was used to calculate the needed distance. The distance for every camera was calculated as

$$Distance = IFOV \cdot N_{pix} \left( 2 \ \tan \frac{FOV_{deg}}{360} \pi \right)^{-1}, \tag{3.1}$$

where $N_{pix}$ is the number of pixels in one dimension. The distance can be calculated by using either horizontal or vertical dimension, as long as the same dimension is used both for pixel number and FOV. One can see the needed values in Table 3.1 (resolution) and Table 3.2 (FOV). The calculated distances are also presented in Table 3.2. The distance is measured from the surface of the stationary plate to the surface of the camera lens.

***Table 3.2*** *Optical parameters of the cameras and calculated distances.*

| Cameras | f-number | FOV (°) | Distance (cm) |
|---|---|---|---|
| Telops Fast-IR 2K | f/2.5 | 21.2×17.3 | 24 |
| FLIR SC7600 | f/3 | 11×8.8 | 95 |
| FLIR X6900sc | f/2.5 | 18.2×14.6 | 57 |
| FLIR A655sc | f/1.0 | 45×33.7 | 22 |
| FLIR T1020 | f/1.15 | 28×21 | 59 |

## 3.3 Calibration

All of the IR cameras are calibrated at the factory. This is performed in a calibration lab, where the camera takes multiple measurements from blackbodies of different temperatures. The temperature, radiation level, emissivity and distance of measured blackbodies are known. According to this information, tables that shows the relation of A/D counts and temperature/radiance values are created. All the measurements with different temperatures are captured into the calibration software and those are passed through radiance curve fit algorithms. As a result, a set of calibration curves are achieved. These calibration curves are then stored into the memory of the camera. When measurements are done by the user, the digital value of the measurement is converted to the temperature value with guidance of the calibration curves. Also the atmospheric attenuation and ambient temperature with its reflection have an effect on the final result and this should be noticed by the user. (*The ultimate IR handbook* 2012, p. 11-12)

The user can also perform the calibration by using a blackbody. At least with FLIR cameras the user can choose between the factory calibration and the user calibration done by him/herself. What is described next is only valid when one uses the FLIR ResearchIR software.

User Calibration Wizard (feature of the software) was tested with FLIR A655sc microbolometer and the main steps of this procedure are described next. A metal container filled with water of different temperatures was used as a blackbody (Figure 3.2). First, the container was filled with water and placed in front of the camera. The user selected the target (in this case the container hole) from the camera frame with a region of interest (ROI) tool. The temperature of the water in the blackbody container was measured with a thermometer and the value was entered to the software. The camera also measured the temperature of the container hole and this value was compared to the entered value. Then the container was filled with water of different temperature and the measurement was repeated. At least two different temperature values should be measured and according to this information the software performs required corrections to provide more accurate results. More precise instructions can be found from *ResearchIR 4 User's Guide* (2016, p. 71-84).

***Figure 3.2*** *The blackbody phantom used to perform a user calibration.*

The user calibration performed did not affect the temperature measurements when comparing measurements done with the factory calibration. One can draw a conclusion that the user calibration was performed right, and the factory calibration was up-to-date. It was decided to use factory calibration when other cameras were tested. However, FLIR SC7600 was measuring scene temperature more than 2 Celsius degrees higher that it actually was. This error could have possibly been avoided with the user calibration. However, there was a limited time to perform the measurements, so the user calibration could not be performed. In this case the purpose

was to examine the temperature differences, thus the precise absolute temperature was not so important. In the future, it would be beneficial to perform the user calibration in situations where it has been a long time since the last factory calibration.

In addition to a proper calibration, one should be aware that the NUC is done for the camera before starting the measurement. This is crucial because the gain and zero offset of every individual sensing elements of the FPA are slightly different. It is very important to correct these differences to the normalized values to create a functional FPA. The NUC is performed before every measurement with the help of ResearchIR software. User can select if only a one-point correction is performed, which corrects the pixel offset. The other option is to do a two-point correction, which corrects also the gain differences in addition to the offset. Usually, the NUC process also identifies so called bad pixels of the FPA and replaces those with the average value of nearest neighbour pixels. These bad pixels are faults of the FPA resulted from semiconductor wafer processing and produce no output signal or a signal that is far outside of the correct range. (*The ultimate IR handbook* 2012, p. 17)

The NUC can be performed on camera- or PC-side. If the user decides to perform a PC-side NUC, this is done with the PC-side correction of the ResearchIR software. The user needs two uniform plates with different temperatures. First, the user will select whether a one-point or a two-point correction is done. Then the number of frames from which the average is taken is decided. (*ResearchIR 4 User's Guide* 2016, p. 83) According to the technical sales specialist of Infradex, Topi Kaaresoja (2018), the number of frames should be set at least to 32 to acquire enough data for average. After this, the first uniform plate is placed in front of the camera. To prevent reflections, the plate should be slightly at an angle compared to the lens of the camera. The set of frames is recorded by the camera and the same is also done with the other plate. Then the software performs the required corrections and tells the percentage of bad pixels that has been detected and the user can either accept this or discard the result and try again. When using the PC-side correction one should turn off the AutoNUC, which means that the camera is not performing the camera-side NUC by itself and so overwriting the performed PC-side NUC. (*ResearchIR 4 User's Guide* 2016; Kaaresoja, 2018)

One can also choose the camera-side NUC. The camera performs the NUC by placing the uniform scene in front of the detector inside the camera. In general, it is unimportant if the NUC is done on PC- or camera-side, as long as it is done. However in *ResearchIR 4 User's Guide* (2016) it is recommended, that the user should not use the PC-side NUC if the factory calibration is used.

Afterwards it was found out that there were some errors in the NUC file of FLIR X6900sc camera. Therefore, the scene appeared non-uniform on the edge of the scene. Fortunately, the ROI was only a small area in the middle of the scene, so the non-uniformity was not affecting the measurements.

In case of Telops camera, the calibration is performed with a help of so-called calibration blocks that contain the calibration data necessary to process a raw data. In the performed measurements, the factory calibration blocks were used, but one could also create new blocks by him/herself. Raw data of the camera is processed with the calibration block. In Telops cameras there are different calibration modes i.e. formats for the output data. Radiometric Temperature (RT) format was used in measurements of this thesis work. The RT performs NUC by using the information of calibration blocks to correct the gain and the offset values on pixel by pixel basis. The RT also expresses the results in units of temperature. More information about the calibration blocks and output data formats can be found from *HypIR manual* (2017).

## 3.4 Camera tests

Two different test procedures were performed for each camera during the camera tests. The aim was to study how rapid effects and small temperature differences they can detect. First, in Subsection 3.4.1 the rapid heat effect test is presented. After that, in Subsection 3.4.2 the idea of measuring small temperature differences is discussed. The determination of the noise levels was also an important part of the camera evaluation. The temporal and the spatial NETD values and how they were determined in this work are discussed in Subsection 3.4.3.

The cameras were tested in different places and so environmental conditions e.g. the room temperature was varying. The water temperature was adjusted according to the room temperature so that the temperature difference would be the same for each camera although the room temperature was changing. The test set-up was covered to reduce background radiation.

### 3.4.1 Rapid heat effect

The first test was executed to study how fast heat effects the cameras are able to detect. In this test, the rotating plate with the 1° sector hole was used. The microcontroller was set to rotate the servo motor with six different rotational speeds. The rotational values are shown in Table 3.3. The values were entered to the

software beginning from the slowest one. Ten second measurement time was used for all rotational speeds. In this work, Parallax's High Speed Continuous Rotation Servo was used, so presented values are only valid with this servo motor.

The camera can see the object as long as the holes of the plates are at least partly overlapping. An individual pixel can see the object half of this time. So all the pixels in the hole area are seeing the object the same period of time but not exactly at the same moment, except when the holes are aligned. Also these time values are presented in Table 3.3.

***Table 3.3*** *Rotational values of the rotating plate with the* 1° *sector hole.*

| **Microcontroller value** | **RPM (1/min)** | **Lap time (s)** | **Object seen by camera (ms)** | **Object seen by pixel (ms)** |
|---|---|---|---|---|
| 1 | 19.5 | 3.07 | 17.1 | 8.5 |
| 2 | 55.2 | 1.09 | 6.0 | 3.0 |
| 3 | 84.1 | 0.71 | 4.0 | 2.0 |
| 4 | 103.0 | 0.58 | 3.2 | 1.6 |
| 5 | 113.5 | 0.53 | 2.9 | 1.5 |
| 6 | 123.5 | 0.49 | 2.7 | 1.3 |

As explained in Section 2.2, the technologies of photon detectors and microbolometers are very different. Like one can remember, the integration time of photon detectors, in this case InSb cameras, determines the time that the "shutter" is open and so the pixel collects photons. With FLIR cameras the integration time is defined by the set temperature range, while with Telops the user is able to set the integration time. Different integration times were tested to see how long integration time can be used still avoiding saturation. One can see the used integration times in Table 3.4.

***Table 3.4*** *Camera specifications for the rapid heat effect tests.*

| **Cameras** | **Frame rate (Hz)** | **Integration time/ Thermal time constant (ms)** |
|---|---|---|
| Telops Fast-IR 2K | 300 | 0.3 |
| FLIR SC7600 | 300 | 1.328 |
| FLIR X6900sc | 300 | 0.338 |
| FLIR A655sc | 50 | <8 |
| FLIR T1020 | 30 | <10 |

Because the frame rate and rotation of the plate were not synchronized, the frame rate had to be increased to 300 Hz to be sure that at least a part of the object was seen. Because of the high frame rate of InSb cameras, the measured data was first saved to the memory of the camera and only after the measurement the data could be transferred to the computer. Otherwise frames would be dropped due to the slow data transfer between the camera and computer. With SC7600 InSb camera there was no possibility to use camera memory for recording. Therefore, the resolution of the camera had to be reduced using windowing when the frame rate was increased over 100 Hz. The reduced resolution of SC7600 InSb was $320 \times 256$ pixels.

With microbolometers the situation is different. There is no shutter and so the pixels are constantly collecting incident radiation energy. In this case the problem is the opposite to the photon detectors. The camera should see the object long enough for the pixel temperature to reach the temperature of the object. This time should be at least the thermal time constant of the microbolometer times five (FLIR, 2016). So for A655sc camera it would be 40 ms and for T1020 50 ms. With microbolometers the maximum frame rate is usually around 50 Hz. This is because these cameras are not suitable for applications involving faster effects. The maximum frame rates for both microbolometers were used. The frame rate and the thermal time constant values of the microbolometers are shown in Table 3.4.

Because the room temperature was altering when different cameras were tested, the temperature of the water was changed accordingly. The difference between room temperature and water temperature was adjusted to be around 7 ℃. Table 3.5 shows the temperature values used during the tests.

***Table 3.5*** *Room and object temperature values in the camera tests.*

| **Cameras** | **Room temperature (℃)** | **Water temperature (℃)** | **Temperature difference (℃)** |
|---|---|---|---|
| Telops Fast-IR 2K | 23.6 | 30.6–30.7 | 7.0–7.1 |
| FLIR SC7600 | 23.5 | 30.4–30.7 | 6.9–7.2 |
| FLIR X6900sc | 22.5 | 28.7–29.2 | 6.2–6.7 |
| FLIR A655sc | 24.5 | 31.6–31.7 | 7.1–7.2 |
| FLIR T1020 | 22.2 | 28.7–29.3 | 6.5–7.1 |

According to the theory of different detectors, the hypothesis of the test results can be made. One can assume that with the InSb cameras the effect lasting only a couple of milliseconds can be detected due to the fast integration time. With the microbolometers the opposite assumption can be made and most likely the effect

will be detected poorly. Because the used temperature difference is quite high, one can still probably detect the time instant of the effect, but not the real temperature of the object.

## Analysis in Matlab

In Matlab (*Matlab documentation* 2019) a ROI was selected from the scene so that only pixels that saw the object i.e. the pixels in hole area were selected. Only pixels inside the ROI were taken into account and other pixels were removed. The pixels with the maximum and the minimum temperature values in the ROI area were chosen from every frame and plotted as a function of time.

Because of the short integration time of the InSb cameras, the motion of the target is frozen when the frame is captured, and one can easily detect which pixels see the object. The warm object was seen only partly in some frames. In these cases it would be inappropriate to take all pixels in ROI area into account. In this way there would have been also pixels that are not detecting the object, but the surface of the rotating plate instead. So in frames where the object was seen, only the pixels that exceeded a predefined threshold temperature value were chosen. It was assumed that the object is seen if the temperature value of one pixel exceeds the minimum temperature value of the ROI by one Celsius degree. In this way also the pixels around the hole were ignored. Figure 3.3 illustrates how the ROI area was selected (left figure) and which pixels exceeded the threshold temperature value (right figure).

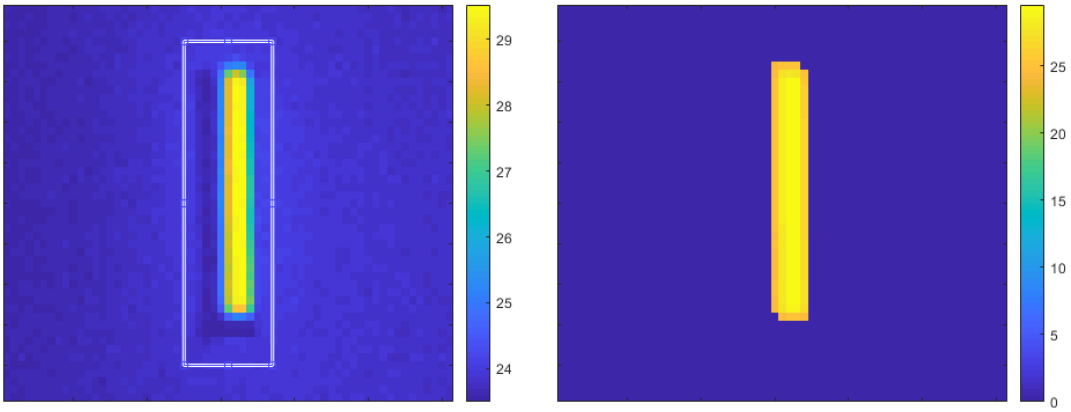


***Figure 3.3*** *The left side figure illustrates how the ROI is selected from the frame. The right side figure shows which pixels of the frame exceed the predefined threshold temperature value. Example frames are captured with an InSb camera.*

Due to the slow response time of the microbolometers the motion of the target is not

frozen. Thus one cannot detect from the frame which pixels are seeing the object and so are still warming up or already cooling down. Predefined threshold value could not be used with the microbolometers to detect which pixels see the object and which do not. So with microbolometers, the entire hole area was carefully cropped, thus no pixels around the hole were selected. All pixels in that area were considered.

After selecting the pixels of the ROI, an average temperature of the pixels was calculated for every frame. A median of all ROI pixels, which was considered as the temperature of the plate system i.e. the environment, was subtracted from the average temperature values to get the temperature difference between the object and the environment. Finally, the average temperature differences were divided by the measured temperature difference given by the thermometers to get relative temperature difference measured by the camera. This was done because the temperature of the water was varying during the measurements. These values were reported as percentage values and plotted as a function of the measurement time. From the plot one should recognize the time instant when the object was seen by the camera, in other words, see the peaks in the plot.

Detection abilities of the cameras were compared with each other. The peaks of the average temperature plot were located, and the average of the peaks was calculated. This was done for the plots of all rotational speeds. Finally, the average of temperature peaks was plotted as a function of time the object was visible. The same was done for all cameras and then plotted to the same graph. Thus one can compare the detection ability of the cameras.

### 3.4.2 Small temperature differences

The aim of the other test was to solve how small temperature differences the cameras can reliably measure. The temperature of the object was set close to the room temperature by adjusting the temperature of water in the container. The temperature difference between water and environment was decreased until the water temperature was the same as the room temperature.

In this test, the plate with the bigger sector hole (15°) was used to increase the time that the object is visible. Rotational speed of 19.5 rpm was used for every measurement. With this rotational speed, the object was visible for 255.8 ms. A ten second measurement time was used for every camera.

Because the time the object is visible was longer in this test, 50 Hz frame rate could

be used for every camera, except for T1020 that has the maximum frame rate of 30 Hz. The integration times and the thermal time constant values of the cameras were the same as in the rapid heat effect test, except with Telops that had an integration time of 0.4 ms.

When the data of these measurements was analyzed, it was noticed that the results were inconsistent. For example, even if the temperature difference was decreased according to the thermometers, the camera measured a larger temperature difference between the object and the environment. This is due to the fact that the surface temperature of the plates was not the same as the measured environment temperature. This is because e.g. the servo motor and the water container were possibly heating the plates. Also a thermal radiation from the camera itself reflects from the surface of the stationary plate, thus increasing the measured temperature of the plate. Also the thermometers used were not accurate enough. The real temperatures of the plates could not be measured. Because of many sources of error, the results of this test are not presented in this work.

One can come to a conclusion that this kind of phantom is not suitable for accurate small temperature measurements. At least if there are not extremely accurate thermometers and an adjustable heat source used. So in the future, the measurement system for small temperature difference tests should be improved. However, as mentioned in Subsection 2.3.2, it is challenging to create a controlled temperature differences in the order of tens of millikelvins.

### 3.4.3 Noise characterisation

One fundamental property of every IR camera is the noise. Like told in Subsection 2.2.5, every detector type has their own noise sources and levels. The NETD value of the camera describes the temperature difference in the scene that creates the SNR equal to 1. The NETD will vary depending on the camera settings and environmental conditions, as already told in Subsection 2.2.6. The temporal NETD values of the cameras provided by the manufacturer are shown in Table 3.1. One should notice, that these values are measured in laboratory conditions and thus they differ from the conditions during the measurements of this thesis work. The temporal and the spatial NETD values were calculated for the tested cameras. As the test conditions were similar and the same calculation procedures were used with every camera, these values are comparable.

To calculate the temporal NETD value, a ROI of $100 \times 100$ pixels was selected from the frame. The ROI was selected so that it contained only pixels that saw

a smooth area of the stationary plate. The calculation was done in the same way as described by Danjoux (2019) for uncooled bolometers to obtain as comparable results as possible. The calculation procedure was introduced in Subsection 2.2.6. The only difference was that FLIR takes all pixels in the frame into account, whereas in this work only $100 \times 100$ pixels were selected. This has practically no effect on the result as the standard deviation was calculated as a function of time. A histogram was used to present the standard deviation values of all pixels in the ROI area. The median of all standard deviation values is the temporal NETD of the camera.

Also the spatial NETD was calculated for the cameras. There were some minor temperature variations caused by external sources. Temperature variations in the frames was also produced by the error in the NUC file of InSb X6900sc camera. These static and low frequency heat variations of the frames were removed before calculating the spatial NETD. The function for correcting temperature variations was produced together with co-worker Heimo Ihalainen. First, the frames containing the warm object were removed. The median of each pixel was subtracted to get rid of the static temperature variation of the frame. 2D orthogonal polynomials were used to find low frequency temperature variations. Polynomials are acting better on the edges of the frame than sine waves that are commonly used to detect frequency components of the signal in Fourier analysis in signal processing. (O'Leary and Harker, 2011) More about orthogonal polynomials and how they are used in 2D data modelling can be found in documents and toolbox of O'Leary and Harker (2013). One function (dop.m) of the Matlab toolbox of O'Leary and Harker (2014) was used to generate the set of orthogonal polynomials used to locate the low frequency heat variation in the frames. Located temperature variations were subtracted from each of the frames. Now only the characteristic noise of the IR camera was left over. The spatial NETD was then calculated the same way than by Danjoux (2019), as described in Subsection 2.2.6. Again, the histogram was plotted to present the standard deviation values of $5 \times 5$ pixel regions of the average frame. The median of all standard deviation values is the spatial NETD of the camera.

The total NETD was also calculated according to Equation 2.46. One should remember that the NETD value provided in the specification sheet of a camera is the temporal NETD, not the total NETD. The total NETD values were calculated in this work as they can be compared to each other. One can expect according to the theory, that the noise levels of the microbolometers are higher compared to the InSb cameras.

# 4. RESULTS AND DISCUSSION

In this chapter, the results of the rapid heat effect tests, as well as the determined noise levels of the cameras are presented and discussed. First, the results of every camera are presented separately in Section 4.1. By combining these to the theory introduced earlier, one can make some conclusions about the functionalities of the cameras. After this, a comparison of different camera results is made. In addition to the test results, noise levels associating with the cameras are presented in Section 4.2. The calculated noise levels of the cameras are compared to one another and also to the values provided by the manufacturers.

Like discussed in Subsection 3.4.1, the results are assumed to be favourable for the InSb cameras, whereas expectations for the microbolometers are not so high. What comes to NETD values, at least manufacturer values are promising for all the cameras as one can notice in Table 3.1.

## 4.1 Rapid heat effect

Results of the rapid heat effect tests with different rotational speeds are shown in Figures 4.1– 4.3 and 4.5– 4.6. In these cases the object was visible for 17.1, 4.0 and 2.7 ms for the camera and half of these times for each individual pixel. The rotational speed increases from the topmost to the lowest figures and so the time the object was visible decreases. In the graphs on the left side, one can see the temperature difference measured by the camera in relation to the real temperature difference between the object and the environment measured by the thermometers. From here onwards, when the average temperature peaks are mentioned it means the peaks in these graphs. On the right side one can see the maximum and the minimum temperature values in the ROI area as a function of measurement time.

First, the results of Telops Fast-IR 2K InSb camera are presented in Figure 4.1. From the results one can see that Telops can detect rapid effects accurately. The maximum temperature peaks are corresponding to the thermometer values quite well, at least with slower rotational speeds. With a rotational speed of 123.5 rpm i.e. when the object was visible for 2.7 ms, the height of the temperature peaks

varies a lot, both in the average and the maximum graphs. The rotation of the plate and the frame rate were not synchronized and thus depending on the time instant the frame is captured in some rounds, the camera can detect only a very small area of the object. So it is possible that with unfortunate timing, no pixel can see the object for the entire integration time but will also see the surface of the rotating plate. This could be improved by increasing the frame rate.

According to the *Nyquist-Shannon sampling theorem*, the sampling rate (in this case the frame rate) of the system has to be at least twice the highest frequency component of the detected signal. So the minimum sampling rate can be defined as

$$F_s = 2f_{max}, \tag{4.1}$$

where $F_s$ is the *Nyquist rate* when $f_{max}$ is the highest frequency component of the signal i.e. the *Nyquist frequency*. If one is using a lower sampling rate, aliasing is happening, in other words, signal frequency components that are higher than $f_{max}$ are summed to lower frequency components. (Balch, 2003)

One can now reach a conclusion that used the frame rate was too low for the measurements. Therefore, the height of the peaks varies a lot. In Table 4.1, one can see the frequencies of the effect and the required frame rates i.e. the Nyquist rates that should have been used. One can now realize, that frame rate of the InSb cameras (300 Hz) was suitable only for the first case when the object was visible for 17.1 ms. For other rotational speeds, higher frame rate should have been used. For Telops this is not a problem since the frame rate can be increased up to 2000 Hz with a full resolution (Telops, 2015).

***Table 4.1*** *The Nyquist rate for the different effect frequencies.*

| **Object seen by camera (ms)** | **Frequency of effect (Hz)** | **Nyquist rate (Hz)** |
|---|---|---|
| 17.1 | 58.6 | 118 |
| 6.0 | 165.7 | 332 |
| 4.0 | 252.4 | 505 |
| 3.2 | 308.9 | 618 |
| 2.9 | 340.5 | 682 |
| 2.7 | 370.4 | 741 |

One can detect from the average graphs in Figure 4.1, that the highest peaks in

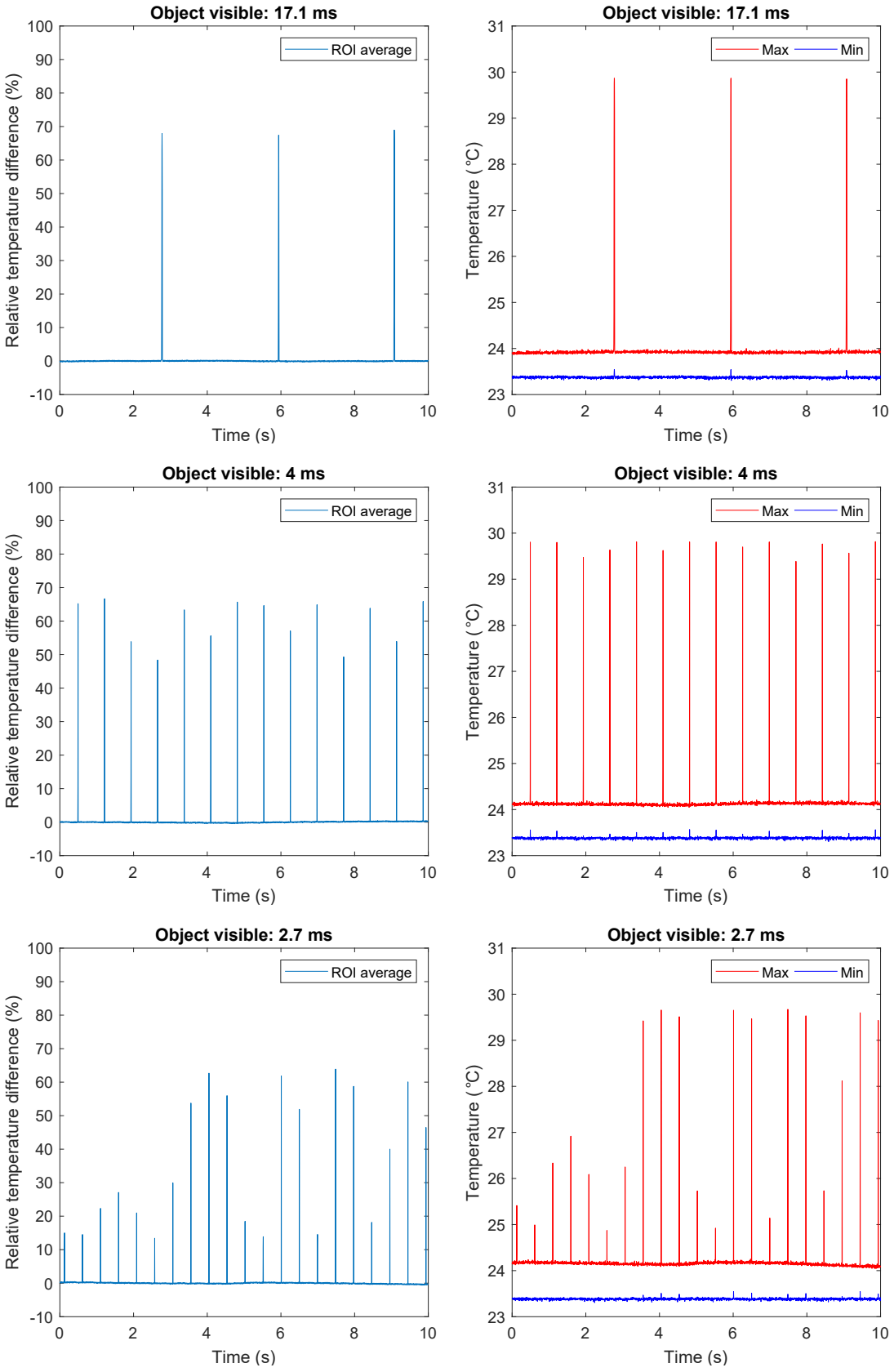


***Figure 4.1*** *Rapid heat effect test results of Telops Fast-IR 2K camera. The left side graphs show the average temperature of the ROI compared to the temperature measured by the thermometer. The right side graphs present the maximum and the minimum temperature values in the ROI.*

all test cases reach the level of 65–70 % of the object temperature. From this can be concluded that the ability of Telops to detect rapid heat effects is good as long as the frame rate is increased to an appropriate value. The same conclusion can be made on grounds of the highest peaks in the maximum graphs.

Visibility of the object could have changed during the integration time. Because of that, some pixels saw the object only for a part of the integration time. This would reduce the detected temperature values of the pixels and thus affect the average and the maximum temperature values.

The results of FLIR SC7600 InSb camera, presented in Figure 4.2 differ from the results of other InSb cameras. The temperature of the object was not seen as high as it should have been. This can be detected from the average temperature peaks that are not reaching even 50 % of the real temperature difference. Also the maximum temperature peaks are lower compared to the other InSb cameras. The fact that the integration time of SC7600 is 1 ms longer than the integration time of other InSb cameras can explain this. Because of the longer integration time, the object was not likely visible for the entire integration time and thus the measured temperature reduced. However, the integration time is not an explanation with the slowest rotational speed (top graphs in Figure 4.2) because the effect was captured by multiple frames.

The aliasing effect can also be detected in results of SC7600 due to the low frame rate. However, the frame rate cannot be increased with this camera as easily as with Telops. For SC7600 camera, the resolution has to be reduced in order to increase the frame rate to 300 Hz. To increase the frame rate over the 741 Hz, which is the Nyquist rate for the fastest effect, the resolution should have been reduced to $160 \times 128$ pixels (*FLIR Product catalog 2018* 2018). This would have not been a problem in this test, because the detected area is smaller than that. But in many situations, this large reduction of the resolution will cause issues as it is done by cropping the image.

From the base temperature levels i.e. the minimum temperature graphs in Figures 4.1– 4.3 and 4.5– 4.6 one can notice that the other cameras detect the environment temperature within $\pm$ 0.5 ℃ as it is measured by the thermometer. The only exception is SC7600 camera that detects the surface temperature more than 2 Celsius degrees higher than it is measured. That could probably be avoided with calibration. In this test the interest is the temperature difference, thus the error should not affect the results. One should just keep this error in mind when considering the maximum and the minimum graphs in Figure 4.2.

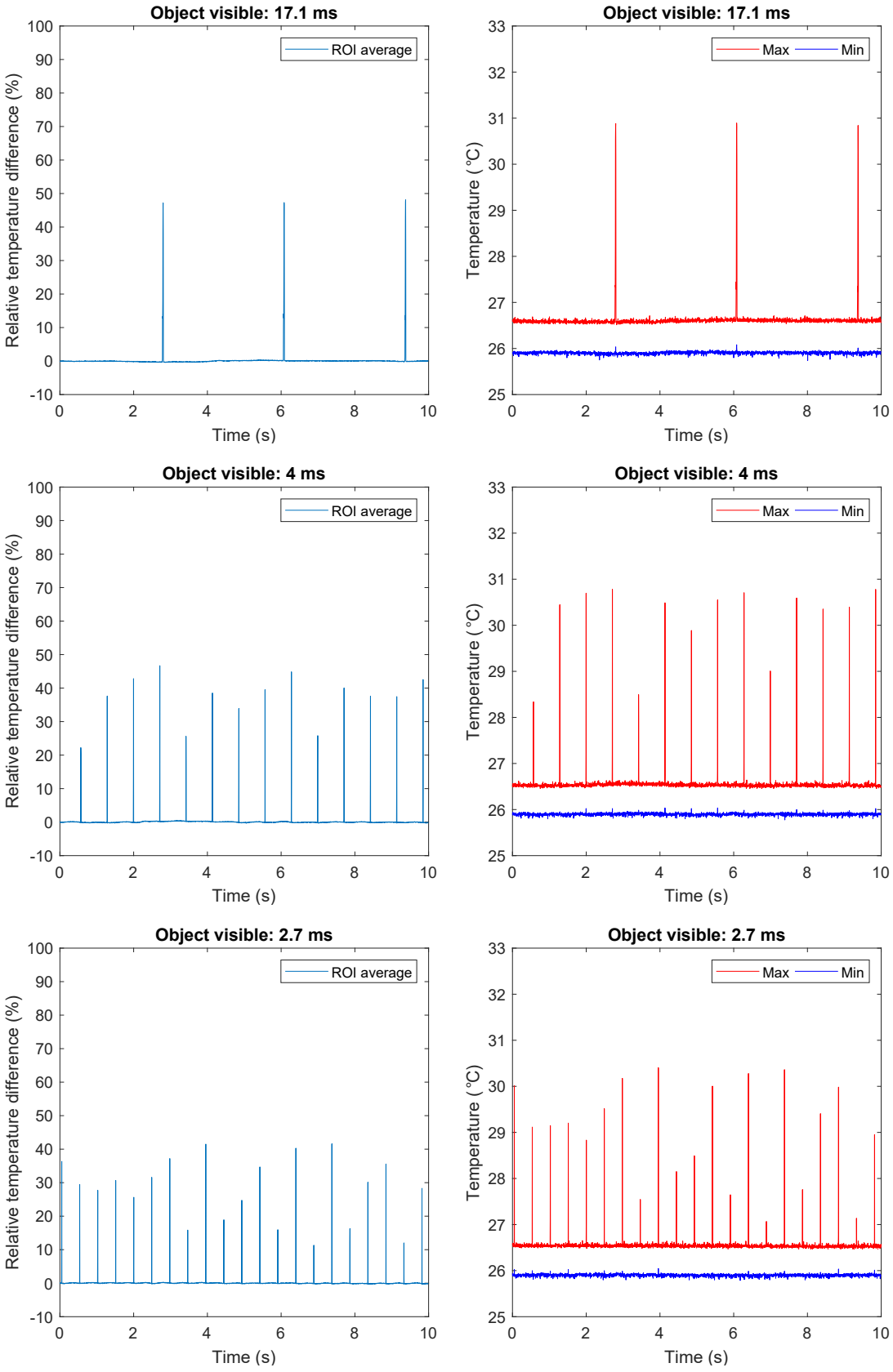


***Figure 4.2*** *Rapid heat effect test results of FLIR SC7600 camera. The left side graphs show the average temperature of the ROI compared to the temperature measured by the thermometer. The right side graphs present the maximum and the minimum temperature values in the ROI.*

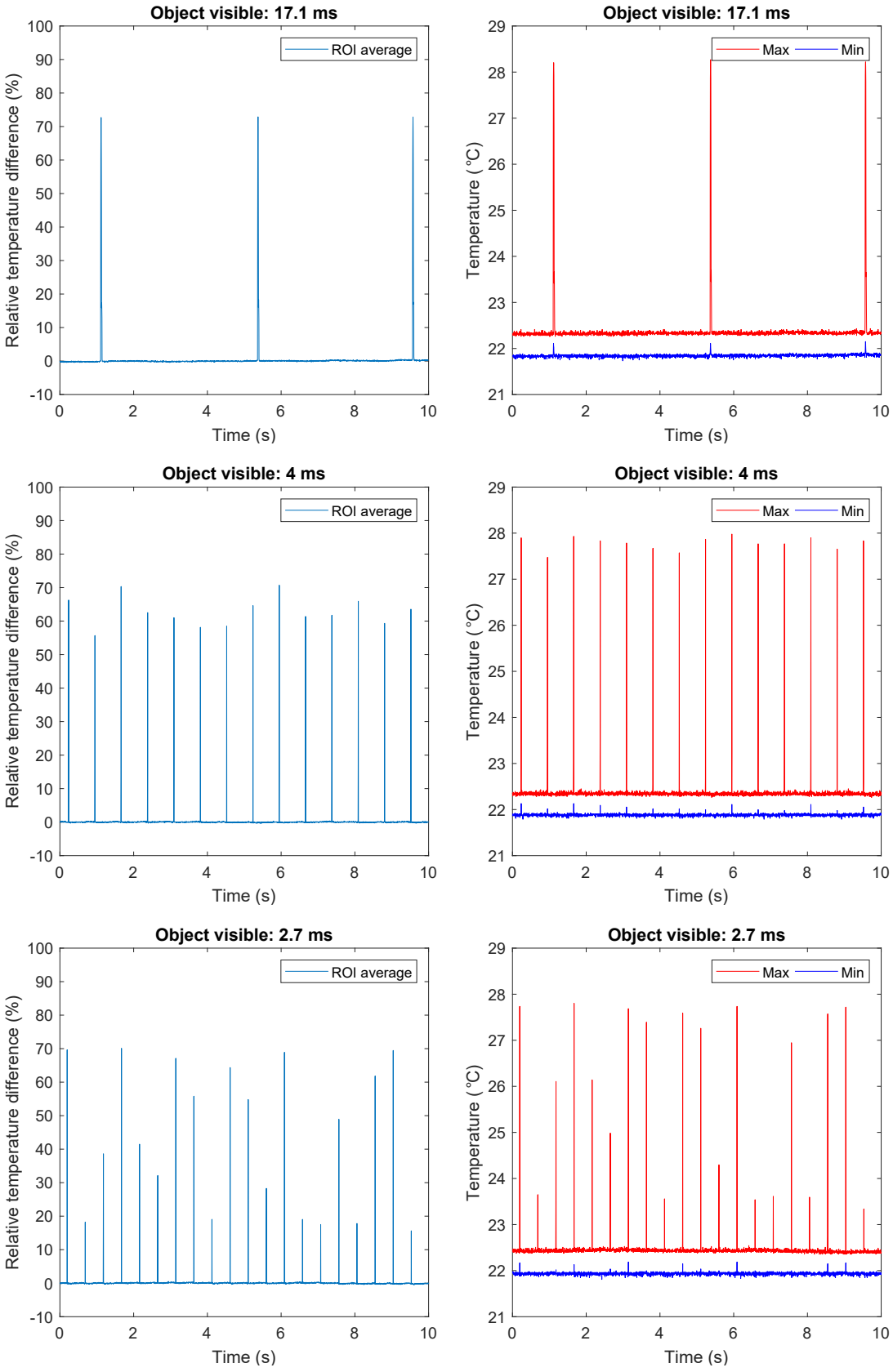


***Figure 4.3*** *Rapid heat effect test results of FLIR X6900sc camera. The left side graphs show the average temperature of the ROI compared to the temperature measured by the thermometer. The right side graphs present the maximum and the minimum temperature values in the ROI.*

The first rotational speed was mistakenly entered wrong to Arduino control center software during the test of FLIR X6900sc InSb camera and thus the plate was rotating a little slower than it should have. Due to the longer lap time, the time the object was visible increased. One can assume that because of the time of exposure with the real rotational speed was already long compared to the frame rate, the error should not affect the results.

The results of X6900sc can be seen in Figure 4.3 and they are quite similar to the results of Telops. The highest average temperature peaks reach at least 70 % and the maximum temperature peaks are less than 1 ℃ apart from the real water temperature. What comes to the aliasing problem, the frame rate of X6900sc can be increased up to 1004 Hz still maintaining the full resolution (FLIR (X6900sc), 2018). So aliasing effect could be avoided with this camera.

According to the results one can make a conclusion that with the InSb cameras the frame rate has to be high enough to detect rapid heat effects. Another possibility is to increase the integration time in which case the quick effect could be seen even with a lower frame rate. However, in this case the camera will probably also see the surface of the rotating plate and thus the measured temperature will be lower than the actual temperature of the object. Integration time of Telops was raised as high as possible without saturation of pixels. With other InSb cameras the integration time was automatically defined by FLIR ResearchIR software according to the temperature range used.

In Figure 4.4, one can see how the InSb camera detected only a part of the object or the whole object depending on the time instant when the frame was recorded. One can also notice how the observed size of the object (i.e. how many pixels saw the object) affected to the height of the average temperature peaks in Figures 4.1– 4.3. There was also a reflection detected in some frames like one can see in Figure 4.4(b). Pixels that saw the reflection were unfortunately reducing the calculated average temperature. The example frames shown were recorded with X6900sc InSb camera when the object was visible for 2.7 ms. The same effects can be detected with other InSb cameras too.

There is a huge difference between the results of the microbolometers and the InSb cameras, as expected. With microbolometers, the thermal time constant and so the response time is much longer compared to the time the object was visible, at least with the faster rotational speeds. So if the effect lasts only a couple of milliseconds, there is no chance for the microbolometer to measure the right temperature of the object. There is simply not enough time for the temperature of the pixel to reach the

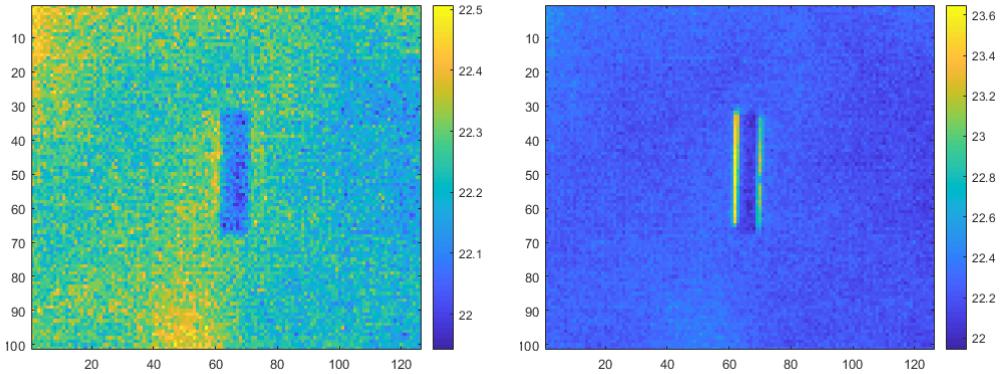

(a) No peak.



(b) Low peak.

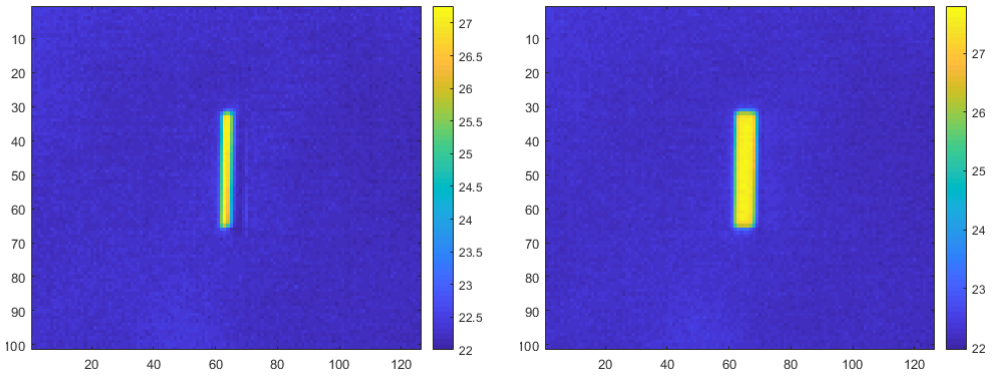

(c) Middle peak.

(d) High peak.

***Figure 4.4*** *Example frames showing how the object was seen in the image of an InSb camera in different cases. Label of the figure tells height of the average temperature peak when the object was visible for 2.7 ms.*

temperature of the object. Also, cooling of the pixel after the object is not visible anymore is slow according to the thermal time constant. At the time the pixel is read, the temperature value is incorrect and much lower than the temperature of the object.

The results of FLIR A655sc camera (Figure 4.5) are slightly better than the results of FLIR T1020 camera (Figure 4.6). This can be caused by the smaller thermal time constant of A655sc microbolometer. Again, the time instant the frame was captured with respect to the rotation of the plate could be the biggest reason.

One can wonder why the average temperature peaks of the upper graph in Figures 4.5– 4.6 are not higher, even though the object was visible for 8.5 ms for each individual pixel. The thermal time constants of A655sc and T1020 are 8 ms and 10 ms, respectively, so one could assume that the temperature of the pixels would increase over 60 % with A655sc and about 50 % with T1020 according to Figure 2.6. But the frame was recorded at intervals of 20 ms (A655sc) or 33 ms (T1020). So at

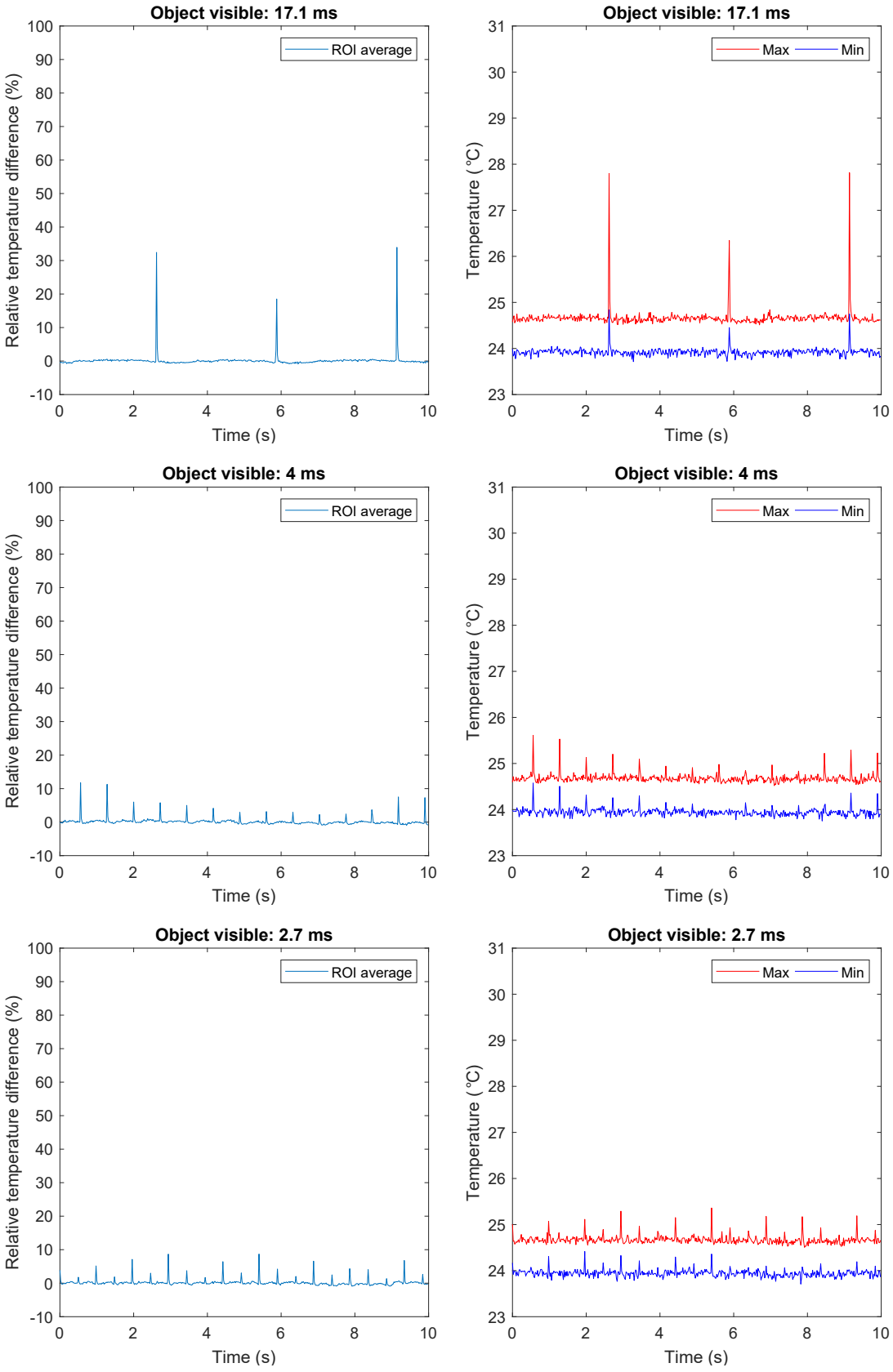


***Figure 4.5*** *Rapid heat effect test results of FLIR A655sc camera. The left side graphs show the average temperature of the ROI compared to the temperature measured by the thermometer. The right side graphs present the maximum and the minimum temperature values in the ROI.*

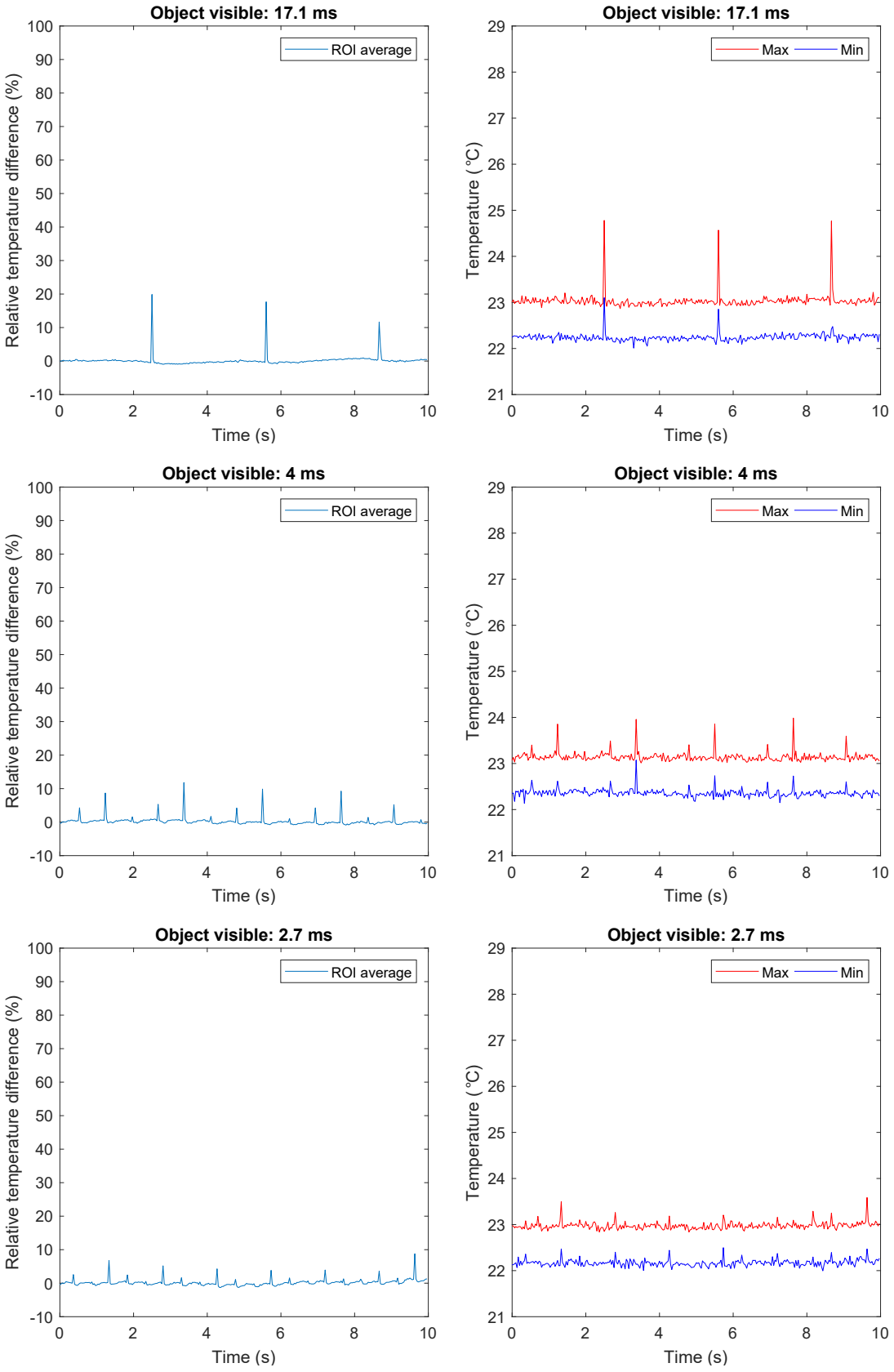


***Figure 4.6*** *Rapid heat effect test results of FLIR T1020 camera. The left side graphs show the average temperature of the ROI compared to the temperature measured by the thermometer. The right side graphs present the maximum and the minimum temperature values in the ROI.*

the time the temperature value of the pixel was read, the value was probably not the highest possible. The frame could be captured when the pixel was still warming up or already cooling down. If the frame rate of the microbolometer could be increased to Nyquist rate, one would be able to measure the maximum temperature value of the pixel. Still, that would not be the right temperature of the object.

It is hard to distinguish the peaks of the average temperature plots of microbolometers when the object was visible for only 2.7 ms. That is why those average temperature plots are presented with a smaller temperature scale in Figure 4.7. One can notice that in the graph of T1020 (lower figure) some peaks are hardly recognizable; one can just conclude that there should be one. Also the base level of the graph is not smooth. The base level of both graphs is changing periodically among the rotation. This is probably because the pixels reacted slowly to the rapidly changing temperature of the scene. The base level of T1020 graph is also varying non-periodically as a function of time. One can assume that this is because of the temperature variation of the environment. However, the test set-up was carefully covered so the variation can be caused by the camera itself.

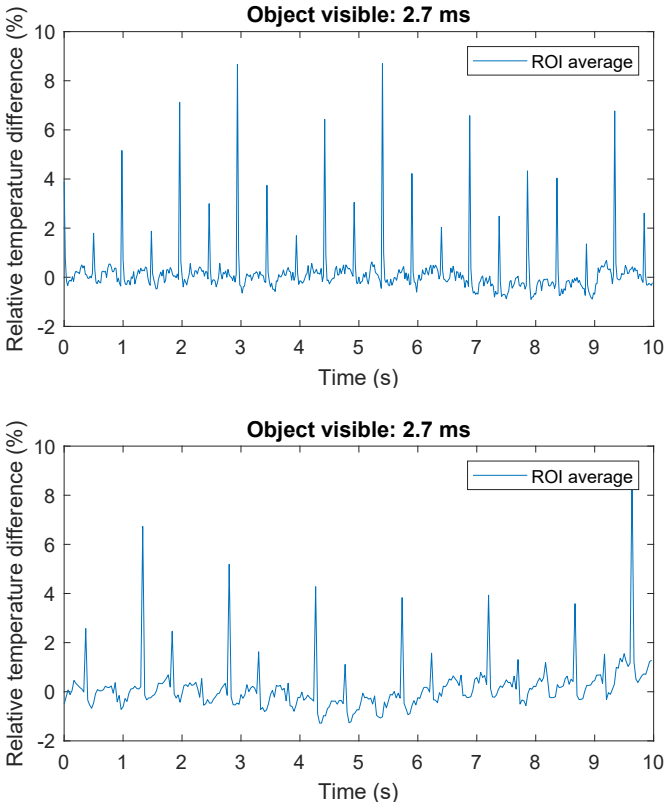


***Figure 4.7*** *Zoomed average temperature plots when object was visible for only 2.7 ms. The upper graph is the result of A655sc microbolometer and the lower one result of T1020 microbolometer.*

In Figure 4.8, one can see which kind of frames caused a certain height of the average temperature peak in Figures 4.5– 4.6 when the object was visible for 2.7 ms. The exact area of the object cannot be detected as opposed to the frames of the InSb cameras. Example frames were recorded with A655sc microbolometer but T1020 microbolometer acts the same.

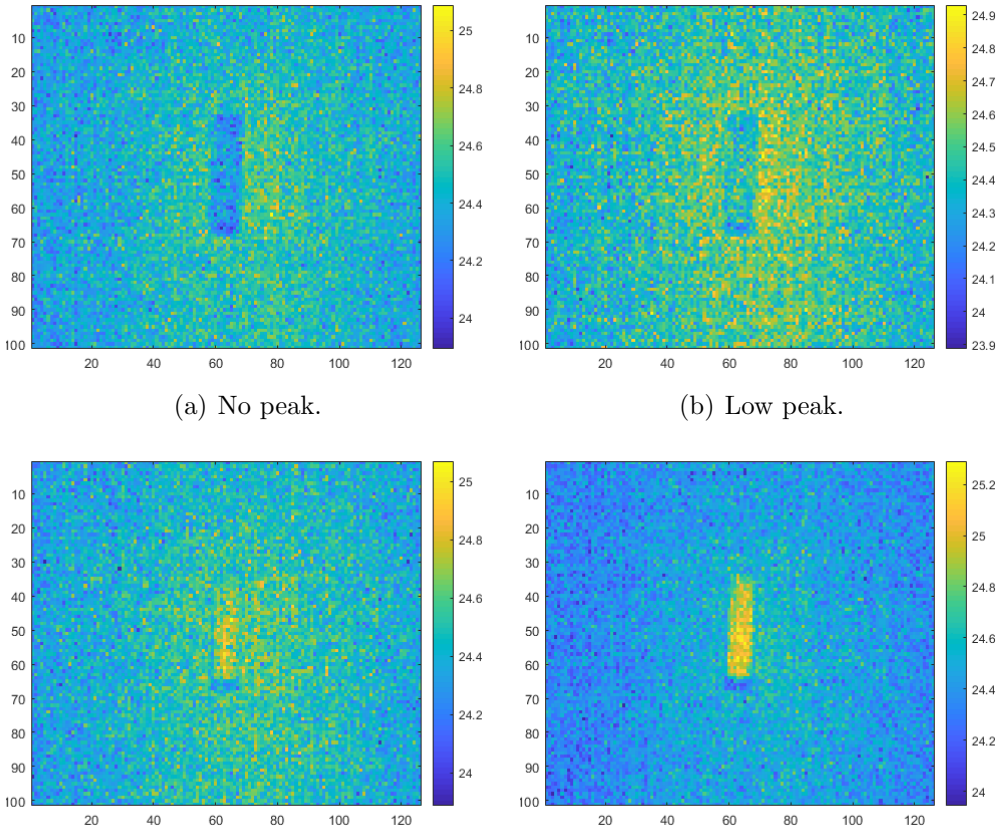

(a) No peak. (b) Low peak.

(c) Middle peak. (d) High peak.

***Figure 4.8*** *Example frames showing how the object was seen in the image of a microbolometer camera in different cases. Label of the figure tells the height of the average temperature peak when the object was visible for 2.7 ms.*

In all Figures 4.1– 4.3 and 4.5– 4.6 the temperature difference between the maximum and the minimum pixel values varies between 0.5–1 ℃ when the object was not visible. In Figures 4.4(a) and 4.8(a), one can also see that there is a temperature difference between the front stationary plate and the rotating plate. Both observations can be assumed to be caused by reflected thermal radiation coming from the camera itself, thus causing the temperature difference between the plates.

In Figure 4.9, one can see the detection ability comparison between different cameras. The relative temperature difference between the object and the environment are plotted as a function of the time the object was visible. The results of Telops and X6900sc are quite similar as already noticed when the results were considered

separately. The relative temperature difference shown by X6900sc is slightly higher. However, one cannot draw definite conclusions from this. The reason for the difference can also be for example that X6900sc just happened to see a bigger part of the object more often. The figure also demonstrates the lower ability of SC7600 to detect temperature differences. This can be explained by the longer integration time of the camera. However, one can reliably compare only the results of the slowest rotational speed (the rightmost measurement point on the graph) as the frame rate was too low for all the other rotational speeds.

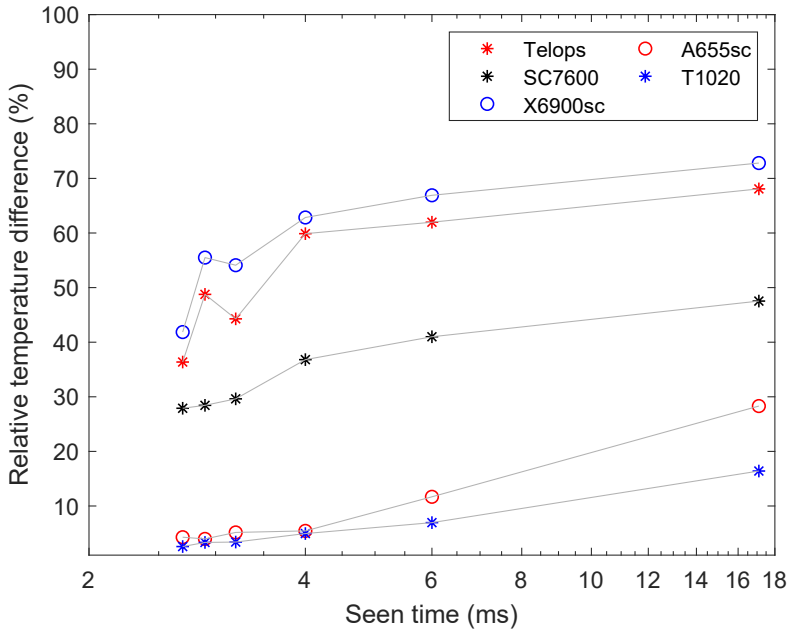


***Figure 4.9*** *Detection ability of the cameras as a function of the time the object was visible.*

Like already said, it is not meaningful to compare the results of microbolometers and InSb cameras in this kind of test. So one can only conclude that microbolometers are not suitable for detecting effects lasting only milliseconds. The relation of the thermal time constant to the pixel temperature was presented in Equation 2.26. According to that equation, the temperature of the pixel after a certain amount of time can be calculated as

$$T(t) = T_\infty + \Delta T e^{-t/\tau}, \tag{4.2}$$

where $\Delta T = T_i - T_\infty$ is the initial temperature difference between the pixel ($T_i$) and the object ($T_\infty$). In Figure 4.10, one can detect how the temperature of a microbolometer pixel will increase as a function of time. The plots illustrate the theoretical behaviour of the pixels in performed measurements. The initial pixel temperature i.e. the environment temperature was 24.5 ℃ and 22.2 ℃ in

measurements of A655sc and T1020, respectively. The temperature values that the pixel had time to reach when the object was visible for 1.3 ms or 8.5 ms are marked to the plots with circles. The red and blue lines show the temperature values of the object used in test cases of A655sc and T1020 cameras, respectively.

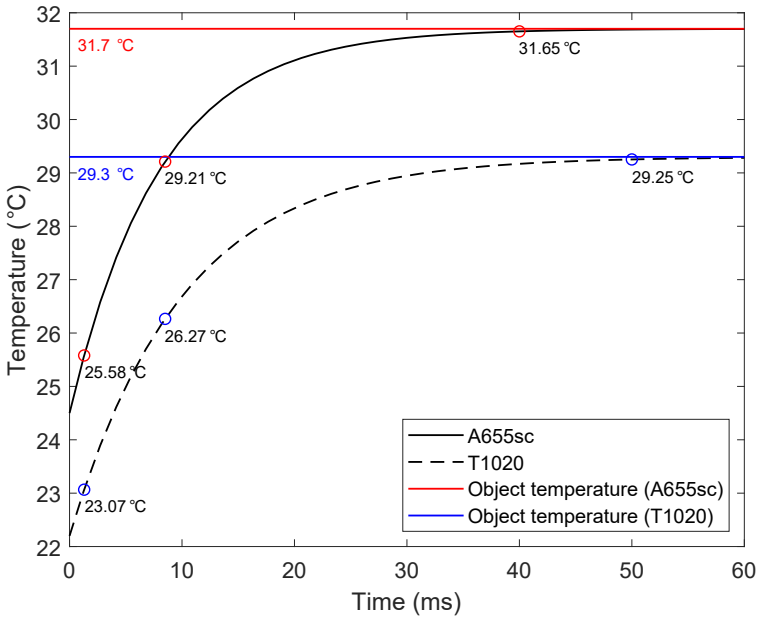


***Figure 4.10*** *The temperature of the microbolometer pixel as a function of time. The plots represent the theoretical behaviour of the pixel in performed measurements.*

According to the thermal time constants, the object should be visible for A655sc at least 40 ms and for T1020 at least 50 ms. Then one could be sure, that the pixel has approximately reached the temperature of the object. The theoretical temperature values of the pixel after 40 ms (A655sc) and 50 ms (T1020) have also been marked in Figure 4.10 with circles. So depending on the thermal time constant, A655sc and T1020 can reliably detect effects as fast as 25 Hz and 20 Hz, respectively. However, one should notice that because the frame rate of T1020 is 30 Hz, the highest frequency component of the signal can be just 15 Hz.

## 4.2 NETD values

In Figure 4.11, the histogram presents the distribution of the temporal standard deviation values of the pixels calculated for every camera. An area of 100 × 100 pixels was selected for the analysis and thus the temporal NETD value is calculated for 10 000 pixels over 32 sequential frames. In top of the figure one can see the median of the standard deviations i.e. the temporal NETD of the camera.

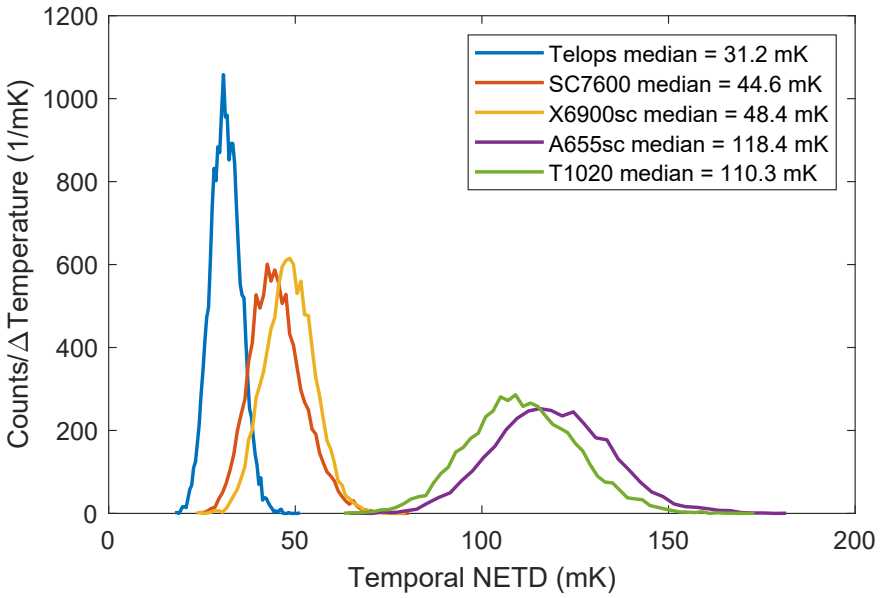


***Figure 4.11*** *Temporal NETD values of tested cameras. The histograms present the distribution of standard deviations of each pixel in* $100 \times 100$ *area. The temporal NETD of the camera is defined as the median value of all standard deviation values.*

When the calculated temporal NETD values are compared to the NETD values provided by the manufacturers, one can notice that the calculated values based on the measurements are much higher. The noise reduction setting of the microbolometer cameras was set off during the measurements. This is the feature of ResearchIR software that can be used with microbolometers. According to Danjoux (2019), the noise reduction feature performs some temporal frame averaging and thus smoothens the output signal. According to discussion with Danjoux (2019), FLIR uses a special noise reduction filter for the specification measurements with microbolometers. This filter is not identical with the feature of ResearchIR, but those are close to each other. Just for testing the noise reduction, one test was performed to A655sc camera where the feature was on. This caused the temporal NETD of A655sc to drop to 28 mK. So this setting reduces the noise level significantly. Because the detected area was small and the heat effect was rapid, it was decided not to use the noise reduction feature in the camera tests to prevent reducing the desired signal as well.

For cooled photon detectors, there was not a noise reduction option, yet the calculated NETD values of the InSb cameras are higher than the values provided by the manufacturers. However, the NETD measurements of manufacturers are performed in strictly controlled laboratory conditions with an object close to a perfect blackbody. It is understandable, that the values given by the manufacturers are smaller.

After all, one can reliably compare the NETD values of different cameras only if the test conditions and the signal processing algorithms are similar for every camera.

When comparing the calculated NETD values of the cameras, one can notice that the values are almost the same between microbolometers. Also the two InSb cameras manufactured by FLIR produce similar values. According to the calculated values, the InSb camera manufactured by Telops produces the best NETD value, 31.2 mK. The standard deviation values of different pixels deviate more from the median value in microbolometers than in InSb cameras. Also in this respect, Telops is better than the other cameras.

The results of the spatial NETD calculations are also favourable to Telops as can be seen in Figure 4.12. Now the histogram presents the distribution of standard deviation values of $5 \times 5$ pixel areas that is calculated for every camera from the averaged frame. The areas of the histograms for InSb X6900sc and MB T1020 are larger than others, as these cameras contain more pixels i.e. a higher resolution. Again, the standard deviation values between different $5 \times 5$ pixel areas vary more with the microbolometers. The manufacturers do not provide spatial NETD value for the cameras.

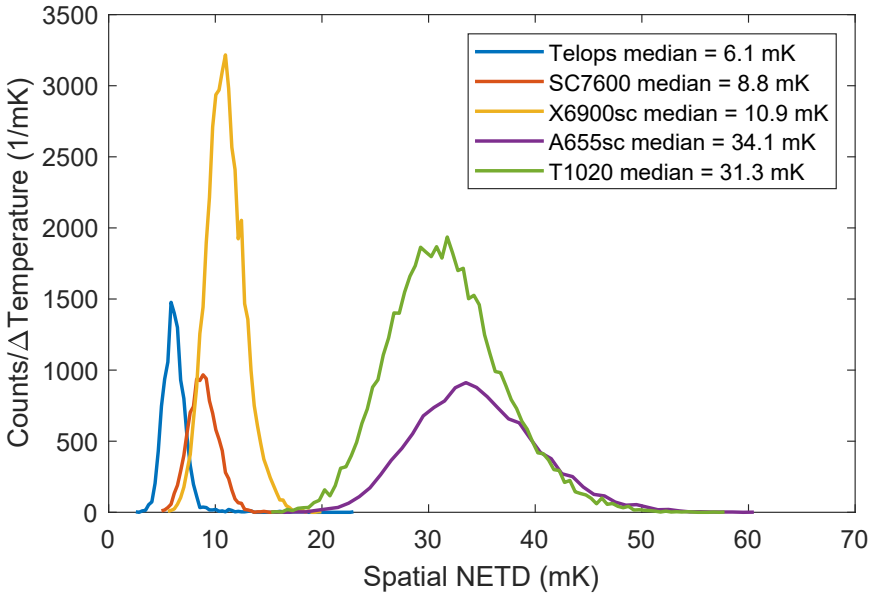


***Figure 4.12*** *Spatial NETD values of tested cameras. The histograms present the distribution of standard deviations of* $5 \times 5$ *pixel areas. The spatial NETD of the camera is defined as the median value of all standard deviation values.*

The total NETD values were also calculated for the cameras. The calculated temporal, spatial and total NETD values are presented in Table 4.2. It is important to notice, that the NETD is not an intrinsic feature of IR cameras. It will vary

depending on the test conditions, the camera settings and the target temperature as told in Subsection 2.2.6. Typically one desires to know what is the temperature difference that will create a signal equal to the noise level. After all, this reveals the magnitude of temperature differences that can be detected with the camera. Instead of just checking the NETD value provided by the manufacturer, one should define the NETD value of the camera in real life operating conditions to acquire a realistic NETD value.

***Table 4.2*** *The calculated temporal, spatial and total NETD values.*

| **Cameras** | **Temporal NETD (mK)** | **Spatial NETD (mK)** | **Total NETD (mK)** |
|---|---|---|---|
| Telops Fast-IR 2K | 31.2 | 6.1 | 31.8 |
| FLIR SC7600 | 44.6 | 8.8 | 45.5 |
| FLIR X6900sc | 48.4 | 10.9 | 49.6 |
| FLIR A655sc | 118.4 | 34.1 | 123.2 |
| FLIR T1020 | 110.3 | 31.3 | 114.6 |

## 4.3 Sources of error

Some possible sources of error can be found. For example, the temperature of the stationary plate was supposed to have the same temperature as the environment. However, there were many heat sources, e.g. the camera, the servo motor and the water container near the plate system that could possibly heat the surface of the plate. Even though the surfaces of the plates were painted to matt black, the emissivity of the surface could not reach the value of 1. Thus reflection of radiation coming from the camera itself, for example, may have occurred. The cameras were tested in different places at different times. So even though the set-up was covered from environment, some errors can still be caused by variation of environmental conditions.

One possible source of error is the uncertainty of the thermometers. However, with the rapid heat effect tests this was not a big problem because the temperature difference was more important than the absolute temperature values. Because the same thermometers were used in every test, the measured temperature differences should be comparable. The water temperature was dropping a little during the measurement. However, this was considered when the average temperature values were calculated.

The results of the cameras varied because the rotation of the plate and the frame rate were not synchronized so that the frame would be captured when the object was visible. This would be a good development step for the measurement set-up in the future. The other option is to increase the frame rate to the Nyquist rate in those cameras for which this is possible.

A specific error of X6900sc InSb camera was the error in the NUC file. This was found out only after the measurements and it was not possible to reproduce the measurement, as the camera was returned to the manufacturer. This error, however, should not affect to the rapid heat effect tests. What comes to the noise values, the temperature variation of the frames was corrected afterwards in Matlab, as described in 3.4.3. There can still be left some frequent temperature variations that were caused by the error and could not be removed. This should affect only the spatial NETD value, not the temporal one. A bad pixel was also located in the frame of X6900sc and Telops. The values of these pixels were replaced with the average value of neighbouring pixels, thus removing their effect on the results. When performing camera tests, one should be aware of possible bad pixels, even though performed NUC should correct them.

All the cameras were calibrated in the factory. However, for some of the cameras this was performed five years ago. In the future, one should consider if the camera should be calibrated manually before the measurements. This is important especially when exact absolute temperature values are considered.

# 5. CONCLUSION

This thesis work was conducted as it was requested by Imaqen Ltd. The aim was to obtain a better understanding of the features and their differences between a variety of IR camera technologies. Based on the evaluation, one could better find the most suitable camera solution for a future application of the company. In theoretical part of the work, one could discover the fundamental properties of different detector technologies. There are advantages and disadvantages with every detector and so the most suitable device can be obtained when the requirements of the application are known. For example, QWIPs are suitable for applications where large resolution, high sensitivity and uniformity of the detector are essential. PV detectors, either InSb or MCT, on the other hand are suited for fast frame rate applications requiring high sensitivity. Even though microbolometers are not so sensitive and fast compared to photon detectors, they offer a competitive option for many applications while having reduced cost and size.

Five different IR cameras, three InSb photon detectors and two microbolometers were also experimentally tested. A test set-up was planned and built for the measurements. The aim was to test the ability of the cameras in detecting rapid heat effects. It was decided to build a technical phantom containing a rotating plate with a small sector hole and behind the plate there was placed a warm object. The user could alter the rate and the duration of the heat effect by adjusting the rotational speed of the plate. With this approach, a controlled and alterable rapid heat effect was created.

According to the test results, one could conclude that microbolometers are not suitable for detecting heat effects lasting only a couple of milliseconds. This was already a hypothesis made on the grounds of the theory. Telops Fast-IR 2K and FLIR X6900sc performed best in this test. However, the group of tested cameras was small and only two different detector types were compared. To make better conclusions one should test larger variety of IR detectors e.g. QWIP, SLS and MCT detectors.

Looking ahead to the future, one could make some improvements for the test set-up.

For example, compared to the length of the heat effect, the sampling rate i.e. the frame rate was too low on almost all the test cases. The solution is to increase the frame rate to the Nyquist rate for those cameras that this is possible. The other option is to synchronize the frame rate and rotation of the plate, especially in those cameras for which increasing the frame rate is not possible. Need for the camera calibration should also be considered when it has been a long time since it has been performed the last. Each camera should also be tested multiple times to verify the repeatability of the results. In this thesis work, it was not possible to reproduce the measurements because X6900sc and T1020 cameras were returned to the manufacturer from where they were borrowed by the dealer, Infradex. Other cameras were also occupied by other projects.

The NETD values were also defined for the cameras. The NETD value determines the temperature difference needed to create a signal equal to the noise level of the camera. Thus one can approximate how small temperature differences the camera can distinguish in certain conditions. The calculated temporal NETD values were compared to the values provided by the manufacturer and it was discovered that the calculated NETD values were much higher. Especially the values of microbolometers differed from the manufacturer values. Possible reasons for this are the conditions of the camera and environment e.g. the noise reduction option of the microbolometer cameras was set off, the measurement target was not a real blackbody, and environment conditions were varying during and between the measurements. By using the noise reduction feature with microbolometers, one could reduce the NETD value to the same level with the InSb cameras. One should still consider using that, as some essential information of the desired signal can be lost because of the averaging. More meaningful than comparison of the calculated NETD value with value provided by the manufacturer is to compare the calculated values with each other. This exposes the real differences between the cameras in certain conditions.

Even though the noise levels and the response rate of microbolometers were worse than values of InSb cameras, one should remember that the NETD values and the period of time discussed here are on scales of millikelvin and millisecond, respectively. In many applications it is not necessary to distinguish temperature differences that small. The same thing is with the speed. If the temperature of the observed object is changing slowly and the scene is relatively static, there is no need for high frame rate and extremely short integration time.

There are still many fields of science e.g. medicine, where detecting very small temperature differences is beneficial. In medical use, the high uniformity and sensitivity of the detector are important as temperature differences on a human skin can be

very small. At the moment, one can assume that heat effects of a human body are not so rapid compared to the ones used in this work. However, there can be some unknown benefit that usage of a high frame rate could offer.

In many situations it is a trade-off between some features of the camera e.g. between sensitivity and speed. Thus one should make a decision between different features according to the requirements of the application. Therefore, one cannot arrange different cameras in order of preference without knowing the application first.

# REFERENCES


Accetta, J. S. and D. L. Shumaker (1993). *The infrared and electro-optical systems handbook*. SPIE. ISBN: 9780819410726.

Agrawal, B. N. and M. F. Platzer (2018). *Standard handbook for aerospace engineers*. Second edition. McGraw-Hill Education. ISBN: 9781259585173.

Balch, M. (2003). *Complete digital design: a comprehensive guide to digital electronics and computer system architecture*. First edition. McGraw-Hill Professional. ISBN: 9780071409278.

Bass, M. (2010). *Handbook of optics: volume ii - design, fabrication, and testing; sources and detectors; radiometry and photometry*. Third edition. McGraw-Hill Professional. ISBN: 9780071498906.

Cengel, Y. A. (2002). *Heat transfer: a practical approach*. Second edition. McGraw-Hill. ISBN: 9780071151504.

D'Amico, A., C. D. Natale, F. L. Castro, S. Iarossi, A. Catini, and E. Martinelli (2009). *Unexploded ordnance detection and mitigation*. Ed. by J. Byrnes. First edition. Springer. DOI: 10.1007/978-1-4020-9253-4.

Danjoux, R., Application Support Engineer Flir Instruments (2019). Electronic mail: 13.-14.-6.2019.

Diakides, M., J. D. Bronzino, and D. R. Peterson (2017). *Medical infrared imaging: principles and practices*. CRC Press. ISBN: 9781138072299.

Driggers, R. G., M. H. Friedman, and J. M. Nichols (2012). *Introduction to infrared and electro-optical systems*. Second edition. Artech House. ISBN: 9781608071012.

FLIR (2016). *Application story*. Accessed: 9.7.2019. URL: https://www.infradex.com/wp-content/uploads/2016/08/RD-App.story-high-speed.pdf.

FLIR (A655sc) (2014). *FLIR A655sc: High resolution science grade LWIR camera*. Accessed: 12.3.2019. URL: https://www.flirmedia.com/MMC/THG/Brochures/RND_011/RND_011_US.pdf.

*FLIR Product catalog 2018* (2018). Accessed: 23.4.2019. FLIR Systems Inc. URL: http://www.flir.kiev.ua/pdf/flir-product-catalog.pdf.

FLIR (SC7600) (2014). *FLIR SC7000 Series: State-of-the-art infrared technology for R&D / Science*. Accessed: 12.3.2019. URL: http://www.flirmedia.com/MMC/THG/Brochures/RND_017/RND_017_US.pdf.

FLIR (T1020) (2015). *FLIR T1K: HD Thermal Imaging Camera*. Accessed: 12.3.2019. URL: https://www.flir.com/globalassets/imported-assets/document/t1k_datasheet.pdf.

FLIR Technical Support Center (2019). *D* Specification*. Accessed: 4.3.2019. URL: https://flir.custhelp.com/app/answers/detail/a_id/471/related/1.

FLIR (X6900sc) (2018). *FLIR X6900sc: High Speed MWIR Science-Grade Infrared Camera*. Accessed: 7.3.2019. URL: https://www.infradex.com/wp-content/uploads/2016/09/X6900sc-datasheet.pdf.

Gade, R. and T. B. Moeslund (2014). "Thermal cameras and applications: a survey". In: *Machine Vision and Applications* 25.1, pp. 245–262. DOI: 10.1007/s00138-013-0570-5.

GRYSTAL GmbH (n.d.). *Optical components: lenses*. Accessed: 29.01.2019. URL: http://crystal-gmbh.com/en/products/opticals/lenses.php.

Gunapala, S. D. and S. V. Bandara (1999). "Significance of the first excited state position in quantum well infrared photodetectors". In: *Microelectronics Journal* 30.10, pp. 1057–1065. DOI: 10.1016/S0026-2692(99)00056-7.

Hamamatsu and Solid State Division (2011). *Characteristics and use of infrared detectors*. Accessed: 29.1.2019. URL: https://www.hamamatsu.com/resources/pdf/ssd/infrared_kird9001e.pdf.

Harrison, P. and A. Valavanis (2016). *Quantum wells, wires and dots: theoretical and computational physics of semiconductor nanostructures*. Fourth edition. Wiley. ISBN: 9781118923344.

Hecht, E. (2017). *Optics*. Fifth edition. Pearson Education. ISBN: 9781292096933.

Hecht, J. (1999). *The laser guidebook*. Second edition. McGraw-Hill. ISBN: 97800713-59672.

Hellier, C. J. (2013). *Handbook of nondestructive evaluation*. Second edition. McGraw-Hill Education. ISBN: 9780071777148.

Herzberger, M. (2014). "Focal length". In: *AccessScience*. DOI: 10.1036/1097-8542.265300.

*HypIR manual* (2017). *High-performance infrared cameras: HypIR software suite user's guide*. Telops.

Incropera, F. P. and D. P. DeWitt (2001). *Fundamentals of heat and mass transfer*. Fifth edition. John Wiley & Sons. ISBN: 9780471386506.

Janesick, J. R. (2001). *Scientific charge-coupled devices*. SPIE. ISBN: 9780819436986.

Johnson, M. (2003). *Photodetection and measurement: maximizing performance in optical systems*. McGraw-Hill. ISBN: 9780071409445.

Kaaresoja, T., Technical Sales Specialist Infradex Inc. (2018). Electronic mail: 25.10.2018.

Kasunic, K. J. (2011). *Optical systems engineering*. McGraw-Hill Professional. ISBN: 9780071754408.

Khandpur, R. S. (2014). *Handbook of biomedical instrumentation*. Third edition. McGraw-Hill Education LLC. ISBN: 9789339205430.

Khandpur, R. S. (2006). *Handbook of analytical instruments*. Second edition. McGraw-Hill Education LLC. ISBN: 9780070604605.

Knight Optical (2014). *Infrared optics*. Accessed: 29.01.2019. Knight Optical. URL: https://www.knightoptical.com/stock/optical-components/infrared-optics/.

Kohin, M. and N. Butler (2004). "Performance limits of uncooled VOx microbolometer focal plane arrays". In: *Proceedings of SPIE - The International Society for Optical Engineering*. DOI: 10.1117/12.542482.

Kukkonen, C. A., M. N. Sirangelo, R. Chehayeb, M. Kaufmann, J. K. Liu, S. B. Rafol, and S. D. Gunapala (2001). "Commercialization of quantum well infrared photodetector focal plane arrays". In: *Infrared Physics and Technology* 42.3, pp. 397–405. DOI: 10.1016/S1350-4495(01)00099-8.

Laikin, M. (2006). *Lens design*. Fourth edition. CRC Press. ISBN: 9780849382789.

Liu, X.-M., L. Han, and L.-T. Liu (2006). "A novel uncooled a-Si microbolometer for infrared detection". In: *2006 8th International Conference on Solid-State and Integrated Circuit Technology Proceedings*, pp. 626–628. DOI: 10.1109/ICSICT.2006.306396.

*Matlab documentation* (2019). Accessed: 9.3.2019. The MathWorks Inc. URL: https://se.mathworks.com/help/matlab/.

McGee, T. D. (1988). *Principles and methods of temperature measurement*. John Wiley & Sons. ISBN: 9780471627678.

Meola, C., S. Boccardi, and G. M. Carlomagno (2015). "Measurements of very small temperature variations with LWIR QWIP infrared camera". In: *Infrared Physics and Technology* 72, pp. 195–203. DOI: 10.1016/j.infrared.2015.08.004.

Meroli, S. (n.d.). *CMOS active pixel sensor vs CCD performance comparison*. Accessed: 1.4.2019. URL: http://meroli.web.cern.ch/lecture_cmos_vs_ccd_pixel_sensor.html.

Mobley, K. (2013). *Maintenance engineering handbook*. Eighth edition. McGraw-Hill. ISBN: 9780071826617.

MoviTHERM (2018). *What is NETD in a thermal camera?* Accessed: 18.3.2019. URL: http://movitherm.com/knowledgebase/netd-thermal-camera/.

O'Leary, P. and M. Harker (2011). "Polynomial approximation: an alternative to windowing in furier analysis". In: *IEEE International Instrumentation and Measurement Technology Conference*, pp. 1–6. DOI: 10.1109/IMTC.2011.5944262.

O'Leary, P. and M. Harker (2014). *Discrete orthogonal polynomial toolbox: DOPBox version 1.8*. Accessed: 19.6.2019. URL: https://se.mathworks.com/matlabcentral/fileexchange/41250-discrete-orthogonal-polynomial-toolbox-dopbox-version-1-8.

O'Leary, P. and M. Harker (2013). *2D polynomial data modelling: version 1.0*. Accessed: 8.7.2019. URL: https://se.mathworks.com/matlabcentral/fileexchange/42474-2d-polynomial-data-modelling-version-1-0.

Paiella, R. (2006). *Intersubband transition in quantum structures*. McGraw-Hill Professional. ISBN: 9780071457927.

Posch, C., D. Matolin, R. Wohlgenannt, T. Maier, and M. Litzenberger (2009). "A microbolometer asynchronous dynamic vision sensor for LWIR". In: *IEEE Sensors Journal* 9.6, pp. 654–664. DOI: 10.1109/JSEN.2009.2020658.

Red Current Ltd (2019). *Building thermal imaging surveys*. Accessed: 21.5.2019. URL: https://www.red-current.com/thermal-imaging-surveys/building-thermography.

Reich, G. (2005). "Near-infrared spectroscopy and imaging: basic principle and pharmaceutical applications". In: *Advanced Drug Delivery Reviews*. DOI: 10.1016/j.addr.2005.01.020.

*ResearchIR 4 User's Guide* (2016). Document Number: 29354-000, Accessed: 9.3.2019. FLIR Systems Inc. URL: http://www.flir.at/fileadmin/user_upload/Vertretungen/FLIR/Software/ResearchIR/ResearchIR_4_Manual_29354-000-en-us-1608-nbn.pdf.

Rogalski, A. (2002). "Chapter 2 - Comparison of photon and thermal detector performance". In: *Handbook of infrared detection technologies*. Ed. by M. Henini and M. Razeghi. Elsevier Science, pp. 5–81. DOI: 10.1016/B978-185617388-9/50002-2.

Rogalski, A. (2003a). "Infrared detectors: status and trends". In: *Progress in Quantum Electronics* 27.2, pp. 59–210. DOI: 10.1016/S0079-6727(02)00024-1.

Rogalski, A. (2003b). "Quantum well photoconductors in infrared detector technology". In: *Journal of Applied Physics* 93.8, pp. 4355–4391. DOI: 10.1063/1.1558224.

Rogalski, A. (2003c). "Third-generation infrared photon detectors". In: *Optical Engineering* 42.12, pp. 3498–3516. DOI: 10.1117/1.1625377.

Rogalski, A. (2006). "Competitive technologies of third generation infrared photon detectors". In: *Opto-electronics Rewiew* 14.1, pp. 87–101. ISSN: 1230-3402.

Rogalski, A. (2010). *Infrared detectors*. Second edition. CRC Press. ISBN: 978142007-6714.

Rogalski, A. (2018). *Infrared and terahertz detectors*. Third edition. CRC Press. ISBN: 9781138198005.

Rogalski, A., M. Kopytko, and M. Piotr (2018). *Antimonide-based infrared detectors: a new perspective*. SPIE Press Book. ISBN: 9781510611399.

Ronda, A., Application Support Engineer Flir Instruments (2018). Electronic mail: 14.11.2018.

Ryzhii, V. (2003). *Intersubband infrared photodetectors*. World Scientific. ISBN: 9789812775535.

Sakudo, A. (2016). "Near-infrared spectroscopy for medical applications: current status and future perspectives". In: *Clinica Chimica Acta*. DOI: 10.1016/j.cca.2016.02.009.

Serway, R. A. and J. W. Jewett (2014). *Physics for scientists and engineers with modern physics*. Ninth Edition. Cengage Learning. ISBN: 9781305401969.

Soloman, S. (2010). *Sensors handbook*. Second edition. McGraw-Hill Professional. ISBN: 9780071605700.

Tan, C. L. and H. Mohseni (2018). "Emerging technologies for high performance infrared detectors". In: *Nanophotonics* 7.1, pp. 169–197. DOI: 10.1515/nanoph-2017-0061.

Telops (2015). *Fast high performance infrared camera: FAST-IR 2K*. Accessed: 12.3.2019. URL: http://www.photonlines.es/downloads/Camara_termica_Telops_Fast_IS.pdf?PHPSESSID=o5dil7vte5n27fbsh19qcqu3j1.

*The ultimate IR handbook* (2012). *The ultimate infrared handbook for R&D professionals*. FLIR Systems Inc.

Vincent, J. D., S. Hodges, J. Vampola, M. Stegall, and G. Pierce (2015). *Fundamentals of Infrared and Visible Detector Operation and Testing*. Second edition. John Wiley & Sons. DOI: 10.1002/9781119011897.

Vollmer, M. and K.-P. Möllmann (2017). *Infrared thermal imaging: fundamentals, research and applications*. Second edition. John Wiley & Sons. ISBN: 9783527693320.

Wang, B., J. Lai, H. Li, H. Hu, and S. Chen (2013). "Nanostructured vanadium oxide thin film with high TCR at room temperature for microbolometer". In: *Infrared Physics and Technology* 57, pp. 8–13. DOI: 10.1016/j.infrared.2012.10.006.

Webster, J. G. and H. Eren, eds. (2014). *Measurement, instrumentation, and sensors handbook*. Second edition. CRC Press. DOI: 10.1201/b15474.

Weng, Q. (2012). *An introduction to contemporary remote sensing*. McGraw-Hill. ISBN: 9780071740111.

Young, H. D., R. A. Freedman, and A. L. Ford (2011). *Sears and Zemansky's university physics: with modern physics*. Thirteenth edition. Addison-Wesley. ISBN: 9780321696861.

Yu, P. Y. and M. Cardona (2001). *Fundamentals of semiconductors: physics and materials properties*. Third edition. Springer-Verlag. ISBN: 9783540413233.

Zhang, C., H. Chang, F. Zhao, and X. Hu (2013). "Design principle of Au grating couplers for quantum-well infrared photodetectors". In: *Optics Letters* 38.20, pp. 4037–4039. DOI: 10.1364/OL.38.004037.

Zimmermann, H. (2009). *Integrated silicon optoelectronics*. Springer. DOI: 10.1007/978-3-642-01521-2.